Corrosion mechanisms and durability models for historical tinplate food cans

THÈSE N^{O} 8910 (2018)

PRÉSENTÉE LE 9 NOVEMBRE 2018

À LA FACULTÉ DES SCIENCES ET TECHNIQUES DE L'INGÉNIEUR

GROUPE SCI STI SM

PROGRAMME DOCTORAL EN SCIENCE ET GÉNIE DES MATÉRIAUX

ÉCOLE POLYTECHNIQUE FÉDÉRALE DE LAUSANNE

POUR L'OBTENTION DU GRADE DE DOCTEUR ÈS SCIENCES

PAR

Fabio COVA CAIAZZO

acceptée sur proposition du jury:

Prof. D. Damjanovic, président du jury
Dr S. Mischler, Dr L. Brambilla, directeurs de thèse
Prof. E. P. M. V. Angelini, rapporteuse
Prof. S. Virtanen, rapporteuse
Dr C. Roussel, rapporteur

ÉCOLE POLYTECHNIQUE
FÉDÉRALE DE LAUSANNE
Suisse
2018

*To my beloved parents "**Elide & Walter**"*
*and my brother "**Nicola**"*

Acknowledgements

It is now time to say thanks to all the great people that in the past four years who were always by my side. Needless to say, this important achievement of my life would not have been possible without their contribution and support.

First and foremost, I want to thank my thesis supervisors, Dr. Stefano Mischler and Dr. Laura Brambilla, for their patience, kindness and scientific experience, which made them the best supervisors I could have wished for. They believed in me since my first day of PhD, and I owe them my scientific and professional growth. There are no word to describe my gratitude for Stefano for the opportunities he gave me during these years.

I acknowledge the members of my PhD jury: Prof. Dragan Damjanovic (EPFL), Dr. Stefano Mischler (EPFL), Dr. Laura Brambilla (HES-SO Arc Conservation-Restauration of Neuchâtel), Prof. Emma Angelini, (Polytechnic University of Turin), Prof. Sannakasia Virtanen (University of Erlangen-Nuremberg) and Dr. Christophe Roussel (EPFL).

Further, I want to thank the Swiss National Foundation for Scientific Research for the founding of the CANS project (CR12I1-152946/1) and all the others partners involved in this project for our precious and successful collaboration: Régis Bertholon, Laura and Aline Michel (Haute École Arc Conservation-Restauration of Neuchâtel), Olivier Schinz (Ethnography museum of Neuchâtel), Rudolf Schmitt and Dimitri Bocquel (Institute of Life Technologies).

I thank Angela Montanari (Stazione Sperimentale per l'Industria delle Conserve Alimentari) for her technical advice about metallic food packaging.

My special thanks goes to Dr. Anna Igual Muñoz and Dr. Alex Roda Buch who gave me scientific and moral support during the thesis writing. For them, I have to say that they have been more than colleagues; they have been my Spanish parents in Switzerland.

For the surface analysis, the technical support and, most importantly, for becoming a very good friends of mine I thank Pierre Mettraux.

Another special thank goes to my colleagues Leili, Valentine, Angela, Vance and Shoufan, together we shared the joys and the sorrows of our PhD life. The feeling for each other is more than a simple friendship, TIC group is a family and I am sure that all of us will never forget these amazing years we spent together.

For helping me with all the administrative troubles, I thank the secretary of the TIC group, Sylvie Vaucher and the secretaries of the Material Science doctoral school, Anne Kolly and Chrystelle Demierre.

Thanks to Marta, Alice, Matteo, Francesca, Chiara and Alessio, the fellow travellers, and now good friends, that were spending time chatting with me every weekend during the train ride to Italy.

Thanks to Mathias, Gianluca, Du, Antoine, Alvaro and Michael from the SMAL laboratory for all the good times we had and in particular for the evenings spent at the Satellite enjoying nice beers. Thanks to their laboratory, I had the chance to meet one of the most extraordinary people I have ever met, Alice.

To her I owe all the best memories of my period in Lausanne, from the beginning of our friendship we helped each other, but the help she gave me during the last year is priceless.

Finally, I would like to express my infinite gratitude to my family and in particular to my parents and my brother. They have been always by my side, supporting and encouraging me every single day.

The PhD is the crowning of a long educational endeavour, thus I would like to acknowledge the people that allowed me to be admitted to such a prestigious university as EPFL.

Thanks to my high school professors, Emanuele Manera, Silvia Grosso, Annamaria Fornara and Vittoria Donini for laying strong foundations on which I could build my future.

Thanks to my Master's thesis supervisor, Dr. Stefano Trasatti. During the year I spent in his laboratory I learned how to carry out scientific research. He always trusted me and gave me important responsibilities, paving the way for my future in the electrochemistry and corrosion fields.

Abstract

Since the early 19th century, canning has been one the most efficient ways of preserving foods. Tinplated steel has been used since the beginning for this purpose and it is still one of the materials most used for can production. The reason for this long-lasting success is because it combines the good mechanical strength of steel with the corrosion resistance of tin. Nowadays, historically relevant cans enrich the collections of several museums around the world. However, these collections are threatened by severe corrosion phenomena, which may lead to perforation, swelling and bursting of the container. Perforation and bursting are extremely dangerous because they not only lead to irreversible damage of the can itself, but are also a threat to other artefacts which are stored in proximity.

The aim of this thesis is to study the corrosion mechanism of tinplate and to propose a durability model that can be used by museum conservators to define an intervention timeline for historical and new can collections. The strategy of the thesis was to investigate separately the material structure and the corrosion mechanisms of the tinplate constituents using model electrolytes and then to combine the two outcomes in a predictive model.

Tinplate is a composite material comprising several metallic layers, which interact with the complex food matrix. The sandwich-like structure of tinplate, composed of an external tin layer, an intermediate intermetallic compound layer and a core of mild steel, was characterized via a multi-technique approach combining chrono-potentiometry, chrono-amperometry, Auger electron spectroscopy (AES), X-ray fluorescence (XRF) spectroscopy, scanning electron microscopy (SEM) and 3D white light interferometry (3D WLI). The analysis showed that the relevant features that need to be considered to make predictions concerning the corrosion mechanism and lifetime of tinplate are the thickness of the tin layer, its porosity, the base steel roughness and the structure of the tin-steel interface.

Canned foods cover a wide range of pH values – from neutrality to pH3 – and they contain several molecules and ions known to affect tinplate corrosion, such as

polyprotic complexing acids, protons, oxygen, nitrates, sulphur dioxide, natural dyes, etc. In this study, the mechanisms and the kinetics of tin corrosion and tin–iron galvanic coupling were investigated in model electrolytes constituted by buffer solutions of citric, malic and oxalic acids at constant oxygen concentration, mimicking the typical environment of canned fruits and vegetables. The study was carried out using an electrochemical approach based on a potentiodynamic polarization technique in static conditions and under convection (rotating disk electrode). XPS was used as an additional ex-situ technique for the investigation of the tin–iron galvanic coupling mechanism.

The results showed that depending on the potential, different mechanisms control tin corrosion, namely: the charge transfer reduction of protons, the diffusion-limited reduction of oxygen and the active dissolution of tin and its passivation. Interestingly, all these reaction are affected by parameters such as pH level, oxygen content and the complexing strength of electrolytes, but to different extents.

Furthermore, the study of tin–iron galvanic coupling demonstrates an increase in the kinetics of tin dissolution, but at the same time a reduction in the reactivity of iron towards acid corrosion due to a self-healing mechanism.

The rationalization of the corrosion mechanisms using kinetic equations based on well-defined parameters permits successful development of a durability model able to predict the lifetime of tinplated cans based on the material structure.

Keywords: Corrosion, Food packaging, Tinplate, Tin, Modelling, Tin–iron galvanic coupling**.**

Riassunto

Sin dall'inizio del XIX secolo, l'inscatolamento è stato uno dei metodi più efficienti per la conservazione degli alimenti. Dalla sua introduzione e fino ad i giorni nostri, la banda stagnata è il principale materiale utilizzato per la produzione di lattine e scatolette. Il motivo di questo successo è che la banda stagnata combina la buona resistenza meccanica dell'acciaio con l'ottima resistenza a corrosione dello stagno. Oggi nel mondo, svariati musei annoverano nelle loro collezioni lattine d'importanza storica. Tuttavia, queste collezioni sono minacciate da importanti fenomeni corrosivi che possono portare alla perforazione, rigonfiamento ed esplosione delle lattine. La perforazione e l'esplosione sono rischiose in quanto, non solo determinano il danneggiamento irreversibile della lattina stessa, ma possono rovinare anche altri manufatti e oggetti conservati in prossimità.

Lo scopo di questa tesi è stato quello di studiare i meccanismi di corrosione della banda stagnata proponendo un modello di durabilità che possa essere utilizzato dai conservatori dei musei per definire una sequenza temporale di controllo e d'intervento per la conservazione di lattine appartenenti a collezioni già esistenti o in via di costituzione.

La strategia della tesi è stata quella di studiare separatamente la struttura del materiale e i meccanismi di corrosione, in elettroliti modello, dei materiali costitutivi della banda stagnata per poi combinare le due informazioni in un modello predittivo.

La banda stagnata è un materiale composito costituito da diversi strati metallici che interagiscono con la complessa matrice organica degli alimenti. La struttura a sandwich della banda stagnata è costituita da uno strato esterno di stagno, uno strato intermetallico intermedio e da un nucleo di acciaio dolce. La sua caratterizzazione è stata effettuata tramite un approccio multi-analitico che combina crono-potenziometria, crono-amperometria, Spettroscopia Auger, Spettrofotometria di fluorescenza a raggi X, Microscopia Elettronica a Scansione e Interferometria 3D a luce bianca. Questa analisi ha evidenziato l'importanza dello spessore dello strato di stagno, della sua porosità, della rugosità dell'acciaio e della struttura dell'interfaccia

stagno-acciaio sullo studio e sulla modellizzazione della corrosione della banda stagnata.

Gli alimenti in lattina coprono un ampio intervallo di pH, dalla neutralità fino a pH 3, e contengono diverse molecole e ioni noti per influenzare la corrosione della banda stagnata come, ad esempio, acidi poliprotici complessanti, protoni, ossigeno, nitrati, anidride solforosa, coloranti naturali etc.

I meccanismi e le cinetiche della corrosione dello stagno e dell'accoppiamento galvanico tra stagno e ferro sono stati studiati in elettroliti modello costituiti da soluzioni tampone di acido citrico, malico e ossalico a concentrazione di ossigeno costante. Queste soluzioni sono state scelte in quanto imitano le tipiche condizioni ambientali ritrovate all'interno delle scatole di conserva di frutta e verdura. Lo studio è stato effettuato per mezzo di un approccio elettrochimico basato su misure di polarizzazioni potenziodinamiche in condizioni statiche e dinamiche. Questa seconda condizione è stata studiata per mezzo di elettrodi a disco rotante. La Spettroscopia fotoelettronica a raggi X è stata impiegata come tecnica ex-situ per lo studio del meccanismo di accoppiamento galvanico tra stagno e ferro.

I risultati hanno mostrato che i meccanismi che controllano la corrosione dello stagno variano in funzione del potenziale: riduzione dei protoni sotto controllo di trasferimento di carica, riduzione dell'ossigeno limitata della diffusione, corrosione attiva dello stagno e sua passivazione. Tutte queste reazioni sono risultate essere influenzate in misura diversa da pH, concentrazione di ossigeno e forza complessante degli elettroliti. Inoltre, lo studio dell'accoppiamento galvanico tra stagno e ferro ha evidenziato che questo fenomeno determina allo stesso tempo un aumento della cinetica di dissoluzione dello stagno e una diminuzione della cinetica di corrosione acida del ferro a seguito di un meccanismo auto-curativo .

La razionalizzazione dei meccanismi di corrosione secondo equazioni cinetiche dipendenti da parametri ben definiti ha consentito di sviluppare con successo un modello di durabilità in grado di predire la durata di vita di lattine in banda stagnata in base alla struttura del materiale.

Parole chiave: Corrosione, Imballaggi alimentari, Banda stagnata, Stagno, Simulazione, Accoppiamento galvanico tra stagno e ferro.

Table of Contents

List of Abbreviations

Acronyms

CANS	Conservation of cAns in collectioNS project
ASTM	American Society for Testing Materials
3D WLI	3D White Light Interferometry
AAS	Atomic absorption spectroscopy
AES	Auger Electron Spectroscopy
ICP	Inductive coupled plasma spectroscopy
SEM	Scanning electron microscopy
XPS	X-ray Photoemission Spectroscopy
XRF	X-ray Fluorescence Spectroscopy
CE	Counter Electrode
HER	Hydrogen Evolution Reaction
K	Equilibrium constant
NA	Not Available data
ORR	Oxygen Reduction Reaction
PP	Potentiodynamic Polarization
RE	Reference Electrode
RGB	Red Green Blue
SCE	Saturated Calomel reference Electrode
WE	Working Electrode

Symbols

A	Surface (m^2)
b_a	Anodic Tafel's constant, base 10 logarithm (10)
b_c	Cathodic Tafel's constant, base 10 logarithm (10)
c_i	Concentration of the species i (mol/m^3)
D	Coefficient of diffusion (m^2/s)
d	Distance between electrodes (m)
E_{cc}	Short circuit potential (V)
E_{coup}	Galvanic coupling potential (V)
E_{corr}	Corrosion potential (V)
E°	Standard potential (V)
E_p	Passive potential (V)
E_{rev}	Reversible potential (V)
F	Faraday's constant (96485 C/mol)

j	Current density (A/m^2)
j_0	Exchange current density (A/m^2)
j_{cc}	Short circuit current density (A/m^2)
j_{coup}	Galvanic coupling current density (A/m^2)
j_{corr}	Corrosion current density (A/m^2)
j_l	Limiting current density (A/m^2)
j_p	Passive plateau current density (A/m^2)
MM	Molecular mass (g/mol)
OCP	Open Circuit Potential (V)
R_{int}	Ohmic resistance of the electrolyte (Ω)
R_{ext}	Resistance due to the electronic conductors (Ω)
r_p	Polarization resistance ($\Omega\ m^2$)
β_a	Anodic Tafel's coefficient (V)
β_c	Cathodic Tafel's coefficient (V)
δ	Thickness of the diffusion layer (m)
θ	Surface coverage % ($0 \leq \theta \geq 100$)
ν	Kinematic viscosity (m^2/s)
ρ	Density (kg/m^3)
ρ_e	Resistivity (Ω cm)
ω	Angular velocity (rad/s)
[ ]	Molarity (mol/L)

Subscripts

a	Anodic
ads	Adsorbed
b	Bulk
c	Cathodic
cc	Short cut
corr	Corrosion
i	Chemical species i
ox	Species oxidized in a half-cell reaction
red	Species reduced in a half-cell reaction
s	Surface
rev	Reversible

Superscripts

0	Standard State

1 Introduction

1.1 Context of the thesis

Cultural heritage includes extremely broad varieties of artworks, such as painting, sculpture, etc., but also unusual and everyday objects, such as food cans. The importance of cans arises from the fact that they attest not only to industrial and technological development, but also that they have become one of the symbols of the consumer society. Cans, as soon they were patented in the early 19th century, played a key role in scientific exploration expeditions and wars. Later on, since the beginning of the 20th century, the introduction of canned foodstuffs changed eating habits and women's status by reducing the time dedicated to meal preparation and thus contributing to developing women's professional activities. The incorporation of cans in contemporary art as a reflection on consumer society started from the middle of the 20th century [1].

Nowadays, cans enrich worldwide museum collections as relevant historical and cultural witnesses (**Figure 1**). However, their conservation is particularly problematic. Severe corrosion phenomena occur due to the interaction with the environment and between the organic content and the metallic container [2,3,4,5,6].

Figure 1 Example of cans in Swiss museum collections [6]

In 2014 the Swiss National Science Foundation granted funding for a three-year interdisciplinary project entitled “Conservation of cAns in collectioNS” (CANS CR12I1-152946/1), proposed by the Haute École Arc Conservation-Restauration of Neuchâtel. The objectives of the CANS project were to improve knowledge of heritage cans, develop treatment methodologies respecting the material authenticity and cultural values of these composite objects, propose solutions in terms of preventive conservation and study the internal corrosion of cans over the long term. Before the CANS project, there were no conservation/restoration protocols available allowing the long-term preservation of complete cans, including (i) the definition of an intervention timeline and (ii) the identification of corrosion protection methods.

The identification of can protection methods and the definition of intervention timelines require a fundamental understanding of the structure and corrosion mechanisms of the can materials over a time greater than the commercial shelf-life of canned foodstuffs (maximum five years). The long-term corrosion behaviour of food cans is at present little understood and no predictive or intervention tools for collection cans are available.

The materials used nowadays for can production are plain tinplated steel, lacquered tinplated steel, lacquered electrolytically chromium-coated steel (ECCS) and lacquered aluminium alloys [2,3]. This study is focused on the study of plain tinplated steel because it was the first adopted but is still broadly used in the manufacturing of cans.

1.2 State of the art

1.2.1 Tinplate

Tinplate consists of a light gauge mild steel coated on both faces with a thin protective layer of pure tin. The joining of these two metals makes it possible to develop a final material that combines the good mechanical strength and excellent formability of the base steel with the low toxicity, solderability and corrosion resistance of tin. The tinplate structure is typically represented in the literature as a linear succession of layers, as presented **Figure 2** [4-7]. In addition to steel and tin,

this structure also includes a tin–iron alloy phase and a passivation layer, which are formed during the production process by means of thermal treatment and chemical treatment, respectively.

Figure 2 Representation of the layered structure of one of the two sides of tinplated steel.

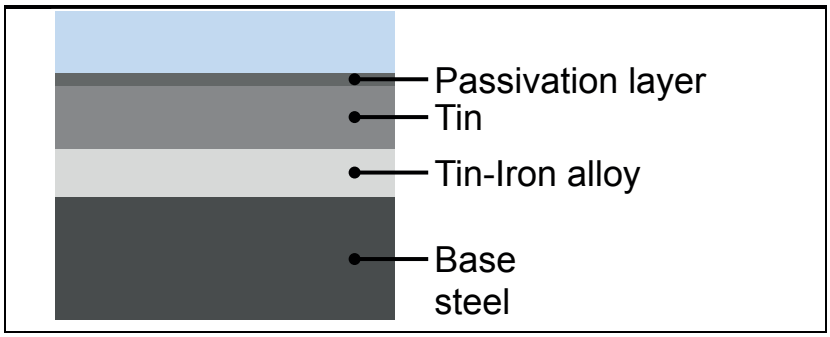

The base steel production and tinning are two independent processes [4-7]**.** The mild steel used is produced by means of the basic oxygen steelmaking (BOS) process. The resulting coils have a thickness range from 0.13mm to 0.5mm and are characterized by low residuals, good formability and good mechanical properties [6]**.** The chemical composition of the base steel is defined according to standard ASTM A623-06 [8], as reported in **Table 1**.

Table 1 Chemical requirements for tin mill products ASTM A623-16 [9].

Elements	Cast composition, max. %		
	Type D	Type L	Type MR
C	0.12	0.13	0.13
Mn	0.60	0.60	0.60
P	0.020	0.015	0.020
S	0.03	0.03	0.03
Si[a,b]	0.020	0.020	0.020
Cu	0.20	0.06	0.20
Ni	0.15	0.04	0.15
Cr	0.10	0.06	0.10
Mo	0.05	0.05	0.05
Al[c]	0.20	0.10	0.20
Other elements, each	0.02	0.02	0.02

[a] When steel produced by the silicon-killed method is ordered; the silicon maximum may be increased to 0.080%.

[b] When strand cast steel produced by the aluminium-killed method is ordered or furnished; the silicon maximum may be increased to 0.030% when approved by the purchaser.

[c] Types L and MR may be supplied as non-killed or killed which would respectively be produced without and with aluminium additions. The minimum aluminium level for type D is usually 0.02%.

The chemical composition of the base steel influences the corrosion resistance and the formability. Usually, the more corrosive the application, the tighter the control of the constitutive elements in the steel. Formability also depends on the base steel composition [4,6,8]**.**

Different types of base steels, with diverse properties and applications, are available on the market and classified by ASTM A623-16 [9], as follows:

- Base steel type D is an aluminium-killed steel intended for severe drawing applications.
- Base steel type L has low content of metalloids and residual elements and is therefore used to greatly improve the corrosion resistance of cans.
- Base steel type MR has low content of metalloids, as does type L, but it contains more residual elements. This base steel still has a good corrosion resistance and is used for most tinplate production.
- Base steels type LN and MRN are base steels type L and MR that have been re-nitrogenized to add strength and rigidity to their existing characteristics.

Tinplating was originally performed by means of the hot dipping process. In this process, base steel sheets or continuous strips are coated to equal extents on both surfaces while passing through a bath of molten pure tin. During this step, the intermetallic compound $FeSn_2$ is spontaneously formed at the interface between tin and base steel.

The main limitations and disadvantages of this technology were as follows [7]:

- The impossibility of obtaining a uniform tin coating for each surface for a weight of tin lower than 20 g/m^2.
- Tin was applied in equal quantity to both surfaces of the base steel.
- The process was slow and expensive.

Electrolytic tinning or electroplating of tin was developed in the 1930s and since 1960 has been the main process for tinplate production [7]. **Figure 3** shows the main stages of the electrolytic process for tinplate production.

Figure 3 Schematic representation of the electrolytic process for tinplate production.

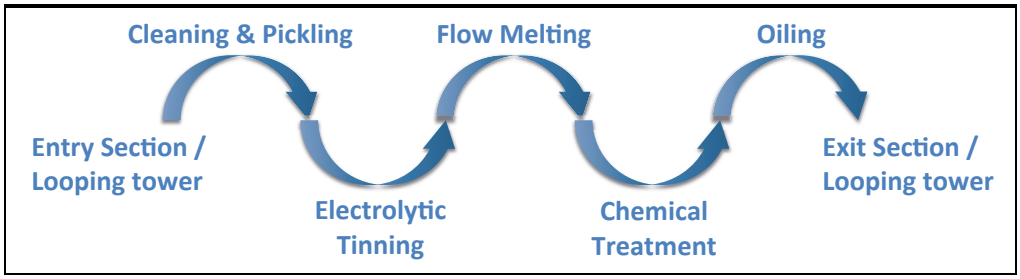

Electrolytic tinning:

In the electrolytic process, after cleaning and pickling, the base steel strip passes through the electroplating tank. Electrolytic tinning can be performed using traditional anodes made of 99.9% pure tin (99.85% is the minimum required purity) or inert anodes made of titanium and coated with platinum or iridium oxide [6-7].

Flow melting:

Immediately after electrolytic tinning, the tin coating has a matt light grey appearance and no $FeSn_2$ alloy is formed at the tin-base steel interface. The bright mirror-like finish and the $FeSn_2$ alloy are achieved by means of the flow melting process. In the flow-melting step, the tin coated strip is heated by induction or resistance above the melting point of tin (typically 260–270 °C) for a few seconds and then rapidly quenched in water [2,7,8]. Covert et al. [10] determined that the $FeSn_2$ alloy produced in the electrolytic process is an extremely brittle compound composed of singular rectangular acicular grains with a density of 7.743 g/cm^3.

The role of the $FeSn_2$ alloy was not well understood when the electroplating process was introduced. The flow melting process was carried out initially only for aesthetic purpose to brighten the tin coating [11]. However, it soon became clear that the $FeSn_2$ alloy was fundamental for resistance of the overall tinplate structure to corrosion [11].

According to the literature [2,7,8,10-17], the $FeSn_2$ alloy enhances the corrosion resistance of tinplate because is supposed to be a chemically inert barrier, which avoids the galvanic coupling between tin and base steel.

Gabe at al. [11,15,16] in their studies of isolated $FeSn_2$ alloys pointed out that the coverage and structure depend greatly on the tinplate production process. The alloy formed during the hot-dipping process has a nodular appearance and

extremely high coverage, while that produced by means of a flow-melting process has an acicular shape and low coverage. **Figure 4** shows the SEM images, examined in transmission, of the isolated alloy layer reported by Gabe at al. [15].

Figure 4 Isolated alloy in transmission at 16.000 X magnifications, source Gabe et al. [15].

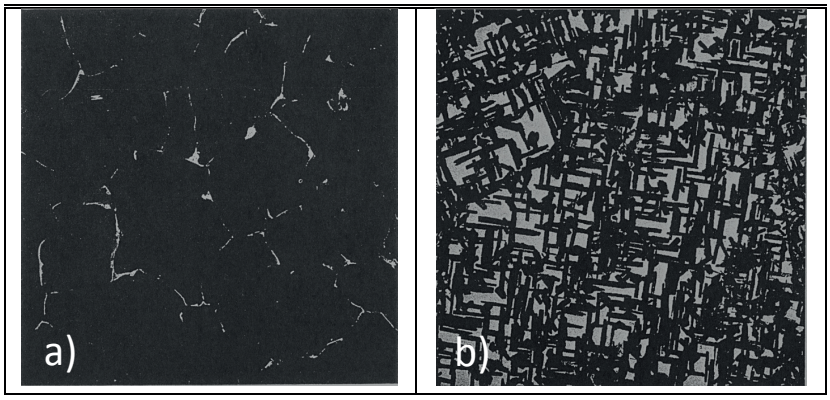

Since the flow-melting stage of the electroplating process became the main process for alloy formation, the mechanism and kinetics of the growth of tin iron alloy have also been investigated [12,13,14,17]. Biber et al. [12] demonstrated that the growth mechanism and rate of the $FeSn_2$ alloy on pure iron depends on the orientation of the iron crystals. However, on base steel, which does not present a preferential crystal orientation, the $FeSn_2$ alloy layer appears as a combination of rectangular crystallites of different dimensions and directions [12].

Gabe et al. [14], Frankenthal et al. [13] and Sarafianos [17] determined that growth of the FeSn2 alloy takes place through a diffusion-controlled mechanism and is temperature dependent according to Arrhenius' law.

In the last few decades, the flow-melting stage has been optimized to obtain a cost-effective material able to provide a few months more resistance than the conventional shelf life of canned foods.

Chemical treatment and oiling:

At the end of the tinplate production process, a thin passivation layer (<1 µm) of chromium oxide is formed on the tinplate surface by means of an electrolytic treatment in a sodium dichromate solution. This passivation layer protects tinplate from atmospheric corrosion and prevents the formation of tin oxides on the surface.

The presence of tin oxides may result in unsightly staining on the container and negatively affect the adhesion of organic coatings [8].

The surface is afterwards lightly oiled to render it more stable and resistant to the atmosphere [2,3,7,8]. The most common food grade oils used are dioctyl sebacate (DOS), butyl stearate (BSO) and acetyl tributyl citrate (ATBC). These are applied in a quantity in the range 2.5–9.9 mg/m^2 [7].

Electrolytic tinplate classification:

With respect to hot dipping, electroplating offers four benefits [7,8]:

- The amount of tin deposited can be strictly controlled, down to a lower weight of 1.1 g/m^2. However, such low coating masses are used only for limited applications, i.e. cans for pet food but not for human food applications.
- "Differential" coatings can be produced, with tin applied in different quantities to the two faces of the base steel.
- Manufacturing costs can be reduced.
- The production rate can be increased to 350–600 m/min.

Determining the thickness of the tin layer is not a trivial matter, since it depends on the roughness of the base steel, the flow-melting process, etc. Thus, tinplates are conventionally classified according to the nominal tin mass applied. However, in modern tinplates, the average thickness of the tin layer is generally between 0.2 µm and 1.6 µm. ASTM and EN standards classify tinplates according to the nominal masses of tin coating applied. The nominal coating masses of tin referred to in the ASTM and EN standards are summarized in **Table 2**, in which the two numbers separated by the fraction slash identify the nominal coating mass applied to each surface.

Table 2 Classification of standard grades of electrolytic tinplate as reported by Robertson [2].

Code		Nominal Coating Mass per Surface	
EN (145–146)	**ASTM (624–626)**	**(g/m^2)**	**lb (Pound)/Base Box (20.2325 m^2)**
-	No. 10	1.1/1.1	0.05/0.05
E 2.8/2.8	No. 25	2.8/2.8	0.125/0.125
E 5.6/5.6	No.50	5.6/5.6	0.25/0.25
E 8.4/8.4	No. 75	8.4/8.4	0.375/0.375
E 11.2/11.2	No.100	11.2/11.2	0.5/0.5
D 2.8/0	-	2.8/0	0.125/0
D 5.6/2.8	No. 50/25	5.6/2.8	0.25/0.125
D 8.4/2.8	No. 75/25	8.4/2.8	0.375/0.125
D 11.2/2.8	No. 100/25	11.2/2.8	0.50/0.125
-	No. 135/25	15.1/2.8	0.675/0.125
D 8.4/5.6	No. 75/50	8.4/5.6	0.375/0.25
D 11.2/5.6	No. 100/50	11.2/5.6	0.5/0.25
D 15.1/5.6	-	15.1/5.6	0.675/0.25

E, equal coating on each surface; D differential coatings on each surface

1.2.2 Tinplate characterization

Since the introduction of tinplate, several methods for the analysis of its stratigraphy have been developed [7,8]. These methods are compiled and described in the standards ASTM A623-16, ASTM A630-03 (2014) and UNI EN 10101:2004 [9,18,19].

The most relevant characterization methods aim to determine:

- Tin coating mass.
- Porosity of the tin layer.
- $FeSn_2$ alloy coverage.

Tin coating mass determination

- *Electrochemical method:*

The chrono-potentiometric stripping method is most widely used for tin coating mass determination because it makes it possible to discriminate between the free tin present in the tin layer and the tin alloyed to iron as the $FeSn_2$ alloy. The method was developed by Kunze et al. [20] and later integrated in the standards UNI EN 10101:2004 [18] and ASTM A630-03 2014 [19]. The method is based on galvanostatic polarization of the tinplate in 1 M HCl at 9.7 mA/cm^2. The corresponding chrono-potentiometric curves exhibit two distinct potential plateaus, which correspond to

the dissolution of the free tin layer and the alloyed tin, respectively (**Figure 5**). The charge associated with each plateau is then converted in the mass of dissolved tin by means of Faraday's equation.

Figure 5 Typical representation of a chrono-potentiometric stripping curve of tinplate.

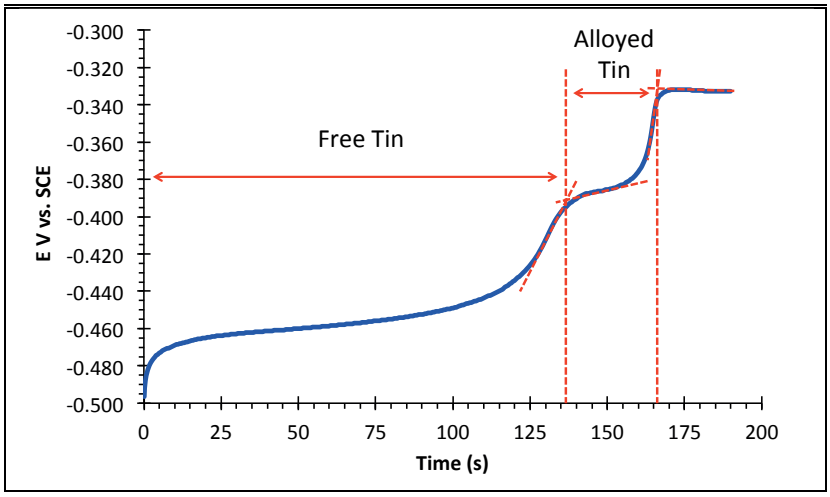

- *Non-destructive method:*

The X-ray fluorescence emission technique (XRF) allows the rapid and non-destructive quantification of elements heavier than oxygen. With this technique, the elements constituting a sample can be detected and quantified, after being excited with a primary X-ray beam, by the emission of their own characteristic fluorescence X-rays. The method does not require a controlled atmosphere and thus is conventionally adopted for in-line quality control of tinplate. However, this technique does not discriminate between free and alloyed tin [7].

- *Chemical method:*

The Bendix test, Sellars' method and the titration method are the three chemical methods for tin mass determination described in ASTM A630-03 2014 [19]. The methods are based on direct titration or back titration of the tin dissolved from tinplate in hydrochloric acid. However, these methods do not distinguish between free and alloy tin either.

Porosity of the tin layer

The porosity of tinplate is an important parameter used to characterize its corrosion resistance. This is defined as the iron exposed through the tin layer porosity and the acicular structure of the $FeSn_2$ alloy. This parameter, called the iron exposure value (IEV), is quantified according to the method proposed by Tsurumaru et al. [21]. This method is based on chrono-amperometry measurements carried out at 1.2 V vs. SCE in a buffer solution at pH 10 (250 cm^3) of 0.02 M Na_2CO_3, 0.02 M $NaHCO_3$ and 0.005 M NaCl. Under these electrochemical conditions it has been verified that the current from pure tin or a surface covered by a homogeneous layer of $FeSn_2$ alloy is negligible compared to the current from base steel. Thus, the current measured after 180 s of stabilization at the imposed potential is directly related to the exposed iron. Later, Milanese et al. [22] found that the higher the IEV value, the higher the corrosion rate of tinplate.

Notter et al. [23] proposed a method based on the determination of tinplate porosity from the measurement of its polarization resistance in ammonium thiocyanate solution. However, this method is not suitable for the determination as it leads to an overestimation of the exposed base steel. This is due to the fact that in thiocyanate solution the $FeSn_2$ alloy and the chromium passivation layer are also both reactive and therefore they will be considered in the overall porosity.

$FeSn_2$ alloy coverage determination

The structure and coverage of the $FeSn_2$ alloy can be characterized by microscopy analysis of the isolated alloy as done by Gabe at al. [11,15,16], or according to the alloy-tin couple (ATC) test described in the standard ASTM A623-16 [9]. This test, developed by Kamm et al. [24], is based on measurement of the current flowing between a tin electrode and a tinplate sample, previously electrolytically detinned, in 5% NaOH until reaching the alloy layer. The test is carried out in the absence of oxygen, in grapefruit juice diluted 3:1 with distilled water containing 500 ppm of potassium sorbate and 100 ppm of stannous chloride. The ATC value is the current expressed in $\mu A/cm^2$ measured after 20 h of coupling. ASTM A623-16 [9], however, specifies that this test can be applied to tinplates with nominal masses of tin > 5.6 and that the ATC values are strongly dependent on the electrolyte. The ATC values

measured in artificial electrolytes are not comparable with the values obtained in tests carried out in the conventional grapefruit juice solution [24].

Gabe et al. [11,15,16] correlate the ATC value to the $FeSn_2$ alloy coverage (**Figure 6a**). The correlation was done by means of the optical analysis of the transmission images of isolated $FeSn_2$ alloy from several customized tinplate samples. The study shows that the range of ATC values of commercial hot-dipped tinplates and electrolytic tinplates were 0.05–0.2 µA/cm^2 and 0.02–0.05 µA/cm^2, respectively.

Figure 6b shows that according to the ATC value, the $FeSn_2$ alloy of electrolytic tinplate has coverage of between ≈50% and 99%, while for tinplate produced by means of the hot-dipping process the coverage is between 85% and ≈100%.

Figure 6 Relationship between the ATC value and the FeSn2 alloy coverage, from Gabe et al. [11,15,16].

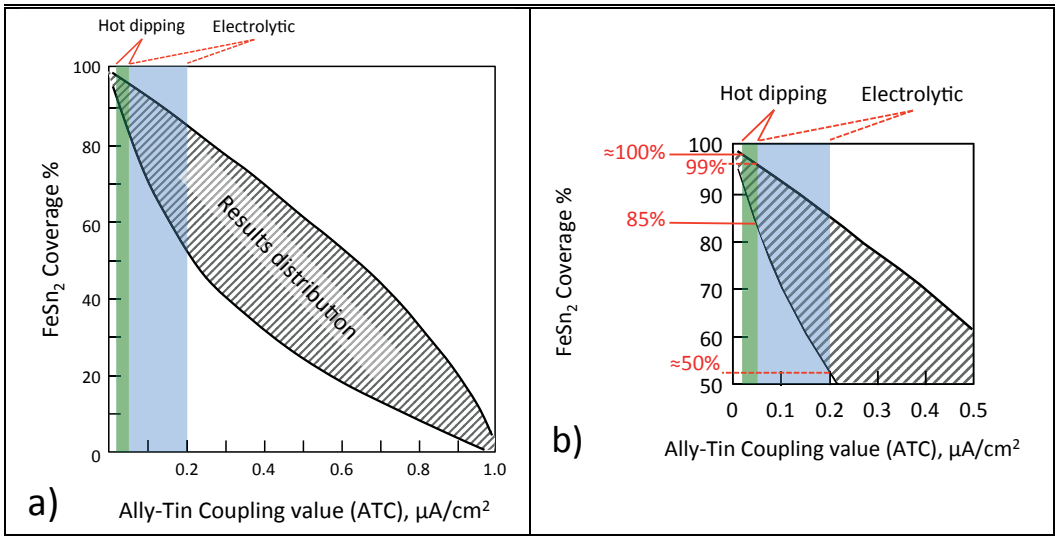

More recently, surface analysis methods have been used to characterize the overall tinplate structure by means of depth profiling techniques. Ramamurthy et al. [25], Lu et al. [26] and Sarafianos [27] used dynamic secondary ion mass spectroscopy (SIMS) and Auger electron spectroscopy (AES) for the characterization of commercial tinplate samples. From the 3D dimensional analysis of SIMS images of several electrolytic tinplate samples, Ramamurthy et al. [25] highlighted the presence of iron-rich regions on the surface of tinplate coated with low masses of tin. These regions corresponded to the porosities or rolling marks of the base steel. Lu et al. [26], using the same method, pointed out that roughness induced by the rolling of

the base steel is responsible of the non-homogeneous thickness of the tin layer present on the tinplate surface. Sarafianos [27], through analysis of the AES depth profiles, pointed out the presence of a wide diffusion region (0.2–0.3 μm thick) at the tin-steel interface. The formation of this region is attributed to diffusion phenomena taking place during flow melting. In the diffusion region, the tin signal constantly decreases to zero, while that of iron increases up to 100%; no constant tin-iron signal ratio induced by the presence of the $FeSn_2$ alloy is detectable. Also Lu et al. [26] highlighted the impossibility of clearly detecting the $FnSn_2$ alloy at the tin-iron interface.

1.2.3 Food corrosivity

In the corrosion of food cans, the nature of the food and its interaction with the tinplate play a key role. Canned foods are extremely complex systems, covering a wide range of pH and buffering properties. Moreover, they also contain several molecules and ions acting as corrosion accelerators, such as nitrates, anthocyanins, sulphur dioxide, sulphur, oxygen, etc. In contrast, essential oils, sodium dodecyl sulphate and organic species such as agar-agar, gelatine and pectin are known to be corrosion inhibitors. Based on the experience of canned food producers, foods are classified according to the following four general corrosivity grades [2,3]:

- Mildly corrosive media (corn, peas, fish and meat).
- Moderately corrosive media (pears, citrus fruits, apples and tomato juice).
- Highly corrosive media (grape and apple juice, prunes, berries, cherries, sauerkraut and pickles).
- Strong detinners (green beans, tomato products, asparagus and spinach).

This previous classification should only be taken as an indication because the corrosivity of foods is highly sensitive to chemical composition and for the same food it may change as a function of the production region or season. This difference in corrosivity can furthermore be amplified by differences in the production processes and in the storage conditions after retailing [2]. The chemical parameters known to affect the corrosion of tinplate are reported in the literature [2,3,28-33].

Acidity and pH:

Typically, canned foods are acidic environments with a pH < 6. However, there is no direct correlation between pH and the degree of tinplate corrosion [2,3,29]. A literature review on the corrosivity of canned fruits reported by the Food and Agriculture Organization (FAO) [29] pointed out that the role of pH is not fundamental for tinplate corrosion. On the contrary, there appears to be greater relevance for the effect of the chemical nature of the anions of the acids, their concentration and the other molecules contained in the fruits. Although the pH is not the principal parameter determining tinplate corrosion, Barone et al. [3] reported that the pH of canned foods more critical for the corrosion of tinplate is in the range 3–4.5. Tinplate corrosion does not decrease below pH 3; however, foods with a pH < 3 are not conserved in tinplate cans.

Presence of complexing agents:

Anions of organic acids, such as tartaric, malic citric and oxalic, are common complexing agents for tin ions contained in canned fruits and vegetables. Citric acid, due to its buffer properties, is also conventionally added to several canned foods as a pH modifier/stabilizer. The complexes formed between tin and complexing agents have been studied by several authors [34-37]. Sherlock et al. [34] reported that the tin-ligand complex has a stoichiometry of order one for citrate, malate and tartrate anions, while the stoichiometry is of order two in the presence of oxalate anions. This was confirmed by Jarosz et al. [37]. However, more recently Lamberig et al. [36] have determined for the citrate complex a stoichiometry of order two.

Despite the complexation order, all authors in the literature agree on the effect and function of complexing acids. Their presence reduces the activity of free tin ions in solution and thus the tin electrode potential shifts towards the cathodic direction [2,3,28-30,34-40]. This cathodic shift due to the presence of complexing agents determines the relative position of the corrosion potentials of tin and base steel conditioning galvanic corrosion [2,3,35,38,39]. The optimal condition for tinplate cans is when the corrosion potential of the tin is lower than that of the base steel. In this situation, the tin layer works as a sacrificial anode, while the base steel is protected from perforation. **Table 3** lists the corrosion potential of tin and iron and

the polarity of the tin-iron couple determined by Gouda et al. [38,39]. In the relevant range of pH for canned foods (3–4.5), tin has a lower corrosion potential than base steel for citrate and oxalate buffer concentration ≥ [0.01]. Willey et al. [35] found that in fruit juices, the concentration of the major complexing acid (citric, tartaric or malic) is in the range [0.01]–[0.1]. Willey also pointed out that the difference in corrosion potential for tin and steel depends on the complexing strength of the anions. Tin dissolution increases with the complexing strength of the ligands compared to the stannous ions as reported by Gouda et al. [38] and Sherlock et al. [39].

Table 3 Dependence of the corrosion potential of tin and steel and the polarity of the tin-iron couple as a function of the type of buffer, its pH and its concentration. Data from Gouda et al. [38,39]. The conditions in which tin has a lower corrosion potential than steel are highlighted in green.

	Corrosion potential after 17 hours of stabilization E_{corr} (V vs. SCE)							
	pH 2		**pH 3**		**pH 4**		**pH 5**	
	Sn	**Steel**	**Sn**	**Steel**	**Sn**	**Steel**	**Sn**	**Steel**
[Citrate] (mol/L)								
10^{-5}	-0.500	-0.565	-0.530	-0.580	-0.570	-0.592	-0.240	-0.605
10^{-4}	-0.540	-0.575	-0.570	-0.595	-0.605	-0.620	-0.360	-0.630
10^{-3}	-0.570	-0.585	-0.600	-0.610	-0.630	-0.650	-0.530	-0.665
10^{-2}	-0.615	-0.540	-0.630	-0.568	-0.670	-0.630	-0.696	-0.694
10^{-1}	-0.650	-0.510	-0.680	-0.550	-0.705	-0.609	-0.754	-0.680
[Oxalate] (mol/L)								
10^{-5}	-0.520	-0.530	-0.560	-0.570	-0.595	-0.600	-0.225	-0.620
10^{-4}	-0.560	-0.555	-0.600	-0.585	-0.635	-0.635	-0.350	-0.650
10^{-3}	-0.600	-0.570	-0.640	-0.600	-0.670	-0.685	-0.500	-0.695
10^{-2}	-0.640	-0.525	-0.680	-0.555	-0.720	-0.642	-0.665	-0.700
10^{-1}	-0.680	-0.490	-0.720	-0.530	-0.760	-0.620	-0.750	-0.680

Content in oxidants:

Protons and oxygen are the main oxidants present in canned food. Besides these, the other molecules known to enhance tinplate corrosion are sulphur dioxide, sulphur, nitrates, trimethylamine oxide and anthocyanins [2,3,28-33].

The presence of protons is due to the acidic environments characterizing most canned fruits and vegetable, while the oxygen is naturally contained in the biological structures of food, is dissolved in the aqueous matrix and is present in the headspace

of the can. Hot-filling, exhausting, vacuum-filling steam injection and minimization of the headspace are the techniques normally adopted during canning to minimize the oxygen content [2,3,28-31].

Sulphur products can be present in foods as residues of agricultural chemicals, or can originate from the degradation of proteins contained in meat, fish and certain vegetables. The increase in the tin dissolution rate due to the presence of sulphur dioxide was confirmed in the work of Saguy et al. [31]. Sulphur dioxide is reduced to sulphide or sulphur on the tinplate surface. Sulphides combined with iron and tin ions form unsightly black and blue/brown stains, respectively [2,3,28-31].

Nitrates are contained in high concentrations in green beans, spinach, beets, lettuce and turnips. However, significant concentrations of nitrates (up to several hundred ppm) can also be encountered in fruits and vegetables grown in heavily fertilized soils [2,3,28-33]. Saguy et al. [31] and Albu-Yaron et al. [32] showed that an increase in nitrate concentration leads to a great increase in the tin dissolution rate. The following aspects characterize the proposed nitrate corrosion mechanism [2,3,28-32]:

- The reduction of nitrate ions to ammonium ions involves proton consumption; therefore the process is pH dependent. At pH values > 5.5, the presence of nitrates is much less problematic.
- The reaction of tin dissolution is catalysed by ferrous ions. As soon as Fe(II) ions are available, they are oxidized to Fe(III) by nitrate ions. Afterwards, Fe(III) ions are reduced through tin oxidation.

Anthocyanins contained in plant pigments are strong tinplate corrosion accelerators [2,3,33]. According to the mechanism proposed by Salt et al. [33], the reduction of the oxonium ring of anthocyanins is much faster than the highly inhibited cathodic process of hydrogen reduction. Furthermore, the hydroxyl groups present on the anthocyanins rings are responsible of the formation of insoluble complexes with tin. The precipitation of the complexes on the tinplate surface favour electron transfer from the tin to the oxonium group of anthocyanins.

Inhibitors:

Other species naturally present in food or used as additives can act as corrosion inhibitors. Substances able to adsorb on tin or iron may act as corrosion inhibitors. According to the Langmuir isotherm [41], the number of sites available for the adsorption of oxidizing species will decrease with an increase in inhibitor adsorption. El-Sherif et al. [42] and Albu-Yaron [32] respectively reported that tin release decreases in the presence of glycine and ascorbic acid. Grassino et al. [43,44] confirmed the inhibiting effect of essential onion oil applied by spraying the tinplate before filling or directly added to the food. However, the inhibitory effect was only present at room temperature, while for storage at a temperature > 36 °C an acceleration of the tin dissolution was observed. This effect was attributed to the action of essential onion oil degradation compounds adsorbed on the metallic surface. Later, Barone et al [3] indicated also that sodium dodecyl sulphate (an emulsifying agent) and organic species such as agar-agar, gelatine, pectin and garlic oil could potentially be considered as corrosion inhibitors.

1.2.4 Tinplate corrosion and modelling

Corrosion of tinplated cans originates through the interaction of the metallic container with corrosive food. The complexity of the tinplate structure and of the chemistry of the foods makes the corrosion of tinplate an extremely complex phenomenon.

This section illustrates the methods commonly used to determine tinplate corrosion, the corrosion rates measured in the literature and the models currently available to describe tinplate corrosion.

Method for the determination of the tinplate corrosion rate:

The corrosion rate of tinplate is conventionally assessed in de-aerated model electrolytes, such as citrate, malate, tartrate and oxalate buffers. Real foods are less used for fundamental studies, but are widely used in the case of package tests. The corrosion rate of tinplate is conventionally measured by means of an immersion test or by electrochemical analysis.

In the immersion test, the amount of dissolved tin and/or iron due to corrosion is quantified by means of spectroscopy techniques, such as atomic absorption spectroscopy (AAS), or more recently through inductive coupled plasma (ICP) spectroscopy. The analysis of the electrolytes is carried out after several days or months in contact with tinplate specimens in sealed containers. Alternatively, it is possible to measure the amount of metals released into the food during package tests. This method allows the estimation of the average corrosion rate over a period of time, but does not provide information on the mechanisms involved. Conversely, electrochemistry, by means of potentiodynamic polarization and polarization resistance, allows assessment of the corrosion rate and furthermore is a powerful method for the study of the corrosion mechanisms involved [45].

Sherlock et al. [45] used both methods for measuring the corrosion rate of tinplate in standard citrate solution (**Table 4**). They pointed out that the corrosion rates of tinplate extrapolated from the cathodic and anodic Tafel lines of potentiodynamic polarization are always larger than the corrosion rate calculated from the dissolved tin by AAS. The reason is that the residual oxygen present at the beginning of the immersion test is rapidly consumed by the corrosion of large specimens (10 cm^2) in a small volume of electrolyte (23.5 ml). Thus, for an immersion test carried out over 70 days, the effect of the oxygen reduction contribution becomes negligible. In contrast, the corrosion rates measured by means of electrochemical methods can be amplified by the presence of residual oxygen that could not be completely removed during the de-aeration phase.

Corrosion rate of tinplate:

Table 4 shows the corrosion rate of tinplate determined in two relevant studies. Bombara et al. [40] demonstrated that the corrosion rates obtained in citrate model electrolytes are close to those measured in fruit juice. However, the values obtained are extremely high compared to the available thickness of the tin coating. According to these corrosion rates, the lifetime of cans would be less than one year. The reason for this overestimation of the corrosion rate of tinplate has been attributed to the presence of residual oxygen affecting the electrochemical analysis. In contrast, Sherlock et al. [45], achieving better de-aeration conditions, measured corrosion

rates one order of magnitude lower than in Bombara et al. [40]. Moreover, comparing the results of tinplate with those of pure tin, they demonstrated that as long as the tinplate surface is coated with a homogeneous tin layer, the corrosion rate of tinplate is low and close to that of pure tin (**Table 4**).

Table 4 Experimental values for the corrosion rate of tinplate from relevant literature.

Author	Material	Electrolyte	De-aeration	Method	Corrosion rate (µm/y)
Bombara et al. [40]	Electrolytic tinplate type E 11.2/11.2	Citrate buffer, pH 2	YES	[1]PP, extrapolation at the Tafel lines interception	7
		Citrate buffer, pH 3.8			4
		Citrate buffer, pH 5			3
		Citrate buffer, pH 8			1.5
		Grapefruit juice, pH 3.2			5
		Pineapple juice, pH 3.8			4
		Tomato juice, pH 4.2			2.5
		Peach syrup, pH 3.9			4
Sherlock et al. [45]	Tinplate type 22 g/m^2	Citrate buffer pH 4, [0.05]	YES	[2]AAS, after 70 days of immersion at 30 °C	0.2–-0.4
	Pure tin	Citrate buffer pH 4, [0.05]			0.2
	Tinplate type 22 g/m^2	Citrate buffer pH 4, [0.05]		[2]PP, Tafel method at 30 °C	0.9–2.6
	Pure tin	Citrate buffer pH 4, [0.05]			0.5

[1] Potentiodynamic polarization (PP); [2] atomic absorption spectroscopy (AAS)

Modelling of tinplate corrosion:

The first attempt to describe and model tinplate corrosion was made in 1957 by Koehler et al. [46]. They identified general factors directly related to the lifetime of tinplate, despite the pack data of previous studies indicating that every product behaves in a different way [46]. In their work, they stated that the lifetime of tinplate cans is divided in two periods: a first period corresponding to a surface totally covered by tin and a second period characterized by the co-exposition of the

tin, iron and $FeSn_2$ alloy. The following two groups of factors determine the duration of each period.

Factors determining the duration of the first period:

- Thickness and uniformity of the tin coating.
- Oxidants contained in the food.
- Possible influence of natural corrosion inhibitors.
- Structure of the tin coating.
- No effect of the base steel.

Factors determining the duration of the second period:

- Anodic properties of the base steel.
- Inhibitors present in the food.
- Properties of the steel or steel surface influencing its power to adsorb certain of these inhibitors.
- Known and unknown factors influencing the potential relationship between steel and tin.

Despite the identification of the previously listed factors and the important studies carried out by Kamm et al. [24,47] and Britton et al. [48] regarding the effect of the $FeSn_2$ alloy coverage and the tin-steel galvanic coupling, no effort has been devoted to combining all these results in a complete model able to describe and predict the corrosion of tinplate as a function of the structure of tinplate and the content food.

Up to now, there has only been an empirical model describing the release of tin from tinplate due to its corrosion. The lifetime of tinplate cans corresponds to the period of edibility of the food contained in the can. Canned food is considered not edible after the nominal expiration date or when the maximum levels of dissolved tin are reached due to corrosion. The legal limits for dissolved tin are 200 ppm for canned food, 100 ppm for canned beverages and 50 ppm for canned baby food [2]. There has only been weak interest in the modelling of long-term corrosion of tinplate cans because – from an industrial point of view – a can no longer serves any purpose as soon as its content is no long edible. However, museum collections need predictive models over longer periods. **Figure 7** shows the trend of tin release as a

function of storage tin, which is commonly used for describing the tinplate corrosion in acidic foods [2,3,28,30]. This trend is based on empirical studies and does not take into account the mechanisms involved. Mannheim et al. [30] state that during the lifetime of plain tinplate cans, tin is released at three different rates according to the storage time:

- 1^{st} stage: During this first period, the oil and tin oxide layers are removed from the internal surface. The high rate of tin dissolution is due to the reduction of the residual oxygen and the oxidant species present in food.
- 2^{nd} stage: This is the longest stage and is characterized by slow tin dissolution taking place at an almost constant rate. The corrosion of the pure tin layer leads to the enlargement of existing pores and defects, thus increasing the exposed areas of $FeSn_2$ and the underlying base steel. The base steel exposed through the $FeSn_2$ alloy provides catalytic sites for the hydrogen evolution reaction (HER). The tin-base steel areas ratio dictates the corrosion rate of tin. Homogeneity rather than the amount of the inert $FeSn_2$ alloy control the exposure of the base steel and the galvanic coupling effect.
- 3^{rd} stage: During the last stage, tin dissolution increases exponentially due to the exposure of large areas of base steel, which catalyses the HER. The accumulation of molecular hydrogen increases the internal pressure, inducing swelling and eventually bursting of the container.

  As previously mentioned, this last stage has tended to be of little industrial importance because by this time the food has reached the end of its shelf life. However, this stage it is extremely important for museum collections in which cans reach this critical condition and start to degrade.

Figure 7 Empirical evolution of tin dissolution with aging as reported in the literature [2,3,28,30].

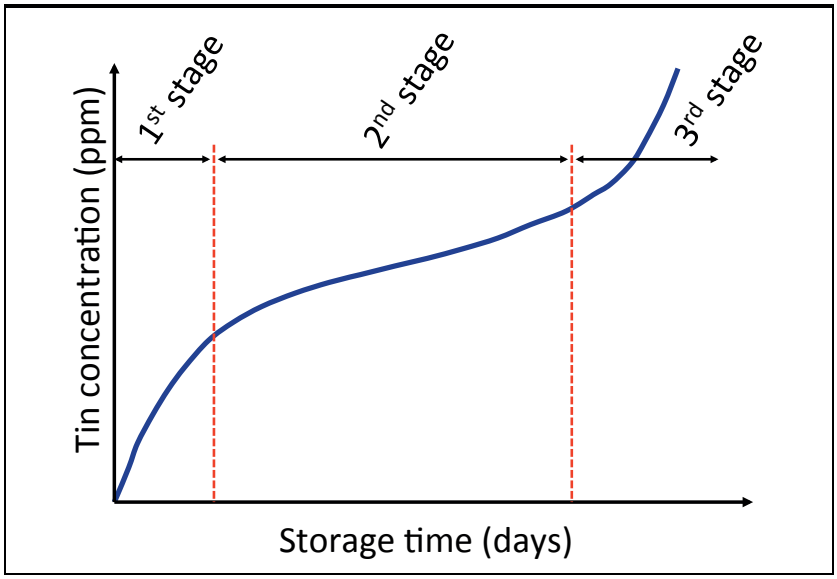

According to Mannheim et al [30] and Gabe et al. [15], the typical scenarios describing the internal corrosion of tinplate cans are as follows:

- Normal detinning takes place in anaerobic conditions and in the presence of complexing agents of tin ions. In this situation, the tin layer acts as a sacrificial anode towards the base steel. Acid corrosion of tin and the HER at the exposed steel sites occur at a slow rate.
- Rapid detinning generally characterizes the first and the last periods of the life of tinplate cans. However, this phenomenon may be originated by the use of tinplate coated with low masses of tin or by an imperfect sealing of the can.
- Localized corrosion may take place in anaerobic conditions and in the absence of complexing agents. In these conditions, tin no longer behaves as a sacrificial anode and localized corrosion attacks occur at the exposed iron sites. This situation is unusual, but may occur in highly corrosive products (pickles and carbonated beverages containing phosphoric acid). Interestingly, Brambilla et al. [6] showed that this situation is a common degradation phenomenon in cans in museum collections.

For the long-term prediction of tinplate corrosion, a more rigorous approach combining structural information on tinplate and the kinetics of corrosion reactions is needed. Information on the tinplate structure has to be combined with the

corrosion mechanisms and kinetics responsible of the dissolution of the pure tin, of the interface constituted by the tin-base steel-$FeSn_2$ alloy and the base steel. For these reasons, the literature review will continue focusing on the following aspects:

- tin corrosion;
- galvanic coupling between tin and steel;
- electrochemical behaviour of the $FeSn_2$ alloy;
- base steel corrosion.

1.2.5 Tin corrosion

The low corrosion rate of tin makes the tin layer the principal barrier against the corrosion of tinplate. This section includes a general overview of the electrochemical behaviour of tin and a more detailed literature review on the mechanisms responsible of tin corrosion in the typical conditions of food cans.

Electrochemical behaviour of tin:

Figure 8 shows that according to thermodynamics, tin dissolves actively in acidic media with a pH < 3.5, while in slightly acid, neutral or alkaline media (pH 3.5 to pH 9) tin oxidizes first to $Sn(OH)_2$ and at higher potential to $Sn(OH)_4$. In acidic media, these hydroxides are not stable and dissolve as Sn(II) and Sn(IV) ions. SnO_2 is formed by the crystallization and dehydration of $Sn(OH)_4$ or by the direct oxidation from metallic tin [49]. However, the tin surface is converted by SnO_2 only if the metal is exposed to the air [49]. Many relevant studies on the electrochemical behaviour of tin have focused on the study of the passivation mechanism of tin in acidic citrate buffers [50-56], neutral phosphate buffers [57-58] or in basic solutions [59-61]. In passive conditions, several authors [50,52,62,63] have shown that tin suffers from pitting corrosion. However, it has been demonstrated that in acidic de-aerated solutions, such as canned food products, tin undergoes active dissolution [40,49]. Thus, the following paragraphs of the literature review focus on the mechanisms and kinetics of the active corrosion of tin in the complexing environments typical of canned fruits and vegetables. Tin passivity and pitting corrosion are not considered further.

Figure 8 Potential pH equilibrium diagram for the tin-water system with activity of tin ions of 10^{-6}, at 25 °C. The diagram considers the hydroxides $Sn(OH)_2$ and $Sn(OH)_4$ [49].

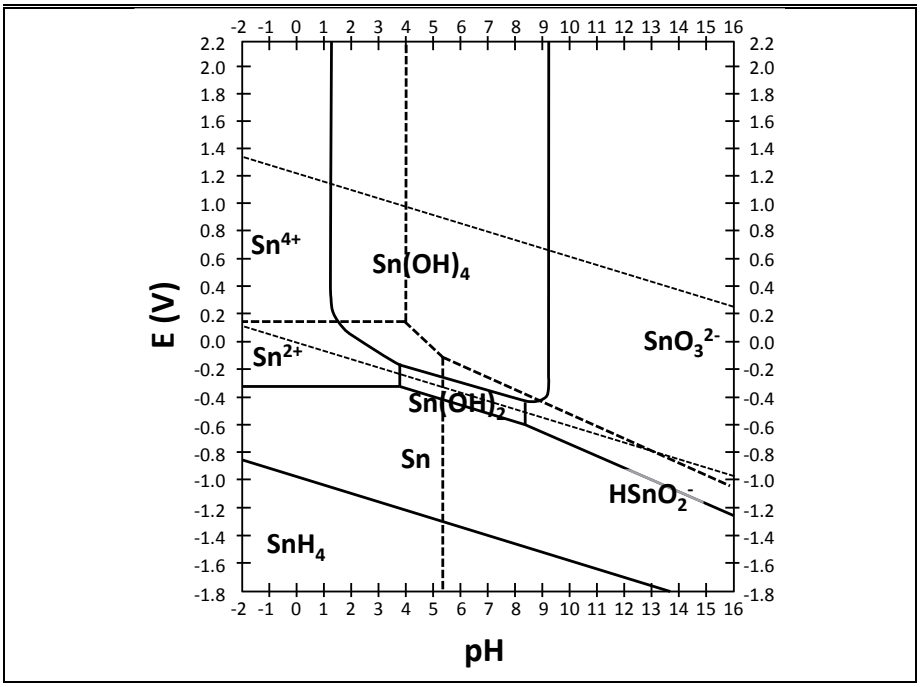

Cathodic reactions responsible for tin dissolution:

In the absence of the previously cited food-specific oxidants, the principal cathodic reactions for the buffer systems relevant to this work are the HER and the oxygen reduction reaction (ORR), as shown in **Eq. 1** and **Eq. 2** respectively:

$$2H^+ + 2e^- \rightarrow H_2 \quad (1)$$

$$O_2 + 2H_2O + 4e^- \rightarrow 4OH^- \quad (2)$$

The protons come from the acidic buffers, while traces of oxygen are naturally present due to the filling process of the cans. In the absence or very limited concentration of oxygen, the corrosion reaction of tin is under cathodic control and the rates of these HER and ORR reactions determine the rate of tin corrosion [40].

The high overpotential for the HER highlighted in the literature is due to the weakness of the tin-hydrogen bond. This inhibits the adsorption of hydrogen and determines a very low exchange current density for the hydrogen electrode on tin (≈10^{-7} mA/cm^2). The adsorption of reduced hydrogen atoms on the metal surface is a fundamental step for both mechanisms of the HER: the Volmer–Heyrovsky

mechanism and the Volmer–Tafel mechanism [41]. In the literature, only Azizi et al. [64] report an exhaustive study of the cathodic mechanisms of the HER on tin in de-aerated acidic media. By means of an electrochemical approach, they determined that the surface coverage of hydrogen exhibits a Langmurian behaviour and is potential dependent. However, even for the lowest applied potential, the maximum coverage did not exceed 0.07% [64]. This confirms the low energy of the tin-hydrogen bond reported by Landolt [41].

Studying the kinetics of Volmer, Heyrovsky and Tafel reactions at different potentials, Azizi et al. [64] identified the HER mechanism as a function of the applied potential. At low cathodic potentials, up to -0.5/-0.6 V, the HER mechanism is a consecutive combination of a Volmer reaction in parallel to Tafel and Heyrovsky reactions. In contrast, at high cathodic potential, < -0.6 V, the Tafel reaction becomes negligible and the HER takes place according to the Volmer–Heyrovsky mechanism [64].

Since in canned foods, the oxygen concentration is extremely low (few ppm), from the results obtained by Sherlock et al [45] and El-Sherif at al. [42], the ORR takes place with fast kinetics according to a diffusion-controlled mechanism.

Anodic reaction of tin dissolution:

The principal anodic reaction of tin is the oxidation of metallic tin to Sn(II) ions. Sn(IV) ions are only generated at higher potentials by the stepwise oxidation from Sn(II) ions [42,50,52,54,65-67] or by the direct oxidation from metallic tin [55,68].

Complexing agents such as citrate anions are also known to promote tin dissolution trough the formation of stable complexes; El-Sherif et al. [42] and Tselesh [52] showed that the passivation currents grow linearly with the citrate concentration. Conversely, the tin dissolution measured in a non-complexing solution, such as sulphate and borate buffers, is characterized by lower active currents and passivation current peaks [40,54].

Willey et al. [35] and Gouda et al. [38] showed that almost all Sn(II) ions added to a complexing buffer solution of polyprotic organic acids are bonded to the complexing anions.

Tin corrosion rate:

As shown in **Table 5**, Gouda et al. [38] and Sherlock et al. [34] demonstrated that the corrosion rate of tin increases with the stability of the tin-anion complex (**Table 6**). However, the mechanisms involved were not completely investigated and clarified and the correlation between the corrosion rate and type of anions was not clearly verified and demonstrated.

Table 5 lists the corrosion rates of pure tin determined by several authors [34,38,42,69] by means of two methods, immersion and electrochemistry, previously described in the section devoted to the determination of the tinplate corrosion rate.

In aerated conditions, El-Sherif et al. [42] measured a corrosion rate of tin four orders of magnitude higher than the values reported by Sherlock et al. [34,45]. In aerated tartaric acid, El-Sherif et al. [42] measured a corrosion rate of tin several orders of magnitude higher than the values reported by other authors [34,38,45,69].

The cathodic plateau situated between -0.6 V and -0.8 V and responsible for such high corrosion rates is consistent with the typical values for the cathodic reaction of the ORR reported by Landolt [41]. Clearly, for the electrochemical determination of the tin corrosion rate due to the HER only the removal of oxygen from the electrolytes is an extremely important issue.

Gouda et al. [38] and Drogowska et al [69] measured a corrosion rate of tin two orders of magnitude lower in de-aerated conditions compared to that measured in aerated solution. However, the corrosion rates of tin measured using this method are still incompatible with the protection provided by ≈1 µm thick tin coatings, normally longer than two years. Thus, despite all the efforts made to achieve a complete de-aeration of the systems, the measurements are likely still affected by the ORR due to the residual oxygen.

As previously highlighted for tinplate and also for tin, using immersion tests to determine the corrosion rate seems to provide the most coherent values. With this method, Sherlock et al. [34] report average corrosion rates < 1 µm/y. However, this method provides only average values and no information on the mechanisms and kinetics involved.

Clearly, in complexing systems, the mechanism of tin corrosion is under cathodic control and the corrosion rate is determined by complexing agents present in the

solution and by the simultaneous reduction of residual oxygen and protons, but there is as yet no study in the literature aimed at determining the individual contribution of the ORR, the HER and complexing agents to the overall kinetics of tin dissolution.

Table 5 Experimental values for the corrosion rate of tin in the relevant literature.

Author	Material	Electrolyte	De-aeration	Method	Corrosion rate (µm/y)
Sherlock et al. [34]	Pure tin	Oxalate buffer, pH 4, [0.05]	YES	[1]AAS, after 35 days of immersion at 30 °C	0.7
		Citrate buffer, pH 4, [0.05]			0.4
		Malate buffer, pH 4, [0.05]			0.3
		Tartrate buffer, pH 4, [0.05]			0.2
El-Sherif et al. [42]	Pure tin	Tartaric acid, pH 1.8, [0.1]	NO	[2]PP, extrapolation at the Tafel lines interception	1712
Gouda et al. [38]	99.2% tin (0.689% Cu, 0.133% Fe)	Oxalate buffer, pH 4, [0.1]	YES	[2]PP, extrapolation at the E_{corr} of the cathodic Tafel line	40
		Citrate buffer, pH 4, [0.1			21
		Tartrate buffer, pH 4, [0.1]			15
Drogowska et al. [69]	Pure tin	HCl /NaCl, pH 4, Cl^- [0.1]	YES	[2]PP, extrapolation at the E_{corr} of the anodic Tafel line	45
		HCl /NaCl, pH 4, Cl^- [0.3]			35
		HCl /NaCl, pH 4, Cl^- [0.5]			45
		HCl /NaCl, pH 4, Cl^- [0.7]			48
		HCl /NaCl, pH 4, Cl^- [1			45

[1] Atomic absorption spectroscopy (AAS); [2] potentiodynamic polarization (PP)

Table 6 Estimated stability constant of tin-anion complexes (Sherlock et al. [34])

Electrolyte	pH range	Average stability constant K
Tartrate	2.0–4.0	$4.6 \pm 1\ 10^{6}$
Malate	2.0–3.9	$2.7 \pm 0.8\ 10^{7}$
Citrate	2.1–4.0	$4.5 \pm 0.6\ 10^{7}$
Oxalate	2.0–3.6	$2.45 \pm 0.9\ 10^{12}$

1.2.6 Galvanic coupling between tin and steel

This section offers an overview of the state of the art for the mechanisms of galvanic coupling between tin and steel in food packaging. As previously explained in the section devoted to the modelling of tinplate corrosion, galvanic coupling occurs only after or in the last period of the commercial lifetime of canned food. However, in museum collections, where the lifetime should be extended for as long as possible, galvanic coupling becomes a relevant mechanism that needs to be taken into account for the long-term corrosion prediction of cans. According to the outcomes reported in the literature, once the interface of tinplate is reached, it is possible to consider the following two mechanisms:

- a direct galvanic coupling current flowing between the tin and steel;
- an indirect inhibiting effect promoted by the tin ions on the dissolution kinetics of steel.

Effect of the galvanic coupling current on the anodic dissolution of tin and iron:

As previously described in the food corrosivity section, many works in the literature [2,3,28-30,34-38,40] agree that tin coating sacrificially protects base steel because in the absence of oxygen and in the presence of complexing agents tin assumes a lower potential than iron. The standard reduction potentials for the Fe/Fe^{2+} and the Sn/Sn^{2+} couples are -0.44 V and -0.136 V vs. SHE, respectively. The reversal of the polarity of the tin-iron couple is attributed to the presence of complexing agents for tin ions, which reduces the concentration of free tin ions. This brings the reversible potential of tin below that of iron.

However, it should be pointed out that the previous explanations extracted from the literature are only based on thermodynamic considerations, while the real polarity of the tin-iron couple also depends on the kinetics of the cathodic and anodic reaction responsible for tin corrosion. Thus, the polarity of the tin-iron couple can only be defined based on the E_{corr}. As previously shown in **Table 3**, Gouda et al. [38,39] demonstrated that the reversal of E_{corr} of the tin-mild steel couple in de-aerated citrate and oxalate buffers does not occur for all pH and buffer concentrations; on the contrary, it is obtained only for buffer concentrations ≥ [0.01]

at a pH < 5. Hoar [70] observed that the reversal of the tin-iron couple is obtained only in de-aerated [0.1] citric acid and citrate buffer, while in a non-complexing environment such as sulphuric acid the E_{corr} of tin is higher than that of steel. In this latter situation, localized attack of the steel may take place at the tin layer porosities. Hoar's [70] measurements showed that when equal areas of tin and iron are coupled, tin corrodes faster and iron corrodes at a much slower rate compared to immersion alone in the solution (**Table 7**). The increase in Sn^{2+} release induced by coupling is equal to the theoretical amount of Sn^{2+} equivalent to the coupling current. Interestingly, the corrosion rate of iron also decreases if iron is immersed in the presence of tin, while the presence of immersed iron does not affect the corrosion rate of tin. Thus, it is possible to conclude that the kinetics of iron dissolution are inhibited by the presence of tin ions, while those for tin dissolution are independent of the presence of iron ions.

Table 7 Effect of galvanic coupling on the corrosion rate of tin and iron. The corrosion rates reported have been calculated from the results of Hoar [70] concerning the weight loss after the immersion test of tin and iron samples, alone and/or coupled. The test was carried out in duplicate for 48 hours in de-aerated citric acid and citrate buffer. The sample area was 2.5x2 cm.

	Corrosion rate (µm/y)							
Buffer	**Sn Alone**	**Sn + Fe in same vessel**	**Sn coupled to Fe**	**Increase of Sn corrosion rate due to coupling**	**Fe Alone**	**Fe + Sn in same vessel**	**Fe coupled to Sn**	**Decrease of Fe corrosion rate due to coupling**
Citric acid pH 2 [0.1]	10	10	97	+87	230	134	27	-109
Citrate pH 5 [0.1]	15	15	50	+35	172	100	14	-86

Britton et al. [48] studied the effect of the tin-steel area ratio on the corrosion rate of tin due to galvanic coupling. As shown in **Figure 9**, they demonstrated that the corrosion rate of tin increases with the percentage of exposed steel.

Figure 9 Amount of dissolved tin and iron from tinplate specimens (7x2 cm) partially de-tinned and immersed for 40 days at 25 °C in de-aerated [0.1] citric acid. Data from Britton et al. [48].

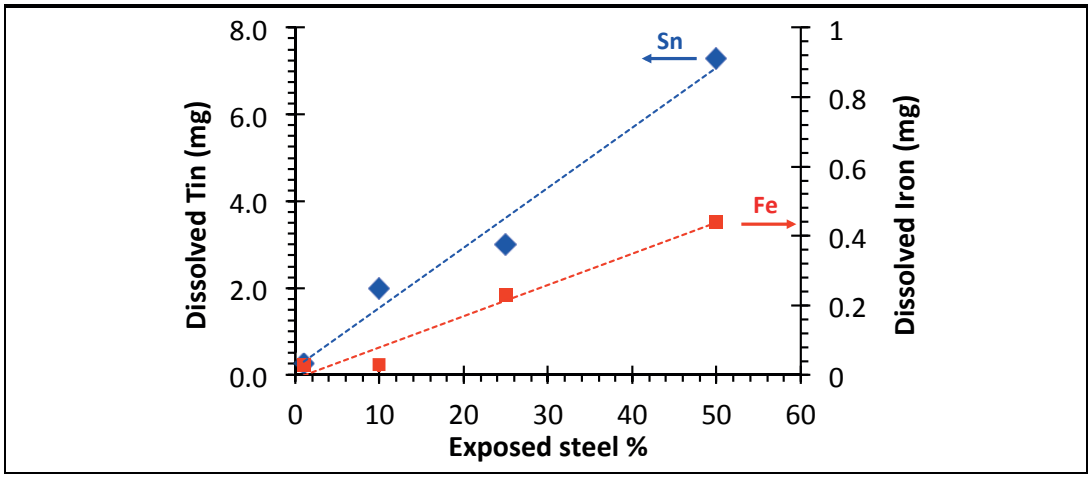

These works [48,70] clearly show that the tin-steel galvanic coupling enhances the anodic dissolution of tin and at the same time slows down the anodic dissolution of steel. However, it remains unclear why the dissolution of steel is inhibited when steel specimens are immersed in solutions containing tin ions. Koehler [71] also observed a decrease in the amount and rate of hydrogen evolution on the surface of steel coupled with tin rather than alone.

Effect of tin ions on the anodic dissolution of iron:

Several authors [47,48,70,71] have observed the reduction of steel dissolution in the presence of tin ions; however, an exhaustive description of the mechanism has only been proposed by Lamberigts et al. [36]. In 1961, Kamm et al. [47] observed that the hydrogen atoms generated on a steel plate coupled with tin or only immersed in the presence of Sn(II) ions diffuses through the steel, while in the case of pure steel all hydrogen evolves on the metal surface with a negligible diffusion. Despite these interesting findings, no further studies were carried out to clarify the phenomena involved.

Only recently have Lamberigts et al. [36] demonstrated by means of XPS analysis that tin ions are spontaneously adsorbed on the steel surface as tin-citrate complexes. This was found to be responsible for the modification of the electrochemical behaviour of steel with respect to the HER. The presence of complexes was observed in both situations, after the coupling test and after the immersion of steel in solution containing tin (II) ions. The coverage of the surface of

steel with stannous tin increases asymptotically to 34% with the concentration of tin ions introduced in the solution. However, when the steel sample was coupled with a tinplate sample 100 times larger, the coverage of the surface increased up to 83%. The enhancement of stannous ion deposition was attributed to the polarization of the steel once coupled with large tin surfaces.

Electrochemical analysis has evidenced that the presence of adsorbed tin complexes inhibits both the cathodic and anodic reactions of steel corrosion, decreasing the exchange current density. Moreover, it has been found that the adsorption of tin-citrate complexes inhibits the Tafel reaction of the chemical recombination of hydrogen-adsorbed atoms and favours the absorption of atomic hydrogen in the steel. This phenomenon was explained by the fact that tin-citrate complexes deposited on the steel surface block the chemical recombination of adsorbed hydrogen atoms, thus favouring their absorption in the steel matrix [36].

1.2.7 Electrochemical behaviour of the $FeSn_2$ alloy

In the literature, very little work has been devoted to the study of the corrosion behaviour of $FeSn_2$. Covert et al. [10] studied the corrosion potential and the hydrogen overvoltage on pure tin, pure iron and especially produced and isolated $FeSn_2$. The study highlighted that in de-aerated citric and hydrochloric acids, $FeSn_2$ has the highest corrosion potential compared to both tin and iron. This was confirmed by Luner et al. [72]. However, despite the relative position of the corrosion potentials, Covert et al. [10] showed that for the application of low current densities (≥ 10 µA/cm^2) the hydrogen overpotential of $FeSn_2$ decreases to a value between that of tin and iron. Thus, the coupling between $FeSn_2$ and tin leads to the consumption of tin at a lower rate compared to the situation in which tin is directly coupled with iron. Britton et al. [48] and Kamm et al. [24] confirmed this last hypothesis by observing that in de-aerated citric acid, tin corrodes at higher rates when it is coupled with a tinplate sample detinned to the $FeSn_2$ alloy layer. However, in these conditions, tin corrodes at a slower rate than when directly coupled to iron or steel. Covert et al. [10] determined the corrosion rates of the $FeSn_2$ alloy as 25 µm/y and 31 µm/y in solution of 4% NaCl + HCl at pH 2 and [0.1] citric acid at pH ≈2, respectively.

However, it should be highlighted that these high corrosion rates are not consistent with the inert nature of the $FeSn_2$ alloy compared to both tin and base steel, as proposed in the literature.

Comparing these corrosion rates with those of iron and steel determined by Stern [73] and reported in **Table 8**, it is clear why the $FeSn_2$ alloy seems to behave as an inert phase compared to iron and base steel. The corrosion of steel takes place through the porosities of the $FeSn_2$ alloy. The difference in the corrosion rates of these two phases leads to a fast dissolution of the steel supporting the alloy. Once the underlying steel is dissolved, the alloy becomes detached before being completely dissolved by corrosion.

1.2.8 Base steel corrosion

Base steel is the core of tinplate and gives the mechanical properties to the final material. Its thickness is 0.13–0.5 mm [7] and its corrosion resistance is poor compared to tin. **Table 8** shows the corrosion rates measured by Stern [73] for pure iron and iron containing the typical alloying elements present in the steels used for tinplate production (**Table 1**).

According to these findings, once the base steel core is in contact with the corrosive environment of the can, it will be dissolved or perforated in a much shorter time compared to the time needed for the corrosion of the protective tin coating. For can collections, an intervention needs to be performed before this stage is reached. Thus, base steel corrosion will not be investigated further in this work.

Table 8 Results of Stern [73] concerning the corrosion rates of iron and various alloys in oxygen-free acids at 25 °C.

Alloy	Corrosion rate (µm/y)	
	4% + HCl NaCl pH 2.00	**[0.1] Citric Acid pH 2.06**
Pure Fe	139	134
0.11% Cu	455	190
0.08% Si	413	209
0.017%P	2226	765
0.11% Mn	190	83
0.015% S	1132	3274
0.11%C	1020	3293
0.11% Mn + 0.032%S	659	1206
0.08% Cu + 0.0022% S	751	148
0.10% Cu + 0.028% P	1827	1744

1.3 Synthesis of the literature

- Although tinplate is commonly represented by a homogeneous stratigraphy, from the literature it is clear that this representation is not adequate for the prediction of its corrosion behaviour.
- In the first period of tinplate corrosion, the corrosion rate and the corrosion mechanism of tinplate approximate those of pure tin.
- In the absence of other oxidants, the ORR and the HER are the main cathodic reactions responsible for tin corrosion. However, the kinetics of the two reactions have never been studied independently of one another.
- Complexing anions such as citrate, oxalate, malate and tartrate are known to affect tin dissolution. However the relation between the complexing strength of anions and the corrosion rate of tin is still an important open point that should be clarified in terms of mechanisms and kinetics.
- The incomplete coverage of the $FeSn_2$ alloy demonstrates that the galvanic coupling between tin and the base steel is a common situation. In the literature, it is demonstrated that tin corrosion increases with its coupling with the base steel and that tin ions inhibit base steel corrosion. However, a rigorous description of these mechanisms is still lacking.
- A qualitative model describing the release of tin from tinplate is available in the literature. However a quantitative predictive model for tinplate corrosion has not yet been developed.

1.4 Objective

The objective of this PhD thesis is to identify and develop a quantitative long-term corrosion model able to predict the lifetime of tinplated plain cans as a function of the material structure and their content. The resulting model will constitute a new tool available for the conservators of historical can collections in defining an intervention timeline for existing or new collections. This main objective will be achieved through the following partial objectives:

- To develop methodologies to characterize the structure of plain tinplated steel in order to obtain the structural input parameters required for the model.
- To describe the corrosion mechanisms and electrochemical kinetics of tin in model electrolytes containing critical food molecular components in order to identify the food input parameters required for the model.
- To study the galvanic coupling between tin and iron in model electrolytes containing critical food molecular components in order to assess its influence on the mechanisms and kinetics of tin and iron corrosion.
- To verify in real food systems the consistency of the findings obtained in the model solutions and the evolution of the corrosivity over aging.

1.5 Strategy

The partial identified objectives will be accomplished by the following strategy:

- The thickness, chemical composition and morphology of each single layer comprise key information needed to make some predictions about the corrosion behaviour of tinplate. The complex multilayer structure of tinplated steel will be characterized through a multi-technique approach. The chemical composition of tinplates will be studied by means of AES, X-ray fluorescence (XRF) spectroscopy and chrono-potentiometry. The evaluation of the morphology of tinplate will be carried out by means of scanning electron microscopy (SEM), 3D white light interferometry (WLI) and chrono-amperometry.
- The mechanisms and kinetics of the electrochemical reactions responsible for tin corrosion will be studied in electrolytes mimicking the typical environment and chemistry of acidic canned fruits and vegetables. This study will be carried out through an electrochemical approach based on linear sweep voltammetry. The potentiodynamic polarization curves will be recorded to assess the overall electrochemical behaviour of tin, while the kinetics of the cathodic reactions responsible for tin corrosion at the corrosion potential will be investigated by means of the use of rotating disk electrodes.
- The effect of the galvanic coupling between tin and iron will be assessed through chrono-amperometry methods, measuring the direction and the amount of the coupling current circulating between the two metals. The implications of the coupling for the corrosion mechanism and kinetics of both tin and iron will be studied by means of potentiodynamic polarizations. Finally, X-ray photoemission spectroscopy will be used for the characterization of the surface chemistry after coupling.
- Real food systems subject to thermal accelerated aging and natural aging will be used as electrolytes for recording potentiodynamic polarizations on tin and for measuring the galvanic coupling current between tin and iron in order to evaluate the evolution of their corrosivity with aging and to validate the results obtained in model electrolytes.

2 Tinplate structure characterization

Goal

The aim of this section is to propose an accurate description of tinplate structure, in particular with regard to corrosion-relevant features, such as the local tin layer thickness and porosity. Thus, five different types of electrolytic tinplate material are fully characterized by means of a multi-technique approach. The tinplate stratigraphy was studied by means of the traditional chrono-potentiometric method to obtain general information over large areas, AES for a local assessment of the stratigraphy and XRF spectroscopy to assess the reliability of this non-destructive method. Chrono-amperometry, SEM and 3D WLI were carried out to assess to corrosion-relevant features, such as porosity, surface morphology and surface roughness.

2.1 Material and methods

2.1.1 Materials

The tinplate samples were provided by Stazione Sperimentale per l'Industria delle Conserve Alimentari (SSIC), Parma, Italy. The samples were coated with different nominal coating mass densities (**Table 9**). All the samples were produced by means of an electrolytic process followed by the conventional treatments of flow melting, passivation and oil spraying. Systematically, prior to each measurement, the oil layer was removed by sonication of the samples for 10 min in acetone (p.a. grade) and afterwards ethanol (p.a. grade). All characterizations were carried out on the side intended to be in contact with food (internal).

Table 9 Nominal tin mass density of the tinplate materials. [1] Category according to UNI EN 10202:2004. E denotes equal coating on each surface; D denotes differential coatings on each surface.

Sample	Nominal coating mass density [1)] [g/m^2]
A	E 1.4/1.4
B	E 2.8/2.8
C	D 5.6/2.8
D	D 8.4/2.8
E	D 11.2/2.8

2.1.2 Electrochemical measurements

Chrono-potentiometry was performed in line with the method proposed by Kunze et al. [20] and adopted for the ASTM A630-03 2014 standard [19]. Measurements were performed using a Metrohm Autolab PGSTAT30 potentiostat. The three electrode electrochemical cell includes a 0.78 cm^2 tinplate working electrode, a gold coil counter electrode (50 cm^2) and a reference saturated calomel electrode (SCE). A diagram of the experimental setup adopted is presented in **Figure 10**.

Chrono-potentiometric measurements were carried out through application to tinplate 9.7 mA/cm^2 in a 1 M solution of hydrochloric acid (250 cm^3) at room temperature. Before undertaking chrono-potentiometry, the passivation layer of tinplate specimens was removed by anodic cleaning in 0.5% w/w sodium carbonate by applying 77.5 mA/cm^2 for 15 s. The anodic cleaning was performed with the same electrochemical setup as used for the chrono-potentiometric stripping of tin.

Figure 10 Electrochemical setup used for chrono-potentiometry and chrono-amperometry.

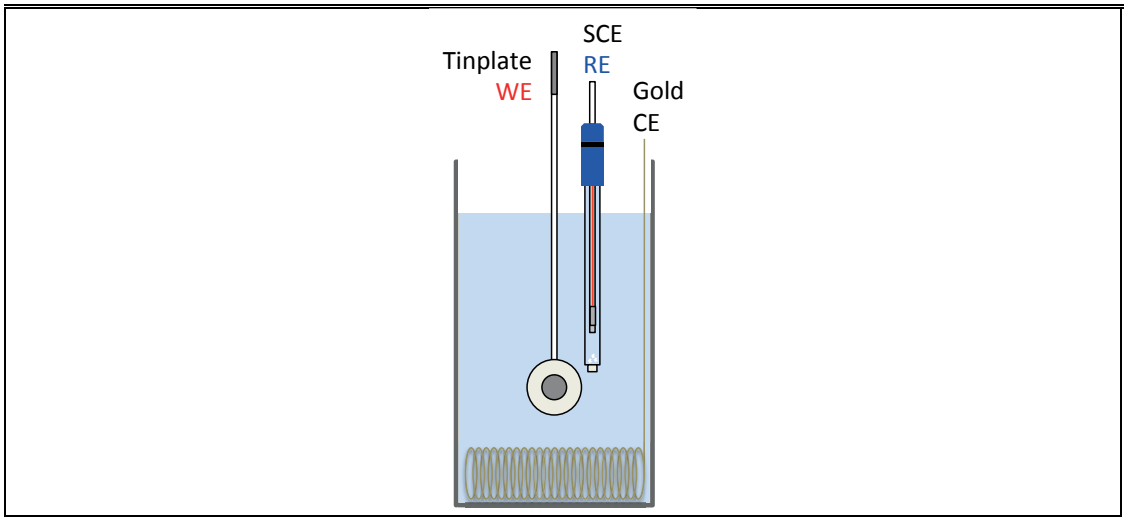

Chrono-amperometry was used to estimate the amount of base steel exposed through tinplate porosity. This IEV test was performed according to the method proposed by Tsurumaru et al. [21]. Measurements were performed using the same electrochemical setup adopted for chrono-potentiometry. The potentiodynamic polarization curves are shown in **Figure 11**.

Chrono-amperometric measurements were carried out by applying 1.3 V vs. SCE to the tinplate in a buffer solution at pH 10 (250 cm^3) comprising 0.02 M Na_2CO_3, 0.02 M of $NaHCO_3$ and 0.005 M NaCl. In these conditions, the measured current is mainly due to the exposed base steel as iron is transpassive and tin is passive (**Figure 11**). In the IEV method, the evolution of the current is measured over 180 s and the last recorded value corresponds to the IEV. The IEV is given in mA/dm^2.

Figure 11 Potentiodynamic polarization curves of tin and iron recorded in a buffer solution with a pH of 10 comprising 0.02 M Na2CO3, 0.02 M NaHCO3 and 0.005 M NaCl. For both electrodes, the potentiodynamic polarization showed a good reproducibility over four replications.

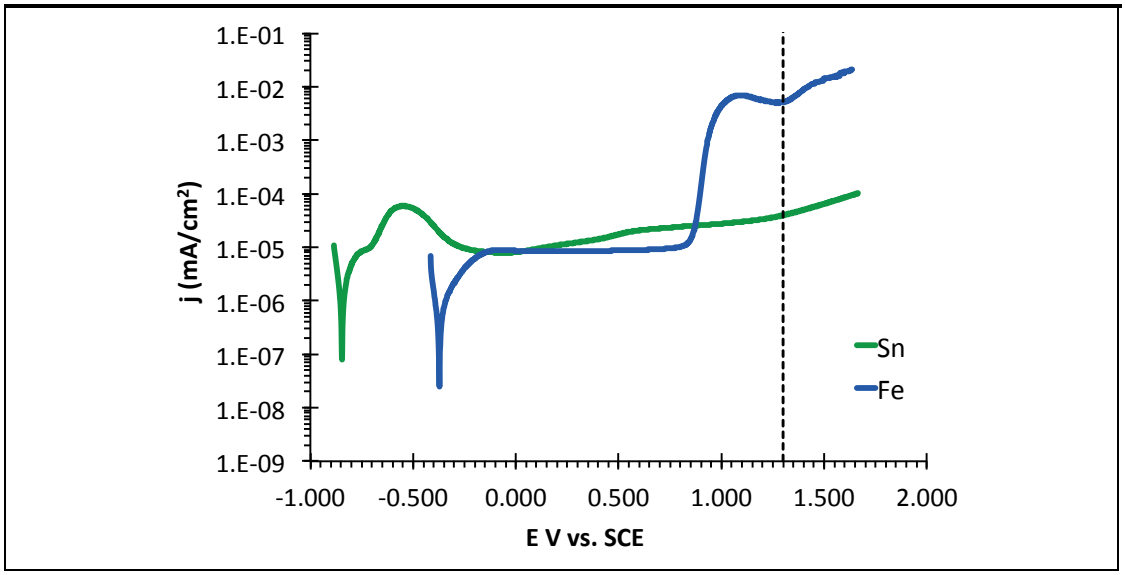

2.1.3 Surface analysis

AES was used for the chemical analysis of tinplate surfaces and to assess the in-depth variation of chemical composition. AES surface analyses were carried out using the Scanning Auger Microscope PHI680, with a primary electron beam of 10 nA at 10 keV. The cylindrical mirror analyser (CMA) resolution energy was 0.5%. AES depth profiles were measured using a 2 keV Ar+ ion beam (1 µA) over an area of

1x1 mm. Elemental maps were acquired using a matrix of 128x128 points. Peak amplitudes were determined as the difference between the element peak maximum from the direct spectrum and the background at the higher energy end of the peak.

AES depth profile analysis was carried at two different positions for each tinplate sample. The electron beam was scanned over an area of 20x20 µm. Signal intensities were converted into atomic concentrations using the sensitivity factors method with sensitivities of 1.7318 and 0.6633 for Sn and Fe respectively [74]. Sputter times were converted into depth using the sputter rate. This was determined by calibrating the AES depth profiling with a known thickness of the tin layer. The thickness of the tin layer was determined by taking the depth at which the tin concentration reached 50%.

The tin layer was produced by means of electrodeposition and the thickness assessed by means of WLI. The instrument used was a 3D White Light Interferometer Smart WLI GBS (10x objective). Tin deposition was realized on a copper disk electrode (Ø 5 mm). Prior to any tin deposition, the copper surface was polished with alumina suspension (1 µm). Plating was performed in 250 cm^3 of electrolyte containing H_2SO_4 at 1 M and $SnSO_4$ at 0.01 M [68]. Deposition was carried out using the same setup previously described for chrono-potentiometry; the only difference was the use of a copper disk electrode as the working electrode. Electroplating was carried out in a potentiostatic mode by applying -0.6 V vs. SCE for 3600 s. Prior to the deposition, the copper surface was activated in the plating solution through a short pre-treatment at -0.8 V vs. SCE for 5 s.

2.1.4 Optical and electron microscopy

Surface topography was studied with a 3D Smart WLI GBS (10x objective). The analysed area was 0.768x1.024 mm^2 with a vertical resolution better than 1 nm. Data treatment was performed using the MountainsView software. A Philips XLF30 microscope and a Zeiss Merlin microscope were used for SEM. Images were acquired with a secondary electron detector, applying an acceleration voltage of 10 keV and a working distance of 10 mm.

2.1.5 X-ray Fluorescence Spectroscopy (XRF)

The atomic percentage of tin present on the base steel was measured with a portable XRF analyser from Thermo Fisher Scientific, model Niton XL3t GOLDD+. Measurements were carried out on an analysis spot of 8 mm. All the measurements were done in "general metals" mode with a total analysis time of 180 s (45 s main range, 45 s low range and 90 s light range).

2.2 Results

2.2.1 Chrono-potentiometry

Figure 12 presents the chrono-potentiometric curves of the five types of samples. For all the samples, good reproducibility was observed over three replications. As expected from the literature [20] and the standard [19], three plateaux are clearly visible in the curves. The plateau located at the lowest potential corresponds to the dissolution of the free tin layer, while the plateau placed at the higher potential corresponds to the base steel dissolution. A third plateau located at potentials included between the dissolution potentials of tin and base steel identifies the $FeSn_2$ alloy dissolution. Sample D shows a narrow $FeSn_2$ plateau, most probably because the quantity of $FeSn_2$ is very low.

According to the standards, the quantities of free tin and alloyed tin in the form of $FeSn_2$ are identified through a graphical interpretation of the chrono-potentiometric curves. In this method, the transition from one plateau to another is identified by means of lines at a tangent to the chrono-potentiometric curves (**Figure 12e**). However, for very narrow plateaux, this method is not easily applied (Sample D).

Therefore a method based on the second derivative of the chrono-potentiometric curves was used here. In the second derivative of the potential versus time, the transition from the tin to the $FeSn_2$ phase was defined as the point at which the derivative changes its sign, i.e. when passing through zero and the first maximum. In the same way, the transition from the $FeSn_2$ phase to the iron substrate was taken as the point at which the derivative passes through zero after the second maximum. This method is illustrated for all the samples in **Figure 12**.

Figure 12e shows that the graphical method and the method based on the second derivative yield consistent results.

From the transition times, the film thicknesses corresponding to free tin and alloyed tin were calculated using **Eq. 3** (free tin) and **Eq. 4** (alloyed tin):

$$D_{Sn\ Free} = {t_{sn}\ j\ MM_{Sn}}/{n\ F\ \rho_{Sn}}\ 10^{-3} \quad (3)$$

$$D_{Sn\ Alloyed} = {0.65\ t_{FeSn_2}\ j\ MM_{Sn}}/{n\ F\ \rho_{Sn}}\ 10^{-3} \quad (4)$$

In these equations, *D* is the thickness (cm) of the layer (Sn free or Sn alloyed), *j* is the current density applied during the chrono-potentiometric experiment (9.7 mA/cm^2), *t* is the transition time, *MM* is the molecular mass (g/mol), ρ is the density (g/cm^3) of the tin (7.31 g/cm^3), *F* is the Faraday constant (96485 C/mol) and *n* is the valence of the iron and tin ions (2 equivalent/mole in both cases). The term 0.65 in **Eq. 4** accounts for the current effectively used for the dissolution of tin from the $FeSn_2$ phase [18-20]. The thicknesses evaluated with this method are reported in **Table 10.** The total tin coating mass density is calculated by multiplying the total thickness (free + alloyed tin) by the tin density. Samples A, B, C, D and E have a total tin coating mass density of 2.7, 2.5, 4.3, 7.3 and 9.5 g/m^2, respectively. These values are in good agreement with respect to the nominal coating mass densities reported in **Table 9** intended for the food side of tinplate.

Figure 12 Chrono-potentiometric curves measured on the five analysed tinplate materials (a), (b), (c), (d), and (e). For each chrono-potentiometric curve the second derivative is also reported as a function of time (black).

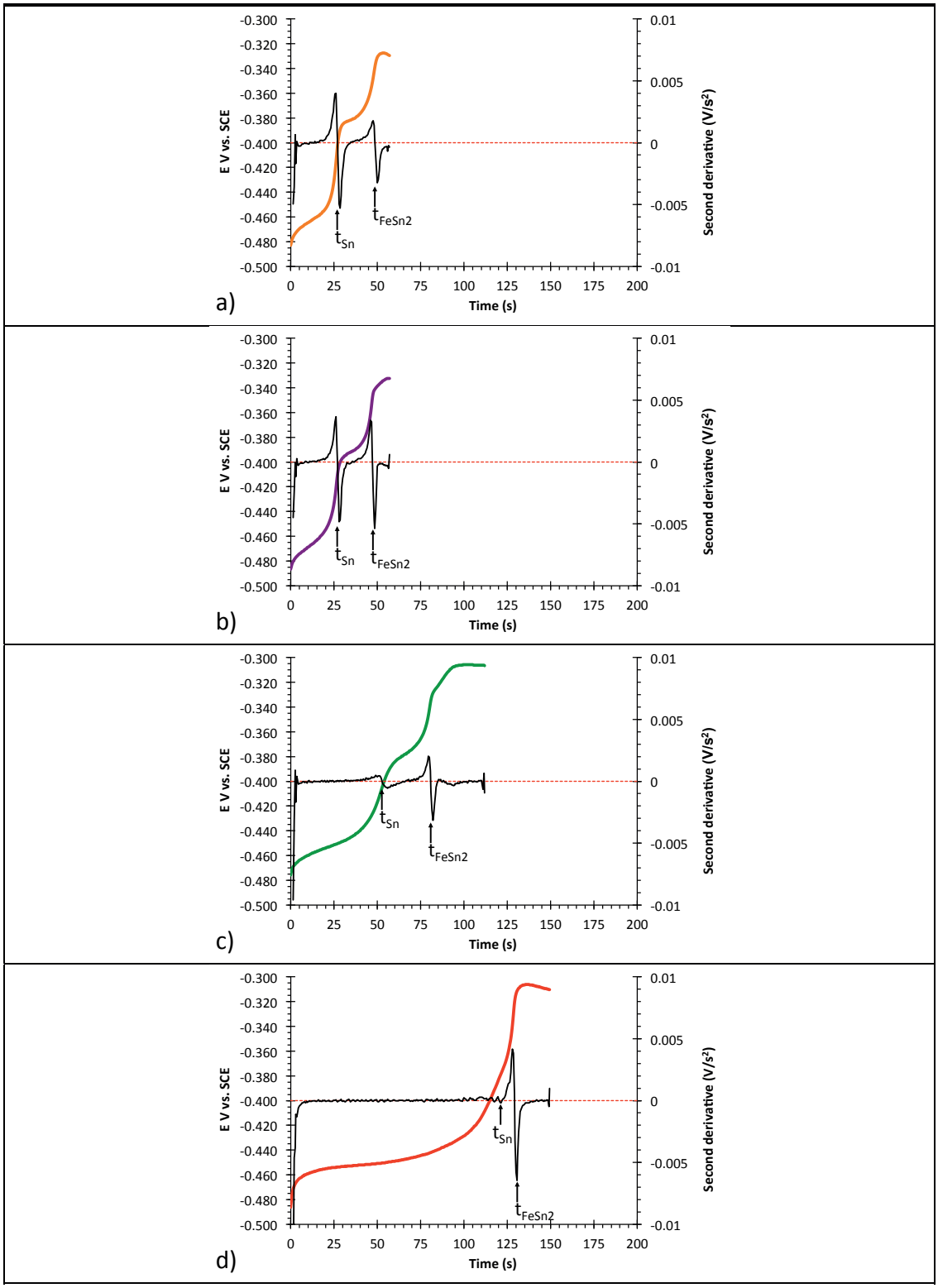

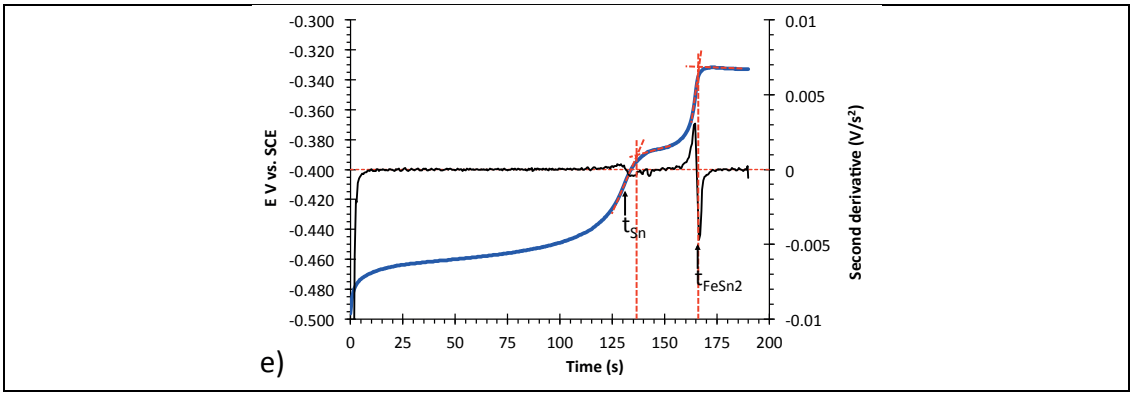

Table 10 Tin film thicknesses determined by means of chrono-potentiometry. *Mean values of three measurements.

Sample	Free Sn* (nm)	Alloyed Sn* (nm)	Total Sn
A	215 ± 05	124 ± 06	339 ± 08
B	211 ± 13	106 ± 05	317 ± 14
C	426 ± 06	138 ± 14	564 ± 15
D	936 ± 49	49 ± 09	985 ± 50
E	1061 ± 65	193 ± 08	1254 ± 66

2.2.2 Chrono-amperometry

Table 11 shows the IEV for the five types of tinplates for 99.99% pure tin and Armco iron. For all the samples good reproducibility was observed over five replications. Considering the masses of tin coating reported in **Table 10**, the IEV values decrease with an increase in the mass of tin coating. The similarity clearly observed among samples A and B based on chrono-potentiometry is also confirmed in terms of porosity when using chrono-amperometry.

Table 11 Iron exposure values. *Mean values over five measurements.

Sample	IEV* (mA/dm^2)
Armco Fe	493.50 ± 49.51
A	205.03 ± 8.90
B	202.95 ± 7.13
C	31.17 ± 2.78
D	16.99 ± 1.66
E	8.80 ± 2.10
Pure Sn	1.83 ± 0.16

2.2.3 AES sputter rate calibration

SEM imaging of the electrodeposited tin layer is shown in **Figure 13a.** The coating appears very uniform and homogeneous. The average thickness measured over 10 points by means of 3D WLI was 737 ± 54 nm. The efficiency of the electrodeposition was found to be 70%. AES depth profiles were recorded for the three areas shown in **Figure 13a**. The excellent reproducibility of the three AES concentration profiles reported in **Figure 13b** is a further confirmation of the quality of the tin deposition. Intensity signals were converted into atomic concentration using the sensitivity factors method with sensitivities of 1.7318 and 0.6633 for Sn and Cu respectively [74].

The AES profiles do not show a sharp tin–copper transition. Sputtering induced effects such as the intermixing effect. The differential sputtering determines the broadening of the tin–copper transition. The width of the interface is quantified by the time needed to move from 84% to 16% of the initial signal of tin [75]. A sputter rate of 36 nm/min was obtained for tin by dividing the tin layer thickness (737±54 nm) by the time needed to reach 50% of the initial signal (20.33±0.06 min). It should be pointed out that the nano-porosities and roughness of the electrodeposited tin layer can increase the apparent thickness and thus lead to an overestimation of the nominal sputter rates and film thicknesses determined by AES. The decision not to perform the flow melting of the deposited tin layer is due to the fact that tin and copper may react, forming bronze. The ratio of the atomic concentration of tin and copper between time zero and the time needed to reach 50% of the initial signal indicates that porosity may contribute to an overestimation of the sputter rate by 10%.

Figure 13 AES sputter rate calibration: SEM image of the surface of a) the electrodeposited tin layer and b) the atomic concentration depth profiles of tin and copper.

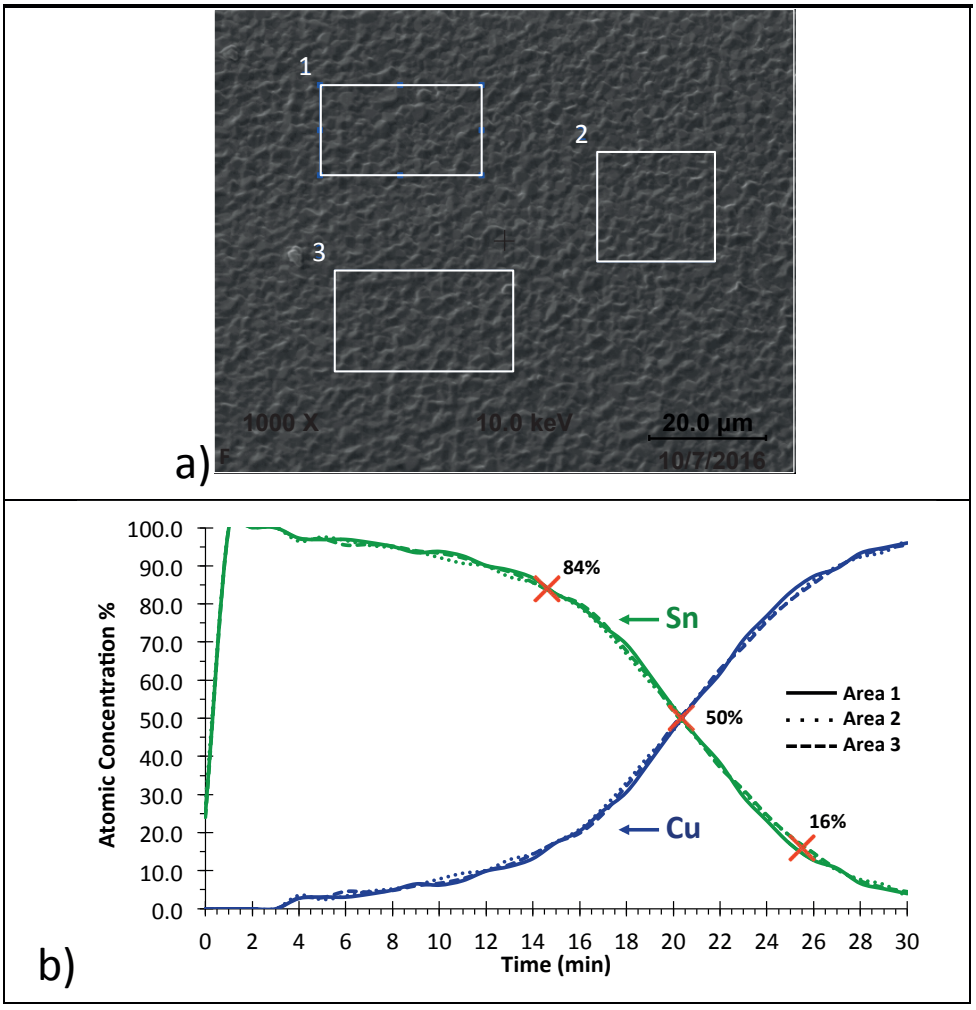

2.2.4 AES surface analysis

The typical surface distribution of elements was assessed using Sample E by means of AES mapping. Maps of tin, iron, carbon, oxygen and chromium were acquired over an area of 1716 μm^2. Sample E was chosen because it had a higher thickness of tin layer and this allowed good characterization of the tin layer.

Chromium and oxygen chemical maps showed that the two elements were uniformly distributed over the surface (**Figure 14**). This was consistent with the chemical composition of the chromium oxide passivation layer formed on the top of tinplate. Tin but not iron is detected in small areas in which chromium is not present. The shape and the lack of an iron signal suggest that superficial scratches in the passivation layer originate these areas. The tin in the oxide layer is exposed through the scratches of the passivation layer. Carbon is homogeneously detected over the surface as a typical atmospheric contaminant.

Afterwards, 36 nm of material was removed by 1 min of sputtering. AES chemical mapping was recorded on the new surface and is shown in **Figure 14**. The disappearance of chromium and oxygen signals after 1 min of sputtering shows that the chromium oxide passivation layer has a thickness < 40 nm. Tin is now the principal element present over the surface. An area rich in iron and poor in tin is clearly visible. Carbon is also present in this area, while it is completely absent from the rest of the surface. The presence of iron and carbon suggests that this area corresponds to an early exposure of the base steel, while the co-presence of iron and tin can be attributed to the $FeSn_2$ alloy.

Figure 14 AES mapping of the elements on the surface of sample E. Elements on the virgin surface: a) Sn, b) Fe, c) O, d) C and e) Cr and at 36 nm depth; e) Sn, f) Fe, g) O, h) C and j) Cr.

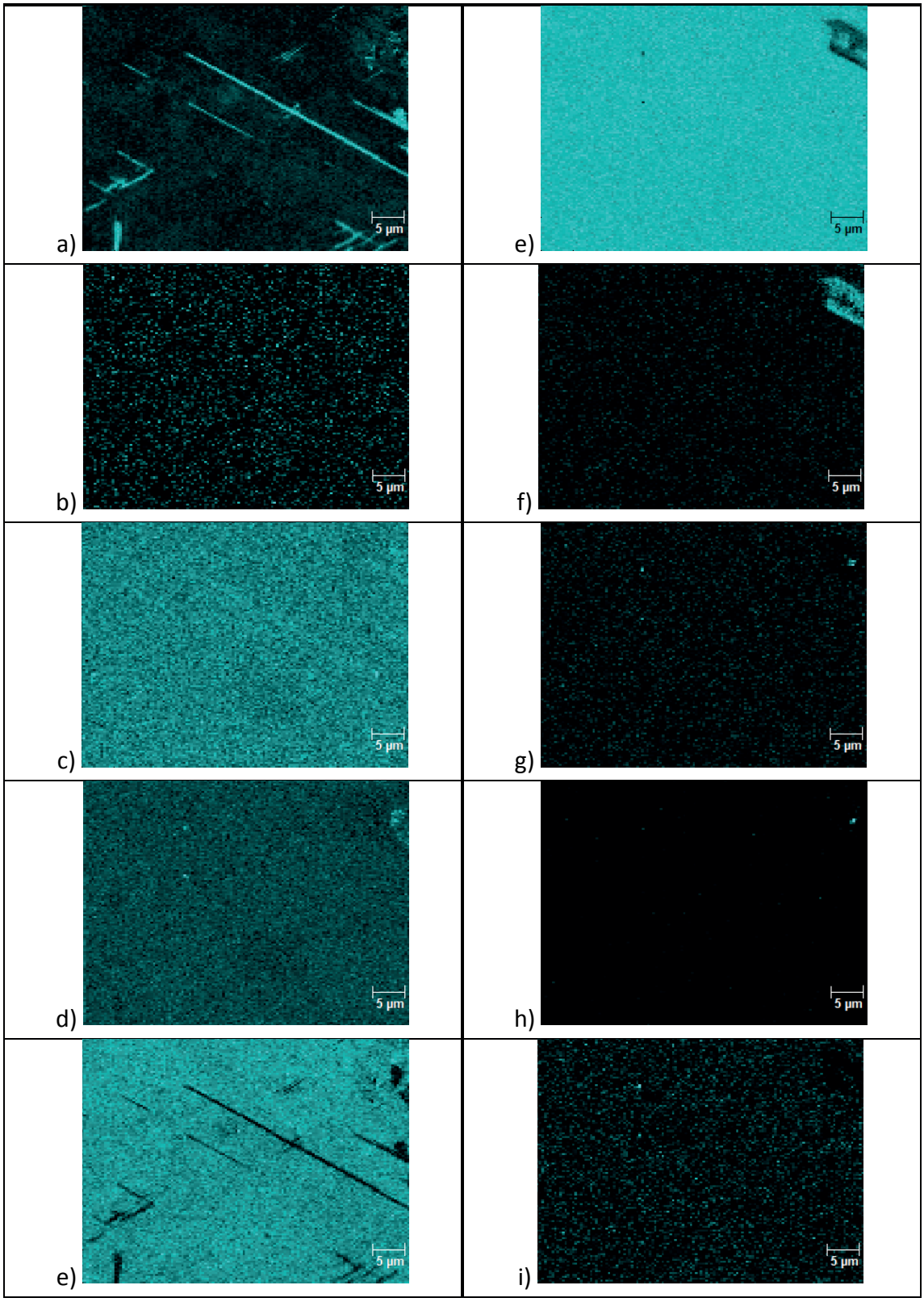

AES mapping was performed at 252 nm, 432 nm, 792 nm, 1152 nm and 1620 nm sputtering depths. The most relevant tin and iron chemical maps are shown in **Figure 15** as contrast images by means of RGB overlay. AES maps do not show a sharp tin–iron transition, but a smooth continuous transition. The morphology of the surface is shown in **Figure 16** by means of SEM images acquired at the end of each sputtering cycle.

The three components of tinplate – tin, $FeSn_2$ alloy and base steel – are clearly recognizable by comparing the SEM images of the surfaces (**Figure 16**) with their AES chemical maps (**Figure 15**). In **Figure 16** the initial smooth phase corresponds to the homogeneous tin layer, while the dark areas comprise the base steel. Interestingly, from the beginning areas of the base steel emerge from the thick tin layer of sample E. The $FnSn_2$ alloy phase, identified in the AES chemical maps as regions of the co-presence of tin and iron, located at the edges of the base steel areas, is characterized by a very rough appearance.

Figure 15 Sn (green) and Fe (blue) AES maps of sample E at different depths: a) 36 nm, b) 252 nm, c) 432 nm, d) 792 nm, e) 1152 nm and f) 1620 nm.

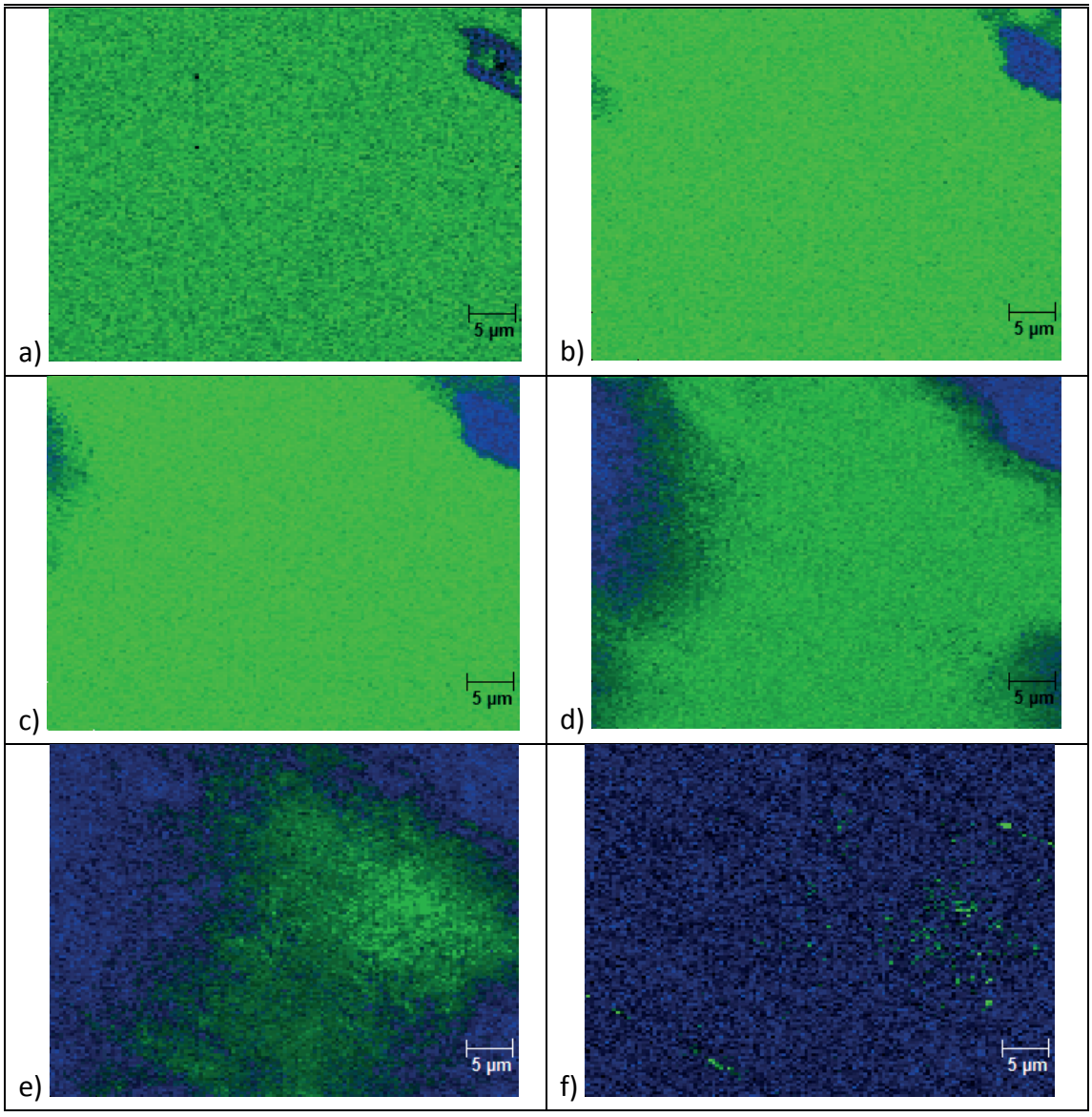

Figure 16 SEM images of sample E at different depths: a) 36 nm, b) 252 nm, c) 432 nm, d) 792 nm, e) 1152 nm and f) 1620 nm f).

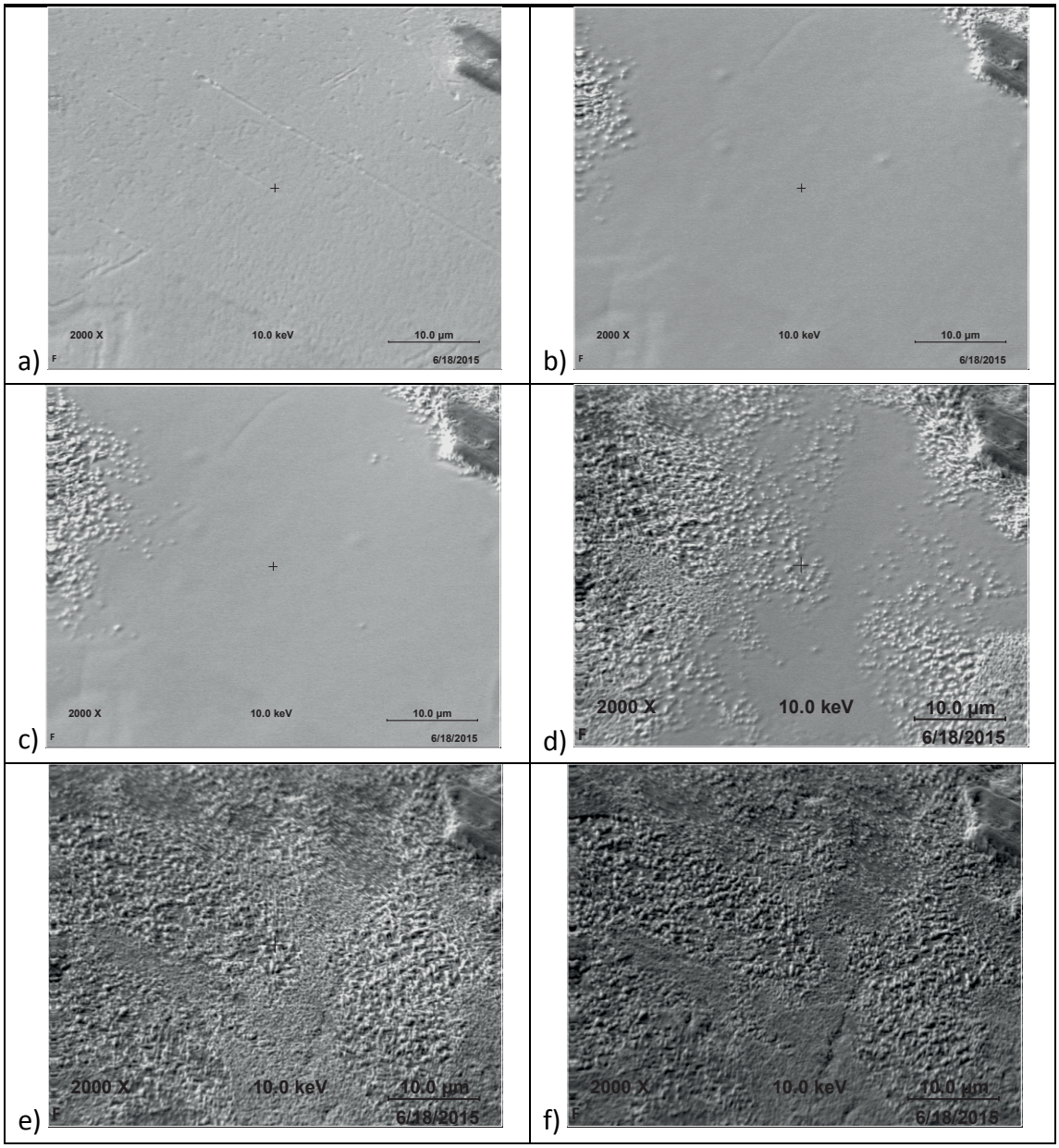

2.2.5 AES depth profiling

AES depth profiles of tin and iron atomic concentrations together with the SEM images of the virgin surface showing the analysed spots are reported in **Figures 17–21.** Samples coated with a high quantity of tin (C, D and E) have concentration profiles characterized by an initial plateau in which the tin concentration is constant and an iron signal is not detected. Afterwards, the tin concentration gradually decreases until the appearance of the iron is a detected element. This broad transition region has two shoulders located at 85–95% Sn and 20% Sn. These

shoulders are probably related to the discontinuity of the transition from tin to iron (base steel) introduced by the simultaneous presence of the $FeSn_2$ alloy. The tin plateau is not visible in samples A and B, whereas iron is already detected on the surface. This behaviour is due to the non-uniform coverage of the base steel when low mass densities of tin are used for tinplate production. For each sample, the thicknesses of the tin layers vary from one spot to another. This phenomenon is particularly evident in tinplate E. In this sample, AES depth profiles were also recorded at points (35 nm).

Figure 17 AES depth profile analysis of sample A: SEM image of the surface showing a) the analysed areas and b) the atomic concentration depth profiles of tin and iron.

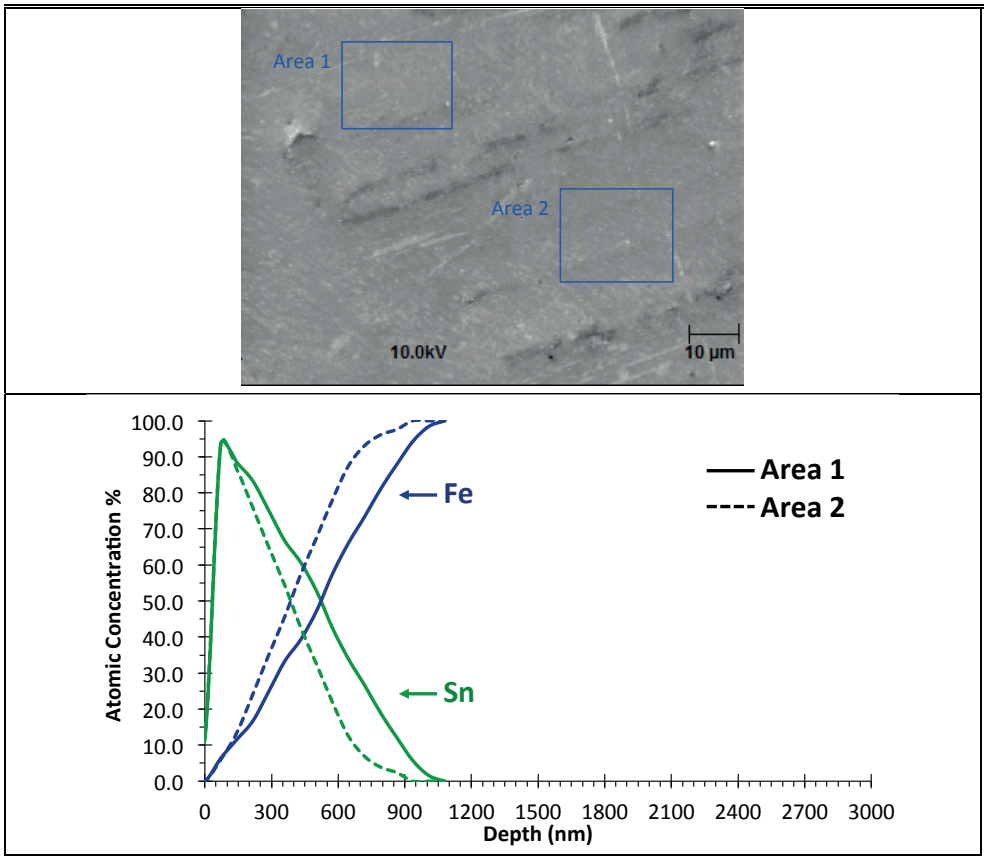

Figure 18 AES depth profile analysis of sample B:

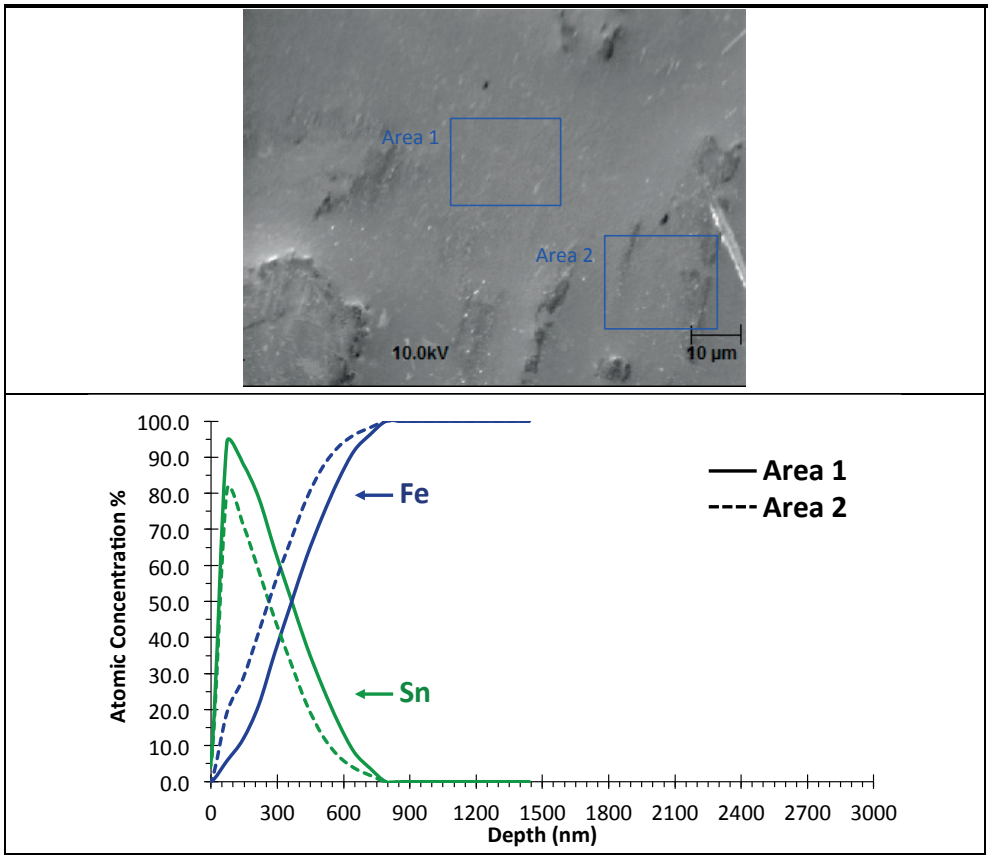

Figure 19 AES depth profile analysis of sample C

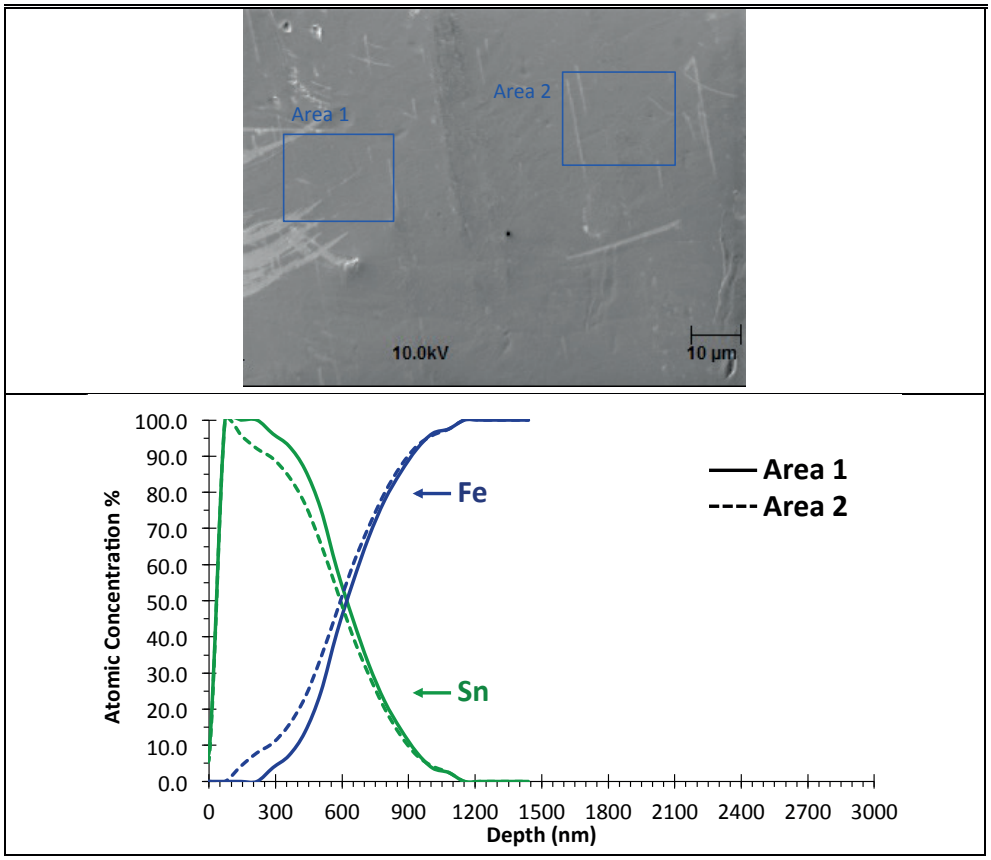

Figure 20 AES depth profile analysis of sample D

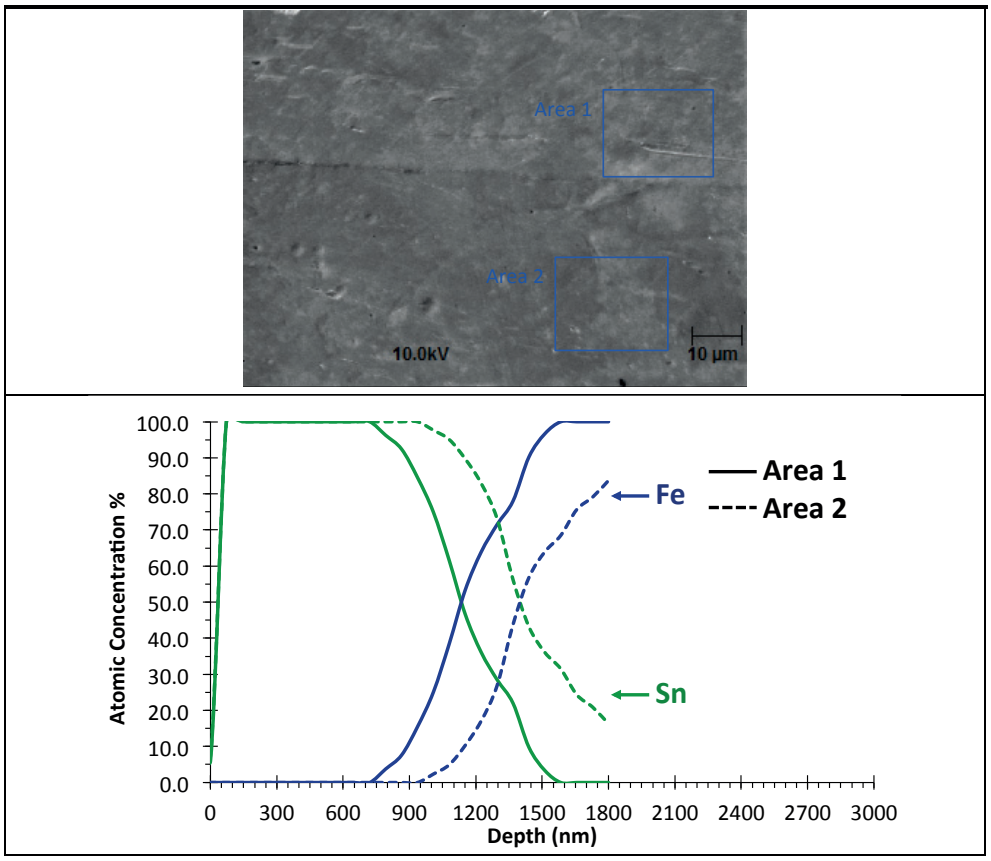

Figure 21 AES depth profile analysis of sample E

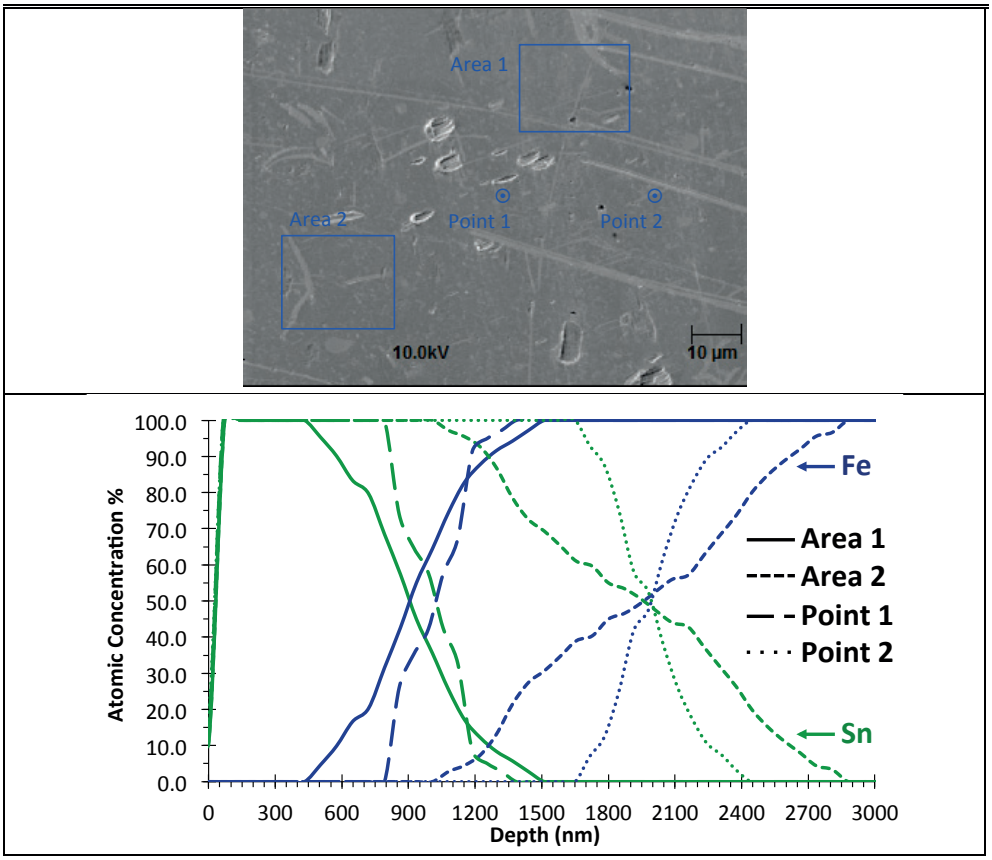

2.2.6 XRF analysis

Table 12 reports the atomic percentages of tin determined for each sample using XRF. This technique does not allow discrimination between the tin signals from either free tin or the $FeSn_2$ alloy. However XRF does permit determination in a rapid and non-destructive manner of the average amount of tin present over a large area.

Table 12 X-ray fluorescence analysis.

Sample	Sn %
A	0.86
B	0.68
C	1.53
D	2.58
E	3.42

2.2.7 Surface topography

Figure 22 shows the 3D surface profiles of the five tinplate samples. In the left column samples are shown in their pristine state, while in the right column samples are shown after sputtering for AES depth profiling.

In this way, it is possible to assess, respectively, the morphology of the tin coating and the morphology of the base steel after the coating removal by means of ion etching. In the pristine state, the surfaces of tinplate samples coated with a larger mass of tin are much smoother. This is because during the flow-melting step the tin melts and fills the valleys between the base steel striae.

After removal of the tin layer, the striae of the base steel are clearly visible for all the samples. The striae are formed during the manufacture of the base steel. The roughness values Ra (mean deviation from central line average) were determined based on five cross-sectional lines extracted for the 3D profiles perpendicular to the striae observed in **Figure 22** (cut-off length 0.25 mm). The increase in roughness after the removal of tin by means of ion etching (**Figure 23**) could be due to the removal of a tin layer of non-uniform thickness and/or to sputter-induced roughening [75].

Figure 22 3D surface profiles measured before (left column) and after (right column) AES sputtering for sample (a), b), c), (d) and (e).

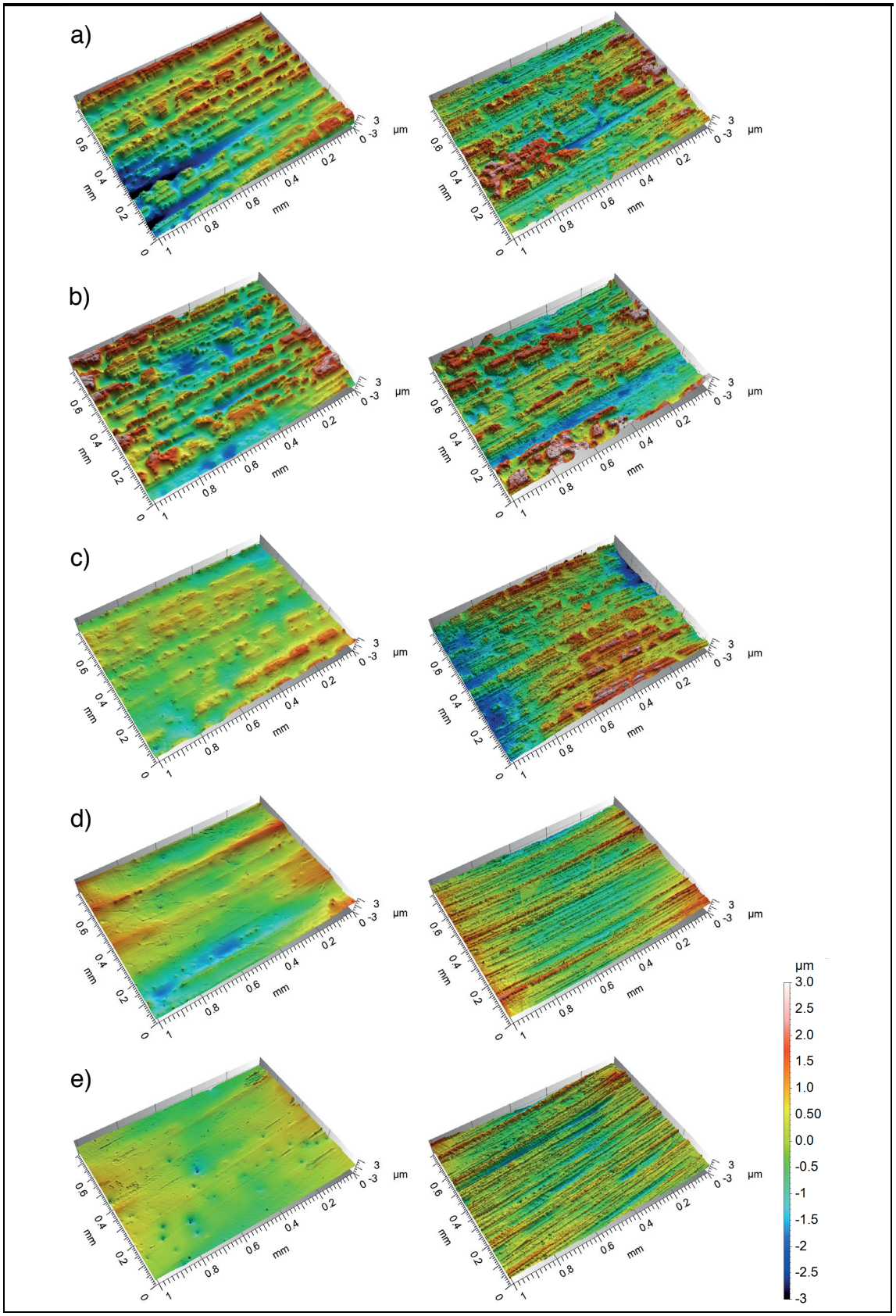

Figure 23 Ra values measured over 5 profile lines perpendicular to the striae visible in **Figure 22** for the five different tinplate samples.

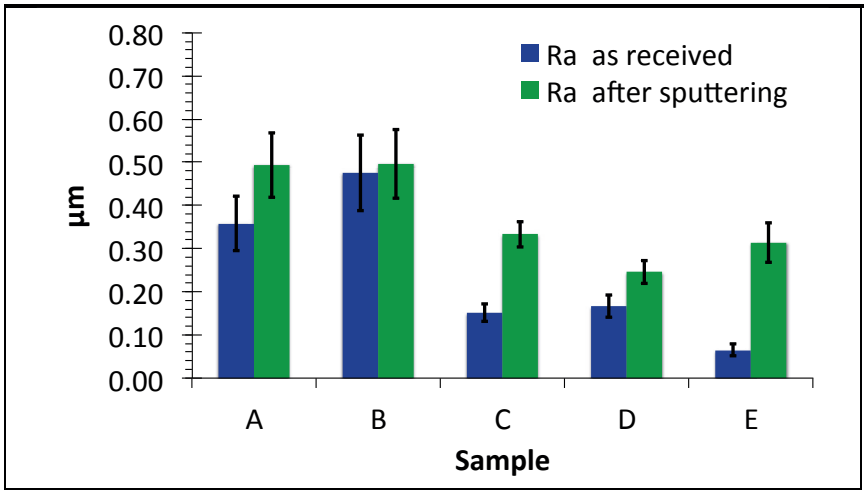

2.2.8 Surface morphology of the tin layer

SEM analysis was carried out on all tinplate samples in the pristine state and after the removal of the tin layer by means of chrono-potentiometric stripping. In this way it was also possible to characterize the topography of the tin layer and the $FeSn_2$ alloy.

The well-oriented striae, previously observed by means of 3D WLI, are visible in **Figure 24** on the pristine surfaces of samples A, B and C. At higher magnifications, the typical acicular structure of the $FeSn_2$ alloy [27-31] is clearly visible on the striae. This is due to the very low thickness of the tin layer left on the striae after the flow-melting process. The tin layer covering the striae is also porous and not homogeneous (**Figure 24**). Samples D and E reveal rather homogeneous surfaces and the striae are not visible. Isolated porosities and superficial scratches are the principal detectable defects (**Figure 24**).

Figure 24 SEM images taken on all the tinplate samples in the pristine state. For each sample, two magnifications are reported: 1000x and 5000x.

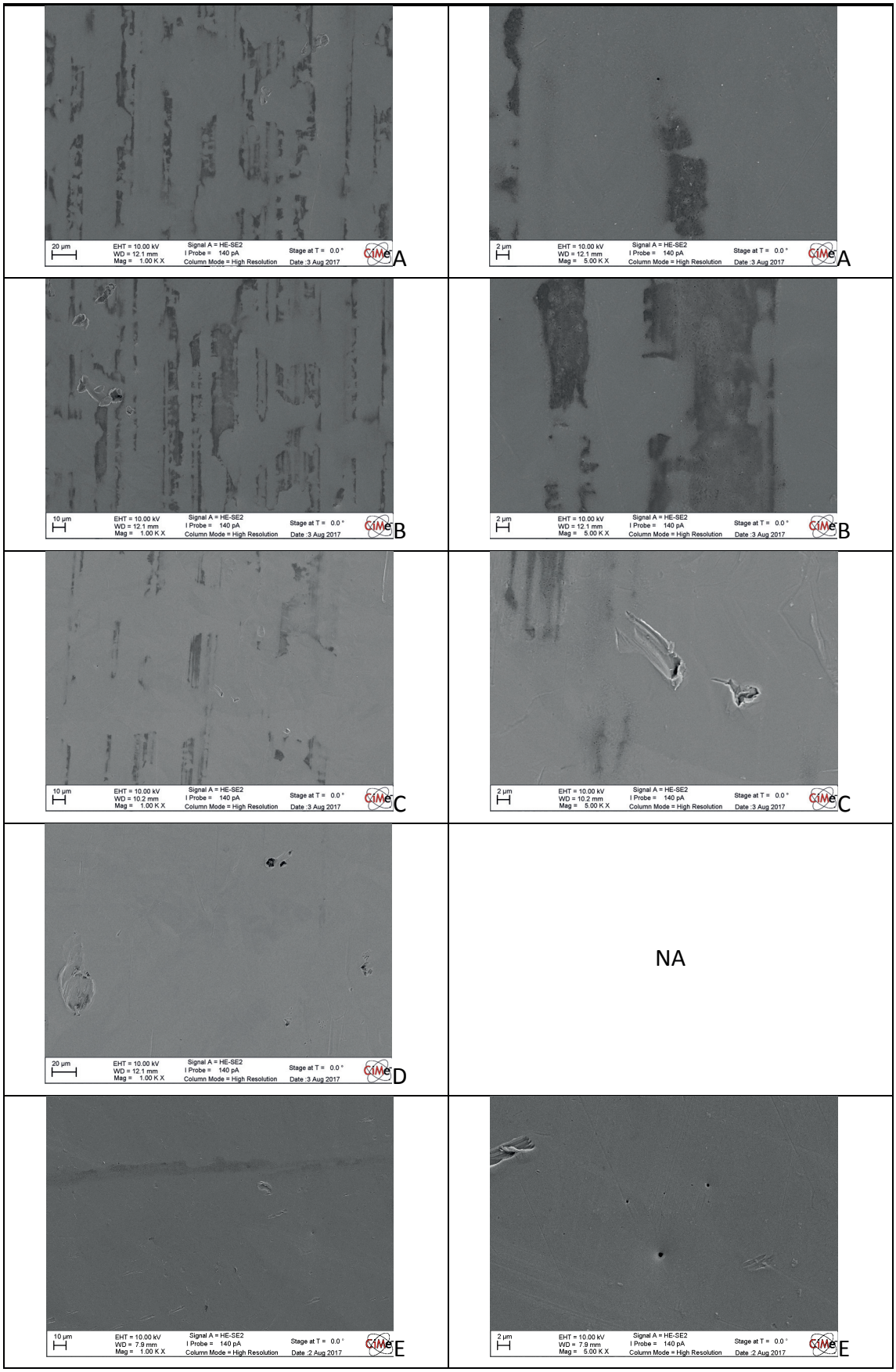

2.2.9 Surface morphology of the interface

The surface topography after the chrono-potentiometric stripping of the tin layer until the $FeSn_2$ alloy plateau was reached (**Figure 25**) is shown in **Figure 26**. Three phases are simultaneously present on the surfaces: residue of the tin layer, the $FeSn_2$ alloy acicular structure and base steel exposed through the $FeSn_2$ alloy porosities or at the sites of localized attack. The SEM image of sample D after the removal of tin (**Figure 25**) reveal the lack of homogeneity and the laches of coverage of the $FeSn_2$ alloy. This is in agreement with what was expected from the chrono-potentiometric stripping curve (**Figure 11**).

During chrono-potentiometric stripping, samples undergo a continuous transformation and thus small differences at the end time determine the variety of the surface states as shown in **Figure 25.**

Figure 25 Chrono-potentiometric curves measured on tinplate samples A to E showing the stripping of tin until the FeSn2 plateau.

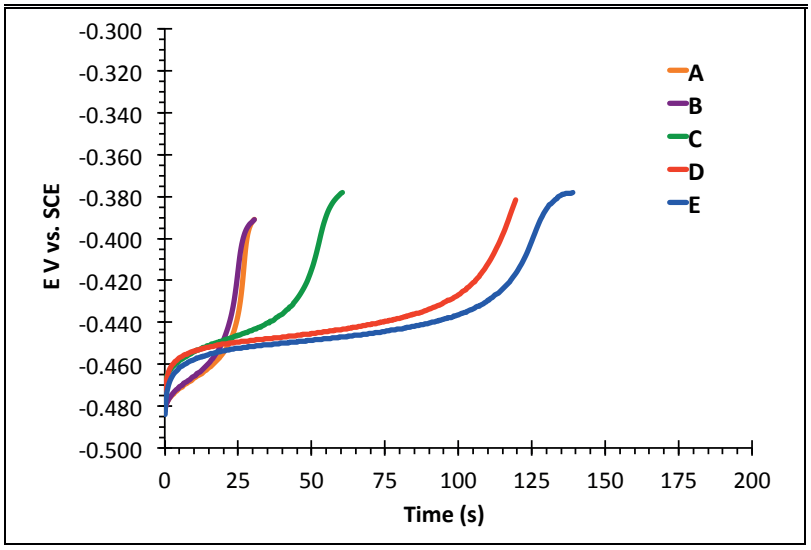

Figure 26 SEM images taken for all the tinplate samples after chrono-potentiometric stripping of tin. For each sample, two magnifications are reported: 1000x and 5000x.

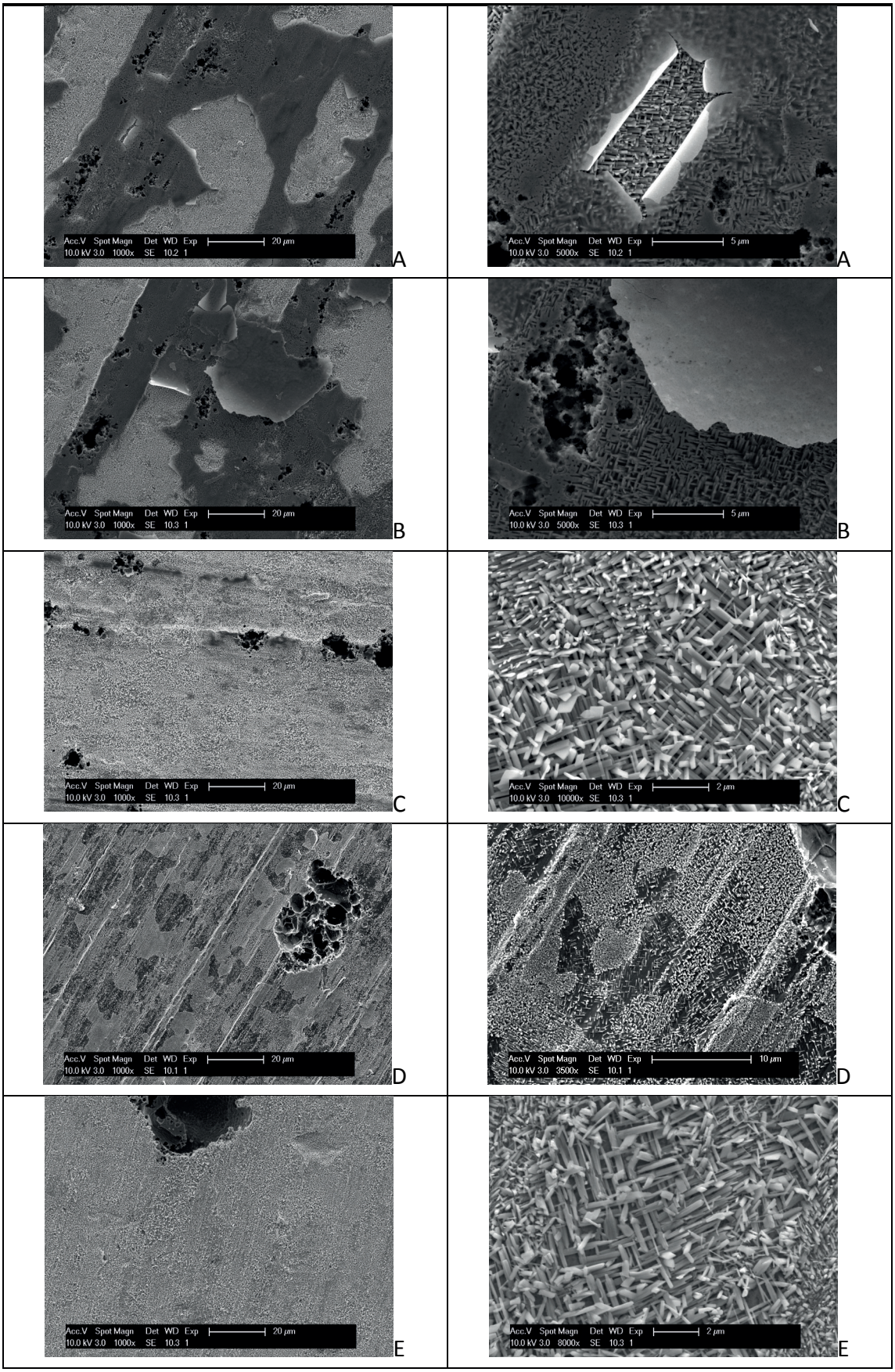

For Sample E the chrono-potentiometric stripping was stopped after 70 s. According to **Figure 11e**, at this time the surface is still coated with an homogeneous pure layer of tin. However, the SEM images presented in **Figure 27** show that only a fraction of the surface is still coated with tin. The rest of the surface shows large areas covered by the easily recognizable $FeSn_2$ alloy. At this early stage, local attacks on the base steel are also visible **(Figure 27c)**.

Figure 27 SEM images taken of the tinplate Sample E after 70 s of chrono-potentiometric stripping of tin. a) Overview of the surface showing the co-presence of Sn and $FeSn_2$ alloy and localized attacks on the base steel. b) Magnification of the acicular structure of the $FeSn_2$ alloy emerging from de-residual tin. c) Magnification of localized attack of the steel.

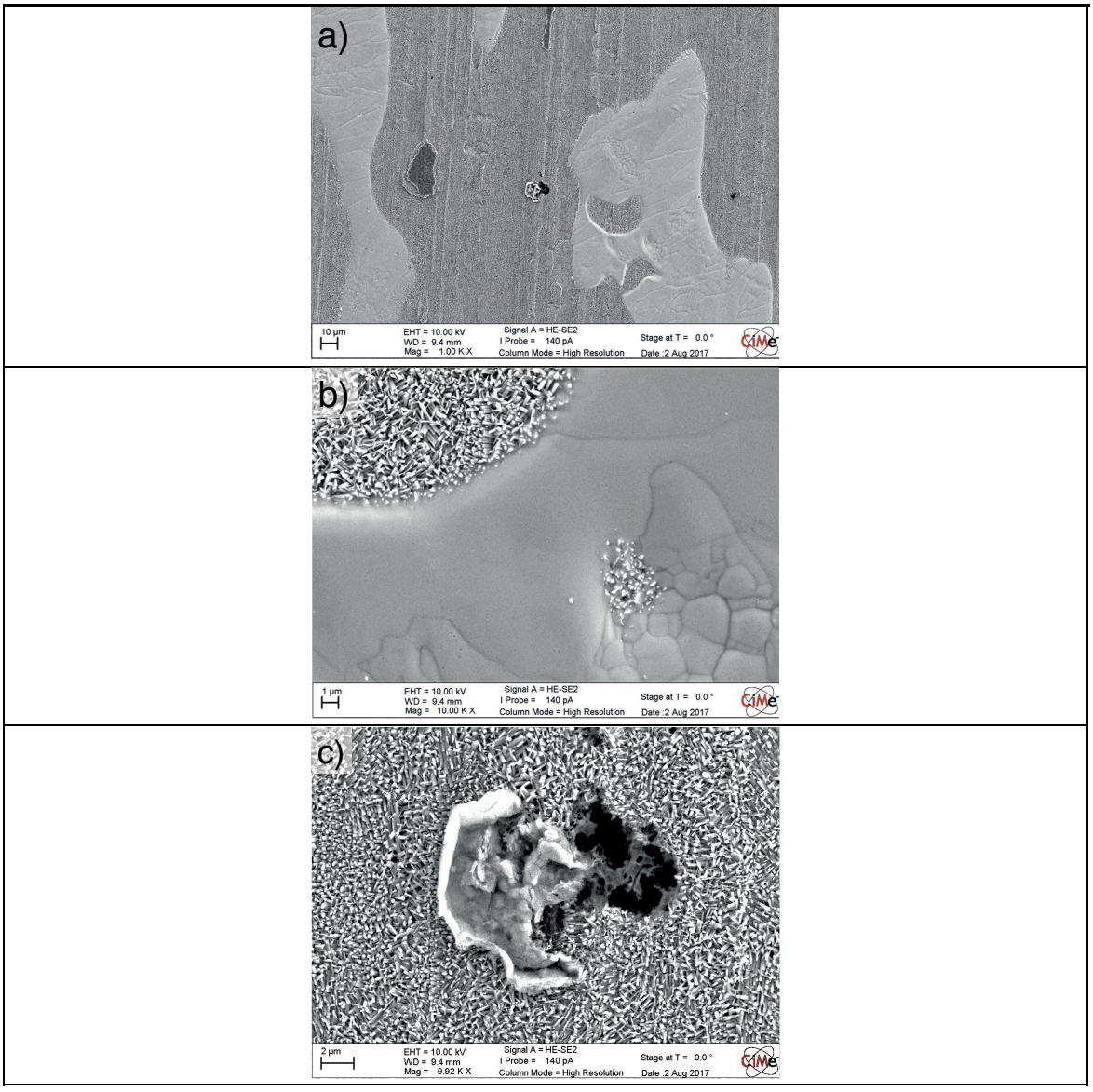

2.3 Discussion

2.3.1 Correlation between the different techniques used

The chrono-potentiometric stripping method and XRF are both quantitative methods for determining the average amount of tin deposited over a large area. Chrono-potentiometry and XRF were carried out over areas of 0.78 cm^2 and 0.5 cm^2, respectively. **Figure 28** shows the good linear correlation among the atomic percentages of tin assessed by means of XRF and the total tin thickness (free tin and alloyed tin) determined by chrono-potentiometry. Thanks to this, it is possible to convert the XRF results into a total thickness of tin. XRF analysis is a non-destructive method, which is faster and requires a simpler experimental setup than chrono-potentiometry. However, XRF analysis is unable to distinguish between free and alloyed tin.

Figure 28 Correlation between film thicknesses measured by the chrono-potentiometric method and the atomic concentrations of tin detected by means of XRF spectroscopy. Regression was forced to pass from zero.

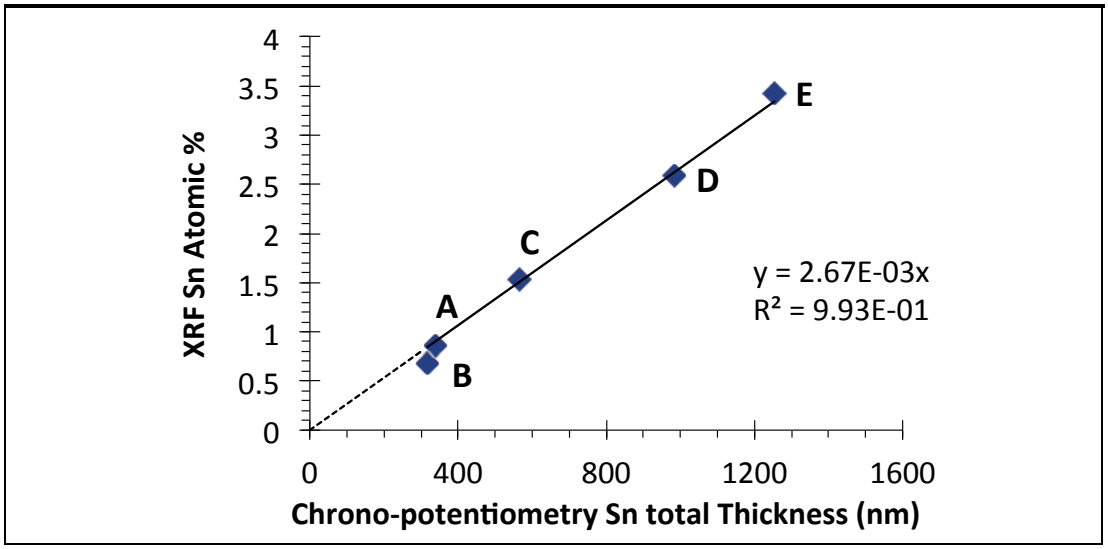

Figure 29 shows the relation between the values of the total tin thickness determined by means of chrono-potentiometry and those obtained through AES depth profiling. A good linear correlation was also found in this case. However, with respect to the chrono-potentiometry, AES overestimates the total thickness of tin by 12%. This, as already shown in section 2.2.3, is consistent with the 10%

overestimation of the sputtering rate due to the porosity of the reference sample used for the calibration.

Figure 29 Correlation between film thicknesses measured by AES depth profiling and the chrono-potentiometric method. Regression was forced to pass from zero.

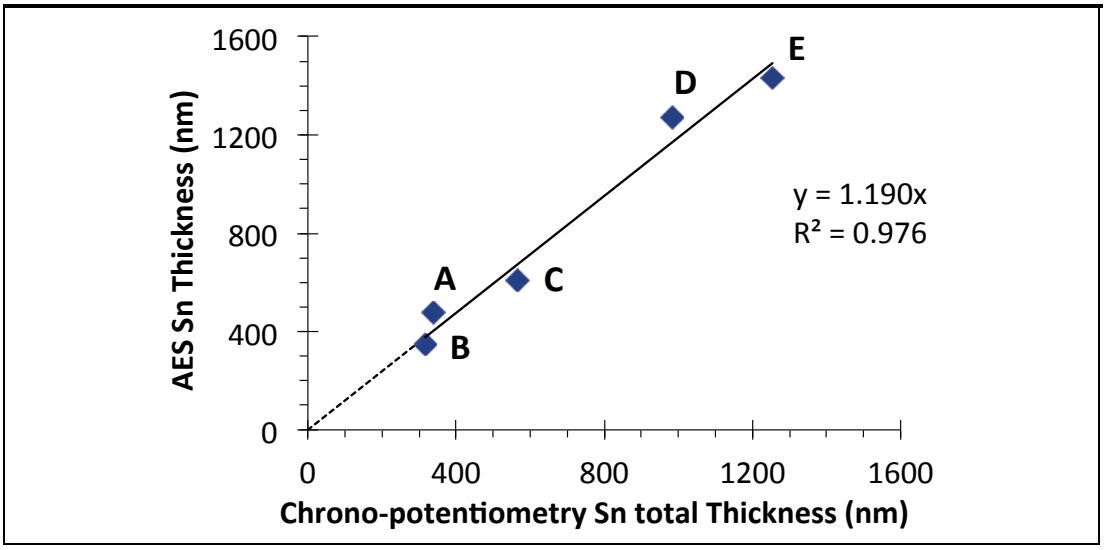

Although the shoulders observed in the AES depth profiles (**Figures 17–21**) suggest that this technique is sensitive to the presence of the $FeSn_2$ alloy, in contrast to chrono-potentiometry AES depth profiling cannot quantify the amount of tin present in this form. In all the AES depth profiles (**Figures 17–21**), the five tinplate samples have wide interfaces. Several phenomena affect the tin-iron transition and cause a broadening of this interface.

First of all, iron is present in all AES profiles at depths much l than the film thickness as determined by the 50% atomic concentration of tin. This may be due to local variations of film thickness and the statistical nature of ion etching resulting in local different sputter rates (for example between surface asperities and valleys). Furthermore, the interface is most likely characterized by the interdiffusion of tin and iron responsible for the formation of the $FeSn_2$ alloy. Thus, the inter-needle voids of the $FeSn_2$ acicular structure are filled with a tin-iron metal matrix characterized by a diffusion gradient of tin in the depth axis. These factors (diffusion gradient, profile distortion by statistical sputtering, $FeSn_2$ needle-like phase) all contribute to a difficult quantitative interpretation of the interface area according to the AES depth profiles and thus the quantification of the intermetallic $FeSn_2$ alloy.

Since it can be carried out over specific points, AES depth-profiling analysis is the sole technique that allows measurement of the variability of the tin coating thickness. In contrast, the chrono-potentiometric stripping method and XRF analysis yield average values of the tin thickness over a large surface. For example, **Figure 21** shows a variation of the tin film thickness up to 50% for AES profiles measured over four points within a 60 µm radius. AES also reveals that iron is exposed at the surface at depths much lower than the nominal free tin layer thickness determined by coulometry. The thinning of the tin coating at the top of the base steel striae and asperities is clearly shown in the SEM analysis carried out on the tinplate samples A, B and C in the pristine state (**Figure 24a, b, c**). In samples A and B, the high porosity and inhomogeneity of the tin layer left over the striae support the IEV results that indicate an exposure of iron of 40% (**Table 11**). Since the corrosion resistance of tinplate depends on the thickness and integrity of the tin layer, these defects clearly affect the corrosion resistance of the tinplate and therefore the chrono-potentiometric results concerning film thicknesses should be considered with caution.

2.3.2 Accurate tinplate structure representation and corrosion implications

The multi-technique characterization approach carried out on five tinplate samples showed the inaccuracy of the material structure reported in the literature (**Figure 2**). **Figure 30** sketches a more realistic and accurate representation of the tinplate stratigraphy, which is based on the findings of these studies. It consists of the thin chromium passivation layer, a pure tin layer of variable thickness due to the base steel roughness and characterized defects, such as scratches and pores, an interfacial layer containing $FeSn_2$ needles embedded in a matrix composed of a mixture of tin and iron and finally the base steel.

Figure 30 Realistic representation of the tinplate structure.

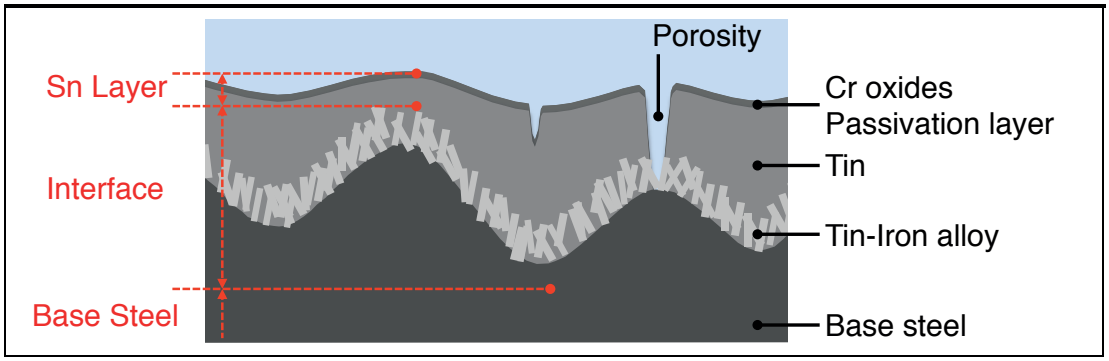

Figure 30 shows the corrosion-relevant features that have to be considered in predicting the corrosion mechanisms of tinplate and the estimation of its lifetime, namely:

- Base steel roughness, which in combination with the flow-melting process introduces local variation in the tin layer. The weak points controlling the lifetime of tinplate are the base steel striae and all the other areas coated with the thinnest tin layer.
- Porosity of the tin coating. Pores can be divided in two categories based on their depth: first, pores with a depth greater than the thickness of the tin layer. These pores are particularly critical because they will cause the exposure of the interface and/or the base steel to the corrosive environment. Second, there are pores within the tin layer, which are less critical for corrosion because their contribution simply entails a local reduction of thickness of the tin layer and not direct exposure of the underlying layers.
- Scratches, like pores, can be superficial, limited to the chromium oxide passivation layer and the tin, or deeper and expose the base steel. This second type of scratch will dramatically compromise the corrosion resistance of tinplates.
- Interface structure. The interface between the tin layer and the base steel is characterized by the coexistence of tin, base steel and the intermetallic alloy ($FeSn_2$ alloy). This alloy is chemically inert [10]; however, due to its acicular structure, it cannot completely shield the base steel. Spaces between the needles of the $FeSn_2$ alloy expose the base steel. The degree of $FeSn_2$ alloy coverage is a key parameter, which depends on the quality of the flow-melting

treatment during tinplate production [13,14,27]. Coupling between tin, iron and the $FeSn_2$ alloy can furthermore complicate the corrosion behaviour of the interface.

2.3.3 Assessment of the characterization methods

The chrono-potentiometric method [18-20], provides access in a fast and reliable way to the average thickness of the Sn layer, but does not consider porosity or variable tin thickness. The traditional interpretation of chrono-potentiometric tests considers the interface as composed only by the $FeSn_2$ alloy and does not address the coexistence of iron and tin. Moreover, this technique cannot provide information on the coverage of the $FeSn_2$ alloy structure.

Chrono-amperometry (the IEV method) [21] provides general information concerning the porosity of the tin coating in the pristine state. Furthermore, this method can also indicate if the amount of tin deposited is enough to cover and protect the surface or if the quantity is too low. In the latter case, after the flow-melting process, the $FeSn_2$ alloy and the base steel will be exposed at the top of the base striae.

XRF spectroscopy analysis identifies the average amount of tin present on the tinplate surface without making any distinction between pure and alloyed tin. However, these results show an extremely good correlation with the total tin thickness determined by the chrono-potentiometric method. Thus, after calibration, XRF spectroscopy can in some cases substitute the traditional chrono-potentiometric method. The positive aspects of XRF spectroscopy are that it implements fast and non-destructive measurements which can be performed in situ on the tinplate production line.

SEM analysis combined with chrono-potentiometry provides some of the missing information. SEM images of tinplate surface at different chrono-potentiometric stripping times can show, as a function of depth, the evolution of the surface porosity, the coexistence of different phases and the coverage of the $FeSn_2$ alloy.

AES depth profiling allows assessment of the local thickness of the tin layer. This analysis, carried out on a statistically relevant number of points of the tinplate surface, allows the determination of the minimum film thickness. This last parameter is much more meaningful than the average value of tin layer thickness for corrosion studies. AES gives information about the distribution of the elements at the interface region.

2.4 Conclusions

The chemical and morphological analysis of five different tinplate materials studied using a multi-technique approach leads to the following conclusions:

- The simple representation of tinplate presented in the literature as a sequence of consecutive layers of tin, $FeSn_2$ alloy and base steel substrate does not correspond to the real stratigraphy of commercial tinplates. The real structure consists of a superficial layer of pure tin, an intermediate interface characterized by the co-presence of tin, FeSn2 alloy, iron and base steel.
- Tinplate materials are characterized by features such as porosity, scratches and local variations in Sn film thickness. Moreover, the concept of the intermediate $FeSn_2$ alloy layer should be replaced by a broad diffusion interface characterized by the coexistence of tin, iron and tin-iron alloy. The nature and the structure of this interface can drastically affect the corrosion behaviour of tinplates and thus their functionalities as food container materials.
- There is no a single characterization technique that can provide all the necessary information about tinplate structure. However, the combination of electrochemical methods, SEM, AES, XRF spectroscopy and WLI proves to be an extremely powerful combination for an exhaustive characterization of tinplates.

3 Corrosion mechanisms of tin in complexing acids

Goal

The literature has revealed that a wide range of foods contain organic acids: citric, malic, oxalic, tartaric, etc. The protons provided by these acids, together with oxygen, are the most common oxidizing agents. The goal of this chapter is to study the mechanisms and kinetics of the corrosion reactions of tin in model electrolytes constituted by acidic buffer solutions of oxalic, citric and malic acids. The values of pH and concentrations of electrolytes were chosen according the typical values reported the literature [34,35]. Solutions containing the same acid buffered at pH 3.0 and 4.5 were used to study the effect of the complexing strength in conjunction with proton concentration. A partial de-aeration of the system was adopted to study the effect of the oxygen, since this molecule is a ubiquitous oxidant present in all cans independently of the type of food but part of the canning process.

3.1 Materials and Methods

3.1.1 Electrodes and electrolytes

Electrochemical measurements carried out in static conditions were performed on pure Sn (99.99+%, Goodfellow) supplied, as rolled, in the form of 1 mm thick disks with a diameter of 15 mm. The active area of the working electrode during the tests was 0.785 cm^2. Disk electrodes made of pure Sn (99.999+%, Goodfellow), with a diameter of 5 mm and an exposed area of 0.196 cm^2, were employed for performing electrochemical tests using a rotating disk electrode (RDE).

Prior to each electrochemical test, the samples were mechanically polished by means of a manual polishing machine (Struers DAP-U). Final polishing was achieved in three stages of 6 min each: first polishing with a SiC paper at 1200 grit, intermediate polishing with a SiC paper at 2400 grit and final polishing with a SiC

paper at 4000 grit. At the end of each polishing stage, the electrode surface was cleaned in ethanol (p.a. grade) by means of an ultrasonic bath for 10 min.

Freshly prepared buffer solutions of Citric, L-Malic and Oxalic acids were used as electrolytes for the electrochemical tests. For each buffer, two values of pH (3.0 and 4.5) and two concentrations (0.1 M and 0.01 M) were investigated. Buffer solutions were prepared by adding solid sodium hydroxide (Merck, puriss p.a.) to Citric (Sigma-Aldrich, BioUltra), L-(-)-Malic (abcr, puriss p.a.) and Oxalic (Sigma-Aldrich, puriss p.a.) acids according the calculated stoichiometric ratios. The pH was measured with a pH meter, Metrohm 654, and final pH adjustments were done with a solution of sodium hydroxide 10 M. Electrolyte conductivity was measured by the conductivity meter Meterlab CDM 210.

Table 13 shows the fractions of the individual components contained in each buffer solution calculated considering the equilibrium constants. **Table 14** reports the measured pH and conductivity values of all the electrolytes employed. In this work, the parameter named "Total Concentration" refers to the value of the initial concentration, expressed in mol/L, of organic acid used for the buffer preparation.

Table 13 Theoretical percentage of anionic species content in the buffer solutions at pH 3.0 and 4.5. Calculated according to the thermodynamic equilibrium considering the following pKa values: citric acid pKa1 3.13 pKa2 4.76 pKa3 6.39, malic acid pKa1 3.40 pKa2 5.20 and oxalic acid pKa1 1.25 pKa2 4.25.

Buffer	pH	% Anions			
		% H_3A	% H_2A^-	% HA^{2-}	% HA^{3-}
Citrate	3.0	55.34	43.96	0.70	< 0.001
	4.5	2.57	64.63	32.39	0.41
		% H_2A	% HA^-	% A^{2-}	-
Malate	3.0	71.40	28.42	0.18	-
	4.5	6.21	78.19	15.60	-
Oxalate	3.0	1.74	93.25	5.01	-
	4.5	0.02	37.05	62.93	-

Table 14 Experimental values of pH and conductivity of electrolytes employed in this work.

pH	[Total concentration]	Citrate		Malate		Oxalate	
		mS/cm	pH	mS/cm	pH	mS/cm	pH
3.0	**0.01**	0.55	3.02	0.43	3.07	1.03	3.06
3.0	**0.1**	3.11	3.05	2.15	2.99	7.41	3.02
4.5	**0.01**	0.99	4.51	0.82	4.50	1.52	4.50
4.5	**0.1**	8.65	4.53	7.48	4.52	12.60	4.49

Sn(II)-Complex formation constants for citrate, malate and oxalate buffers reported in **Table 15** were calculated, at different pH values, according to **Eq. 5** [34] from the data reported by Willey [35]. In **Eq. 5**, *L* is the total concentration of the complexing agent, including both protonated and deprotonated species while *K* is the global complex formation constant of a buffer at a certain pH. According to the literature review reported in **Chapter 1**, the complexation order *y* can be 2 or 1.

$$Sn^{2+} + yL \leftrightarrows SnL_y \qquad K = \frac{[SnL_y]}{[Sn^{2+}][L]^y} \tag{5}$$

Table 15 Sn complexation constants of the buffers, expressed in pK, for citrate, malate and oxalate buffers. Calculated based on the experimental data reported in the literature by Willey [35] and the two possible complexation orders.

Complexation order	pH	Complexation constants of the buffer (pK)		
		Citrate	Malate	Oxalate
1 (SnL)	**3.0**	5.18	4.24	8.54
	4.5	8.16	6.70	10.40
2 (SnL_2)	**3.0**	6.19	5.26	9.55
	4.5	9.17	7.72	11.42

3.1.2 Electrochemical measurements

The electrochemical tests were performed in the absence of light and at low concentrations of residual oxygen to mimic the internal environmental conditions of food packaging. The de-aeration of electrolytes was achieved by bubbling an Ar flow (Carbagas, purity 4.8) in the electrochemical cell for 2 h prior to each test. To maintain a constant concentration of oxygen, Ar was bubbled in the cell for the entire duration of the test.

All the electrochemical measurements were carried out on an Autolab PGSTAT30 potentiostat equipped with a multiplex MUX.MULTI4 module and a rotating disc electrode (RDE).

Static electrochemical tests were performed, after the two hours needed for the electrolyte de-aeration, in a 1.25 L electrochemical cell equipped with 5 independent working electrodes (WEs) sharing a common gold mesh counter electrode (CE) (31.5 cm^2) and a statured calomel reference electrode (SCE) (the SCE potential is +0.244 V with respect to the hydrogen standard electrode). OCP was alternatively

measured every 80 s for 20 s over the two hours needed for the system stabilization. Afterwards, the polarization resistance of each electrode was assessed by a potentiodynamic polarization from -10 mV vs. OCP to +10 mV vs. OCP with a scan rate of 0.002 V/s.

Cathodic and anodic branches of potentiodynamic polarization curves were recorded respectively from OCP to -1.2 V or -1.5 V vs. SCE and after 180 s of stabilization at OCP, from OCP to 0.7 V vs. SCE at a scan rate of 0.001 V/s. The experimental setup for the electrochemical measurements in static conditions is shown in **Figure 31**.

The dynamic electrochemical tests were performed after 1 h of de-aeration and OCP stabilization in a 0.3 L electrochemical cell equipped with an Sn RDE as the working electrode, a gold mesh as the counter electrode and a reference SCE. Potentiodynamic polarization curves were recorded from 0.05 V vs. OCP to -1 V vs. SCE with a scan rate of 0.001 V/s. **Figure 32** shows the experimental setup for the electrochemical measurements in dynamic conditions.

Figure 31 Experimental setup for the electrochemical tests performed in static conditions.

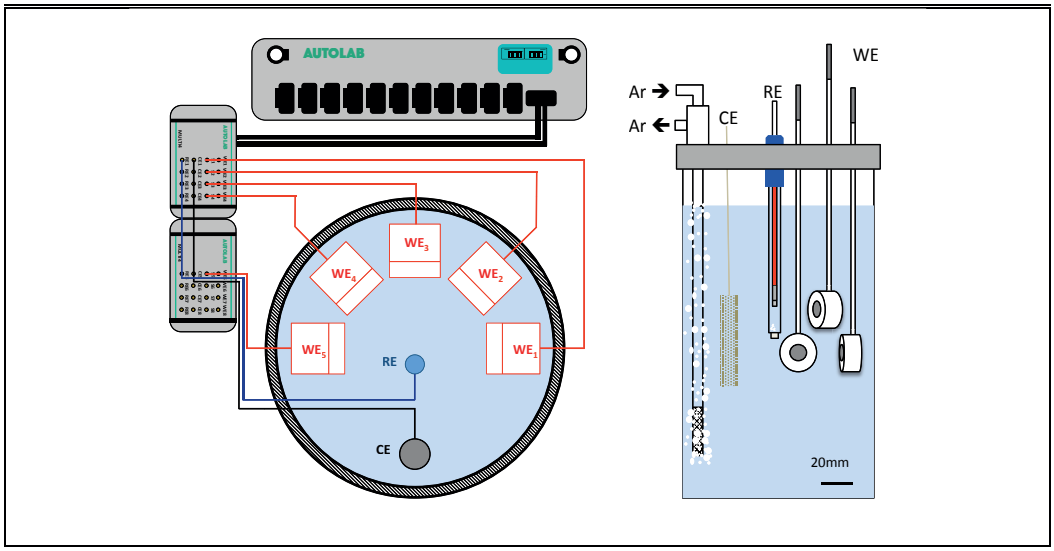

Figure 32 Experimental setup for the electrochemical tests performed in dynamic conditions.

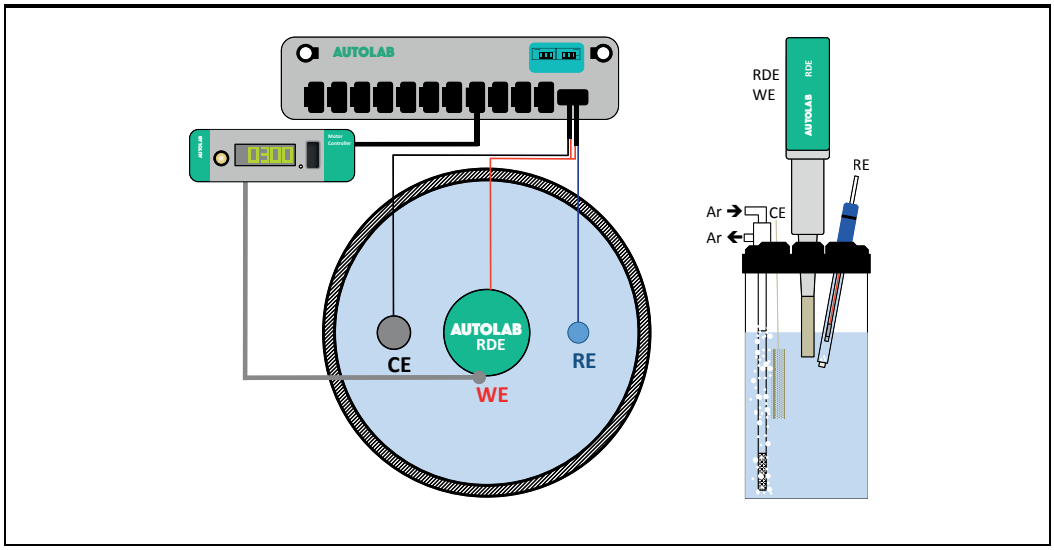

3.2 Results

3.2.1 Effect of the buffer system on the open circuit potential

Table 16 lists the OCP values measured in each buffer after 2 h of system stabilization and the corrosion potentials (E_{corr}) extracted from the PP curves. Interestingly, the OCP values correspond with the E_{corr}. Thus, clearly in these conditions tin undergoes active dissolution. It is interesting to highlight that OCP values of tin shift in the cathodic direction with an increase of the complexing strength of the solution. **Figure 33** shows that the cathodic shift of the OCP is directly related to the complexation constants of the buffers. The complexation strength of the solution is increased either by changing the type of anions, or by increasing the pH (**Table 15**). Thus, the OCP of tin can be theoretically determined by knowing the complexation strength of the solution in which the tin electrode is immersed.

Table 16 OCP values and corrosion potentials (E_{corr}) of tin electrodes measured in static conditions in the three buffered systems. Average value over 5 measurements.

pH	[Total concentration]	Citrate		Malate		Oxalate	
		OCP	E_{corr}	OCP	E_{corr}	OCP	E_{corr}
3.0	**0.01**	-0.590 ±0.010	-0.592 ±0.010	-0.569 ±0.006	-0.573 ±0.007	-0.669 ±0.006	-0.671 ±0.007
3.0	**0.1**	-0.625 ±0.005	-0.626 ±0.008	-0.599 ±0.007	-0.601 ±0.006	-0.734 ±0.012	-0.732 ±0.010
4.5	**0.01**	-0.682 ±0.008	-0.684 ±0.005	-0.647 ±0.004	-0.650 ±0.006	-0.732 ±0.006	-0.729 ±0.005
4.5	**0.1**	-0.703 ±0.008	-0.702 ±0.008	-0.663 ±0.006	-0.662 ±0.006	-0.769 ± 0.009	-0.766 ± 0.008

Figure 33 Relation between the OCP values of tin measured in all the [0.1] buffers and the buffer complexation constant calculated for the same buffers.

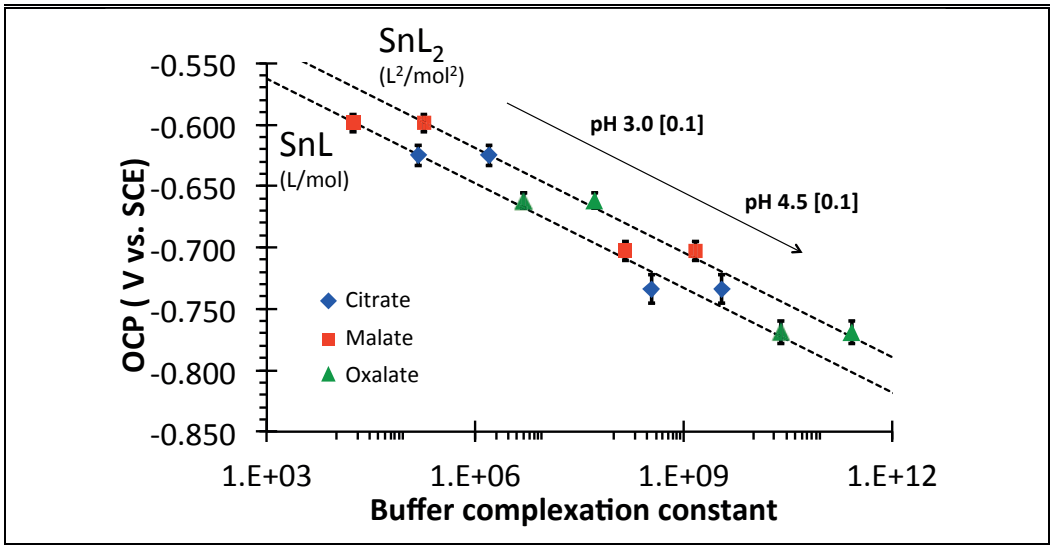

3.2.2 Anodic behaviour of tin

Figure 34 shows the active-passive behaviour of tin. From the corrosion potential to an overvoltage of 30–100 mV, the currents grow exponentially with respect to the potential applied. After this limited Tafel domain, the currents of the active region grow linearly until the passive potential (E_p) is reached.

Figure 34 Anodic potentiodynamic polarizations recorded in static conditions on tin in all citrate a), oxalate b) and malate c) buffers.

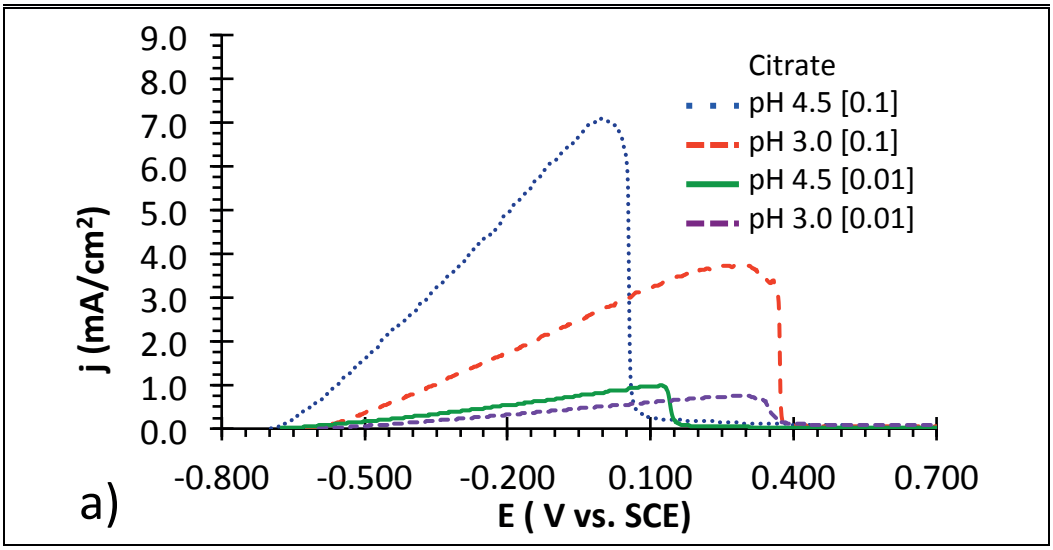

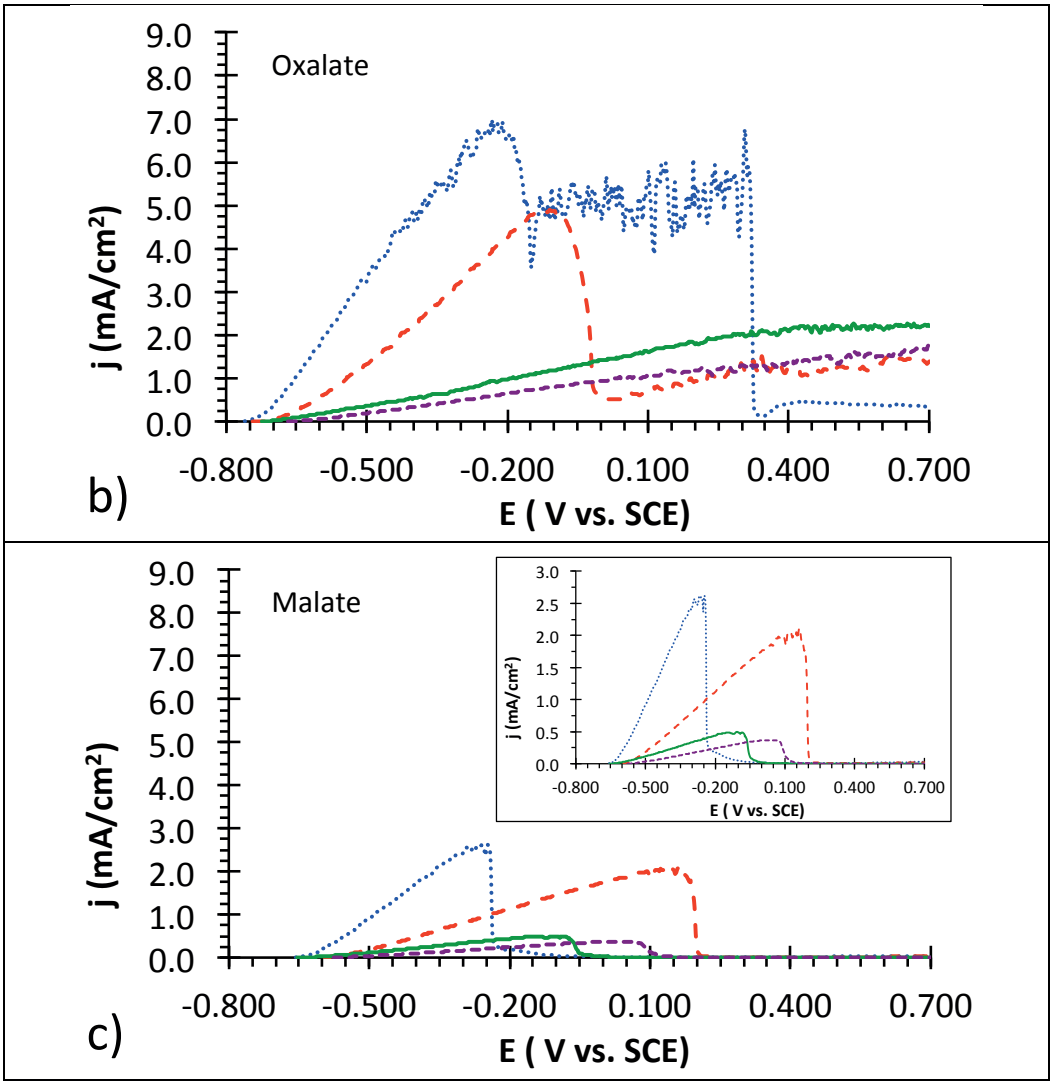

The linearity of the evolution of active currents with the applied potential suggests that the active dissolution is under ohmic control.

Figure 35 shows the active currents measured at -0.4 V vs. SCE, extracted from the anodic PP curves reported in **Figure 34**, plotted as a function of the buffer conductivities (**Table 14**). For the comparison, the ohmic drop effect has been disregarded because for the currents measured at -0.4 V vs. SCE, the calculated ohmic drop is < 1 mV . The linear relation between active currents of all the buffers and the solution conductivities confirms that the active domain, far from the E_{corr}, is purely under ohmic control and that the type of buffer does not exert any influence. Moreover, it should be pointed out that the mechanism reported in the literature [42,65,68], according to which the tin dissolution is mediated by the adsorption of the anions on the tin surface, does not seems to take place.

Figure 35 Relation among the buffer conductivities and the active currents extracted from the anodic potentiodynamic polarization curves for an applied potential of -0.4 V vs. SCE.

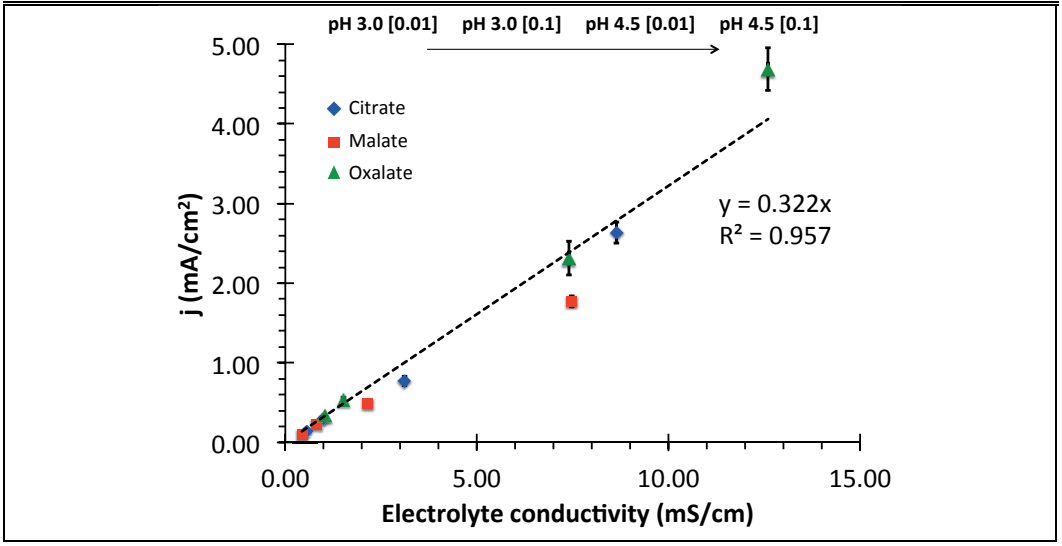

In citrate and malate buffers, the passive potentials are mainly pH dependent. In these two buffers, the passive potentials of tin measured at the same pH but with different total concentrations are within a range of potential (+/- 100 mV).

A well-defined active-passive transition is observable only in citrate and malate buffers, while in oxalate buffers, the passivity is observed only in the most concentrated buffers. This suggests that the passivation mechanism of tin in oxalate buffer is initiated by the precipitation of tin oxalates on the tin surface. Clearly, this mechanism will depend on the concentration of the oxalate buffer. The higher the concentration of the buffer, the higher the amount of precipitates and thus the passivation will occur at lower potentials. The partial coverage of the surface with the oxalates will determine the increase in the currents at the porosity site. This effect can be due to the instability of current characterizing the passive domain of tin in oxalate buffers.

The current densities associated with the passive domain (**Table 17**) increase together with the complexing strength of the anions, while for the same buffer, currents increase with the total concentration but are either weakly or not affected by the pH of the buffer.

Table 17 Passive plateau current densities (j µA/cm^2) of tin electrodes measured in the potential interval 0.650–0.700 V vs. SCE in static conditions in the three buffer systems. Average values over 5 measurements.

pH	[Total concentration]	Passive plateau j_p (µA/cm^2)		
		Citrate	Malate	Oxalate
3.0	**0.01**	50.0 ± 21.5	6.9 ± 5.1	No passivation
3.0	**0.1**	92.6 ± 34.1	11.1 ± 5.5	1557.6 ± 664.0
4.5	**0.01**	13.5 ± 5.8	5.8 ± 1.3	No passivation
4.5	**0.1**	93.6 ± 41.7	10.9 ± 6.9	395.0 ± 111.0

3.2.3 Cathodic behaviour of tin

Figure 35 shows the cathodic polarization curves of tin in the three buffer systems. A short cathodic plateau in the range of potential from the E_{corr} and the potential of onset of the water reduction reaction is present in all the systems. The low currents associated with these cathodic plateaux are listed in **Table 18**; their values vary from -2 to -9 µA/cm^2 independently of the pH. Thus, it is clear that this plateau cannot be attributed to the proton reduction.

Figure 35 Cathodic potentiodynamic polarizations recorded in static conditions on tin in all citrate a), oxalate b) and malate c) buffers.

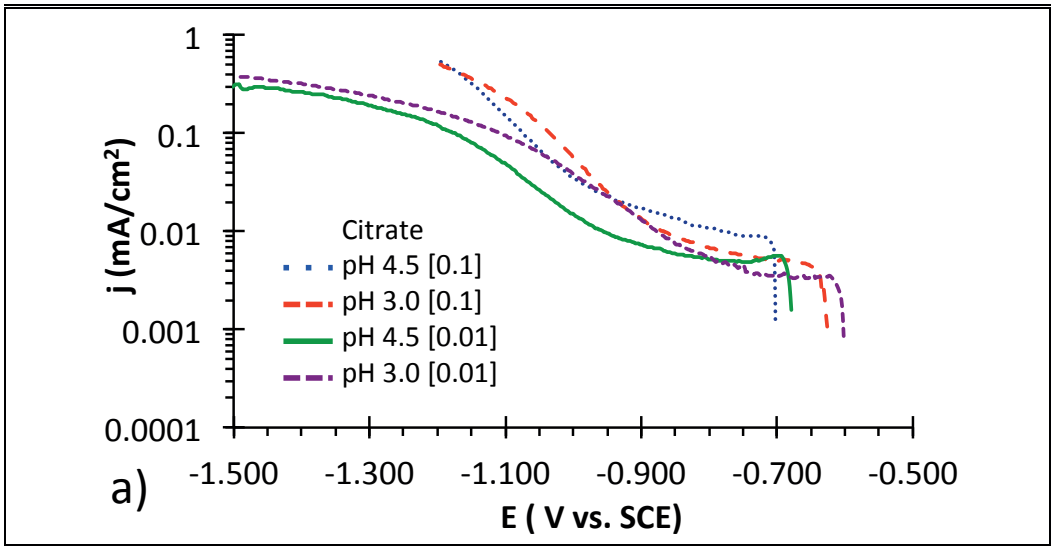

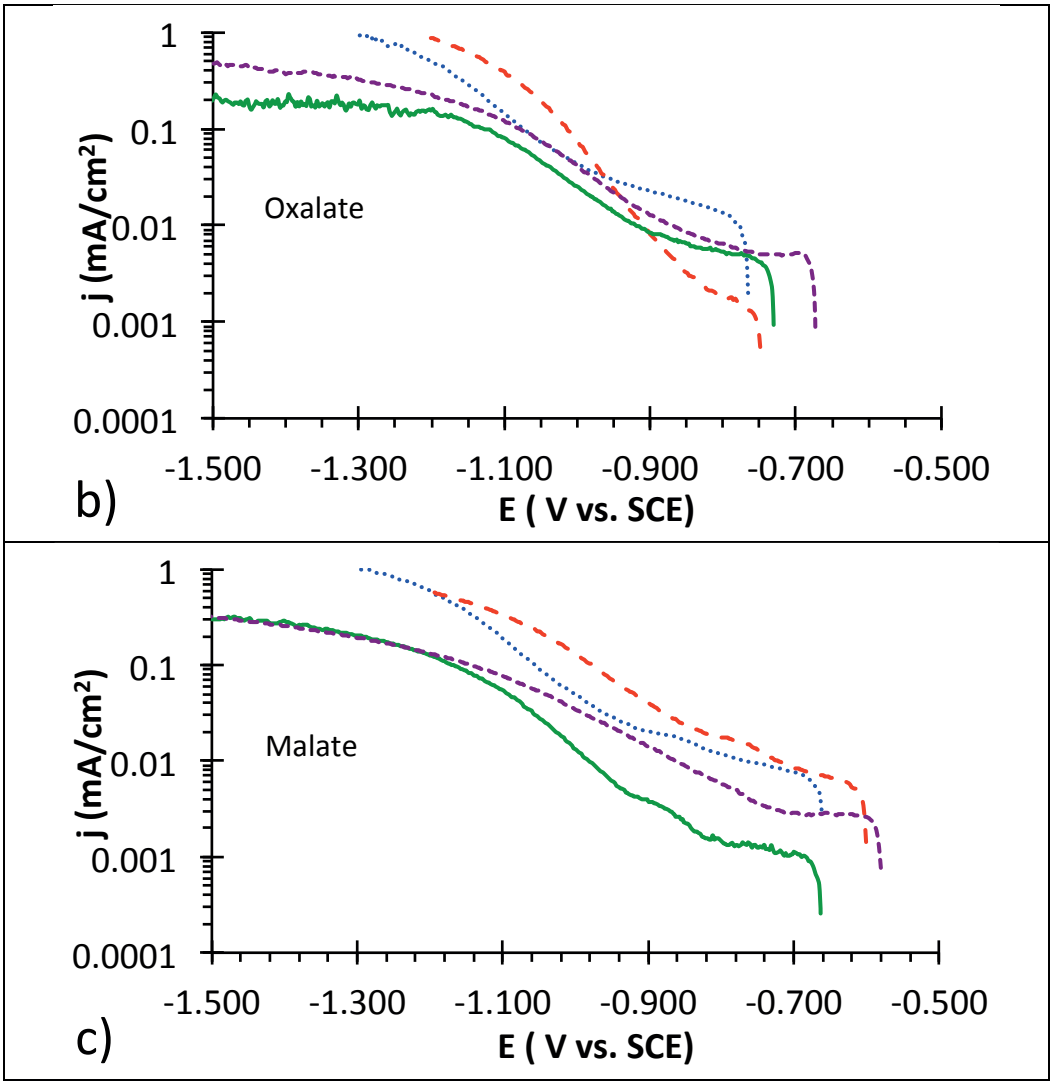

Table 18 Cathodic plateau current densities (j µA/cm^2) of tin electrodes measured in static conditions in the three buffer systems, between -0.650 and -0.800 vs. SCE. Average value over 5 measurements.

pH	[Total concentration]	Cathodic plateau j (µA /cm^2)		
		Citrate	Malate	Oxalate
3.0	**0.01**	-7.5 ± 4.0	-3.8 ± 2.6	-5.8 ± 3.0
3.0	**0.1**	-5.4 ± 2.8	-5.3 ± 2.5	-6.0 ± 4.2
4.5	**0.01**	-3.5 ± 1.3	-2.1 ± 0.9	-4.0 ± 1.8
4.5	**0.1**	-7.8 ± 5.0	-6.2 ± 3.1	-9.2 ± 5.2

Figure 36 shows the PP values recorded in aerated [0.1] citrate buffer at pH 3.0. Interestingly, now the currents associated with the cathodic plateau increase to -24 µA/cm^2. Thus, it is possible to state that the cathodic plateau included between -0.700 V and -0.8 V vs. SCE is due to the oxygen reduction based on a mechanism under diffusion control. This evidence suggests that the oxygen

reduction is the main cathodic reaction responsible for this plateau and determines the kinetics of tin dissolution.

Figure 35 shows that after the cathodic plateau, moving towards more negative applied potentials (> -0.9/-1 V vs. SCE), the water reduction reaction becomes the main cathodic process. At these potentials, the current is strongly potential affected by the total ion concentration but not by pH. This effect can most likely be attributed to the fact that the buffer systems at higher concentrations are able to supply a higher number of protons that will be used for the water reduction reaction. Vice versa, for a tenfold lower buffer concentration, the number of protons available for the water reduction reaction will decrease greatly. This hypothesis is also supported by the fact that the cathodic currents associated with the two concentrations differ by roughly 10 times.

Figure 36 Cathodic potentiodynamic polarizations recorded in static conditions on tin in [0.1] citrate buffer at pH 3. The curves were recorded in aerated condition at 25 °C with a theoretical oxygen concentration of 8.3 mg/L.

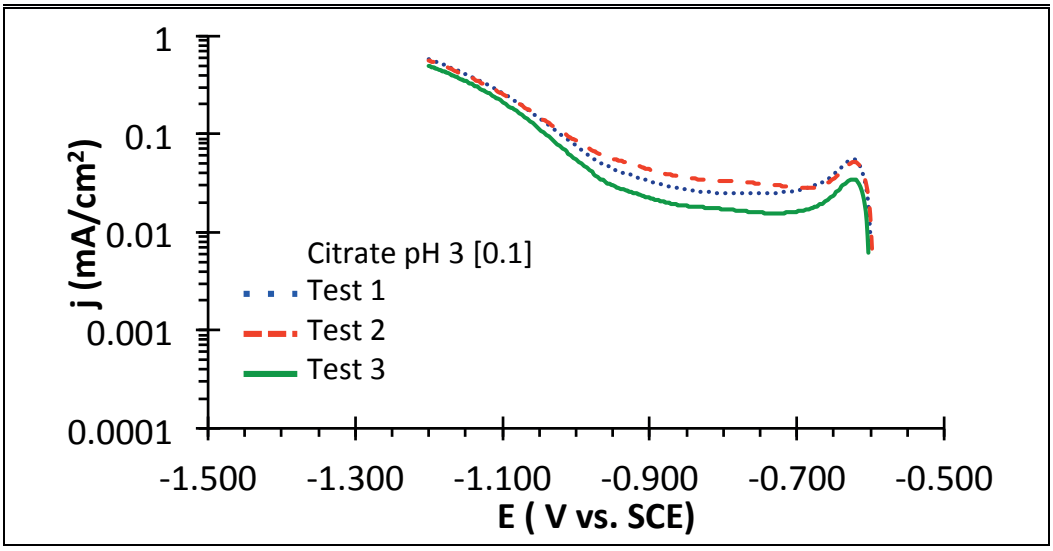

3.2.4 RDE experiments

The use of RDE made it possible to study the kinetics of the cathodic reactions taking place in the potential region close to the corrosion potential characterized by the presence of a plateau of current. **Figure 37** shows the PP curves recorded in the cathodic domain using a tin RDE in all citrate and oxalate buffers. From the comparison of the different plots reported in **Figure 37**, it is apparent that neither

the pH nor the buffer type seems to play a role in the cathodic plateau currents. The imperfect flattening of the plateaux indicates that the cathodic reactions taking place in this region are most likely under mixed control. These observations support the assumption that the oxygen reduction reaction is responsible for this cathodic plateau. If hydrogen reduction were governing the cathodic kinetics, one would expect a marked effect of pH or acid concentration; however, from the RDE results it is clear that these two parameters do not play any role in the kinetics of the reaction associated with the cathodic plateau.

Figure 37 shows that the Tafelian region of the anodic domain is not under diffusion control. The PP value are independent of the rotation speed of the electrode.

Figure 37 Cathodic potentiodynamic polarizations recorded by means of RDE in dynamic conditions on tin in citrate a,b) and oxalate c,d) buffers.

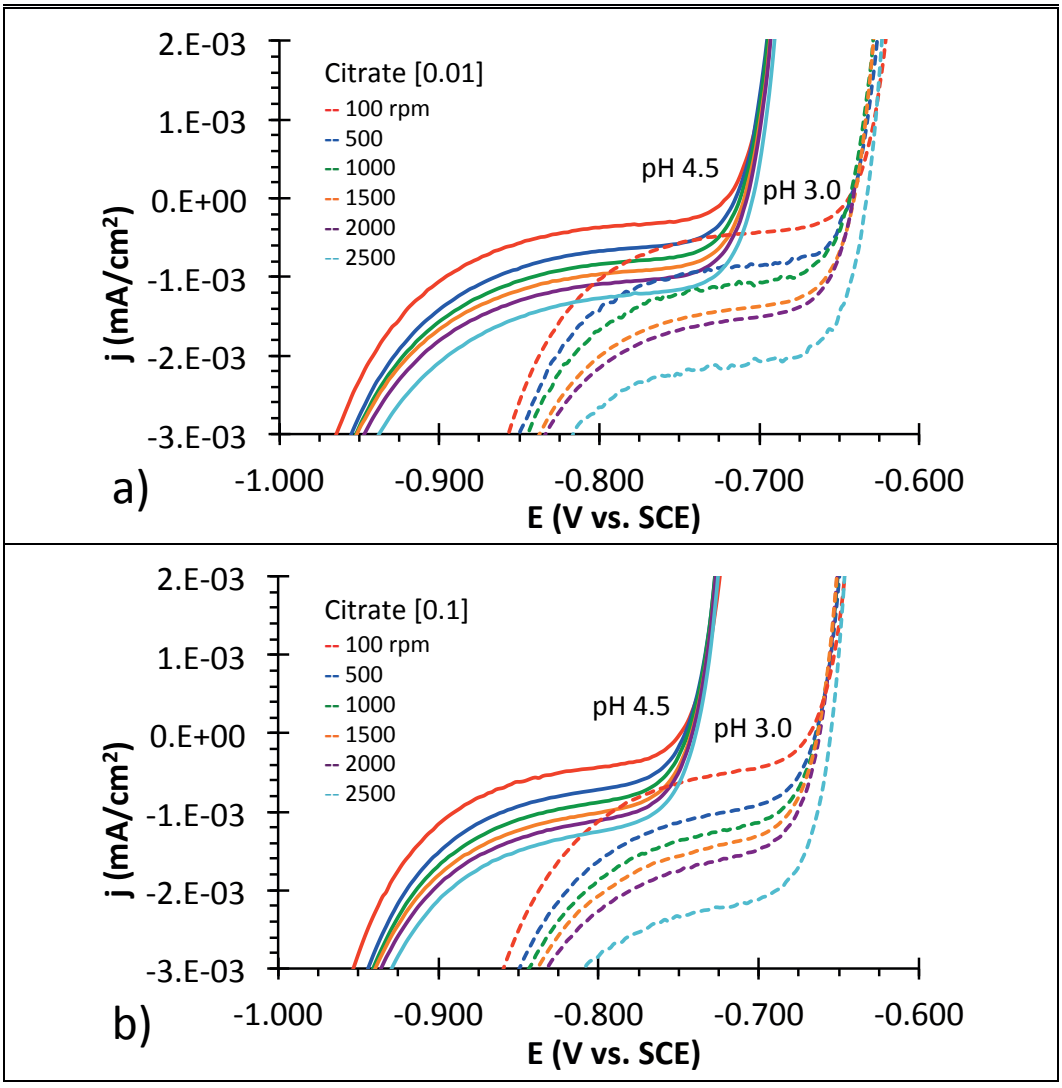

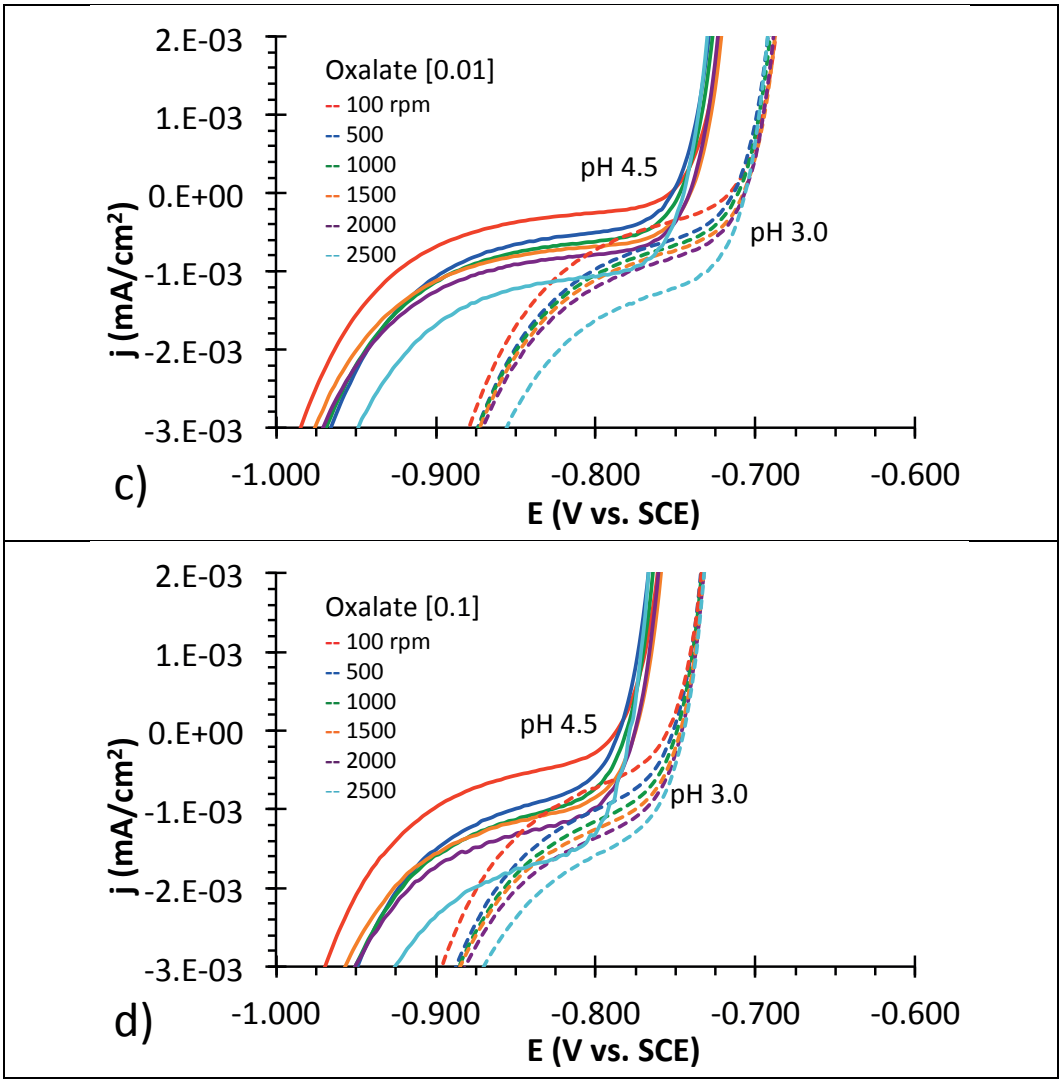

3.3 Discussion

3.3.1 Active dissolution kinetics

All anodic PP curves reported in **Figure 34** have an active region characterized by a limited Tafelian region close to the E_{corr} followed by a region in which the current increases linearly with the applied potential. The anodic Tafel slopes b_a determined by means of RDE are reported in **Table 19.** Clearly, the type of anions and the complexing strength of the solutions determine small variations in the b_a values.

Table 19. Anodic Tafel slopes b_a for tin oxidation determined on the anodic branch of the potentiodynamic polarizations of tin measured with the RDE setup (100 rpm) in citrate and oxalate buffers. *Not measured in malate buffers.

pH	[Total concentration]	b_a (mV/dec)		
		Citrate	Malate*	Oxalate
3.0	**0.01**	34.03 ± 0.06	NA	29.74 ± 0.47
3.0	**0.1**	29.61 ± 0.07	NA	29.05 ± 0.78
4.5	**0.01**	30.48 ± 0.17	NA	27.60 ± 0.65
4.5	**0.1**	29.34 ± 0.78	NA	26.65 ± 1.27

Figure 38 shows that b_a values are in fact related to the complexing strength of the solution and thus the dissolution of tin in the Tafelian region is enhanced by the increase in the complexing strength of the anions present in the solution.

By subtracting tin ions, the complexing anions shift to the right of the equilibrium of tin dissolution reported in **Eq. 6**. Thus, the anodic kinetics of tin dissolution will become faster as the complexing strength of the solution increases. If the buffers have similar complexation strength, i.e. citrate buffer pH 4.5 and oxalate buffer pH 3.0, the b_a values and the dissolution kinetics will be similar.

$$Sn \leftrightarrows Sn^{2+} + 2e^{-} \; [49] \qquad (6)$$

Figure 38 Relation among the complexation constants of citrate and oxalate buffer systems [0.1] and the anodic Tafel slope b_a, determined with the RDE test, for a complexation stoichiometry of 1 a) and 2 b).

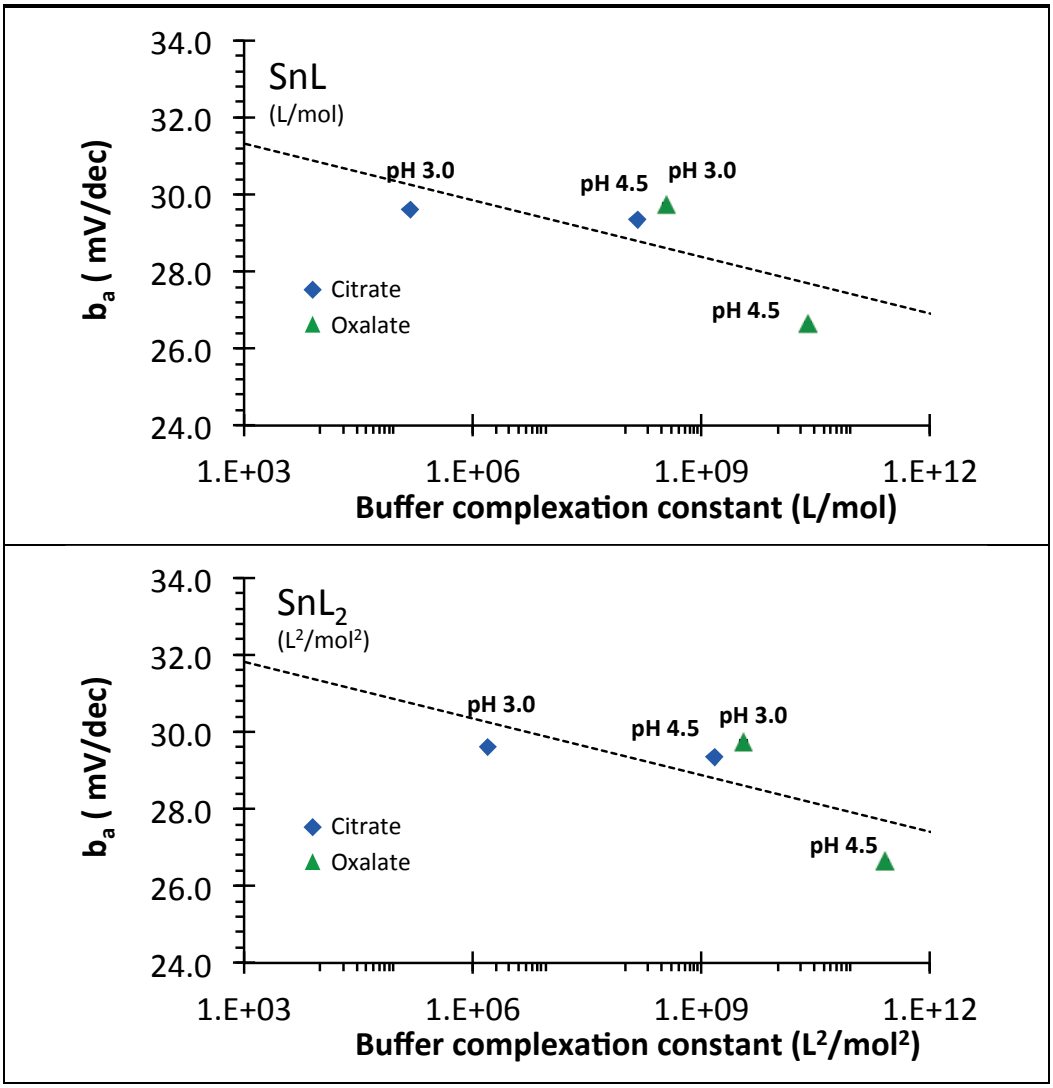

After the Tafel region, the currents increase linearly and as shown in the results section, the dissolution of tin is under ohmic control. The effect of pH and type of anion will again become evident for the active-passive transition.

3.3.2 Passivation kinetics

Figures 39a and **39b** show the relation among the E_p values and the complexation strength of the three buffer systems [0.1] for a complexing stoichiometry of 1 and 2, respectively. All data are available for the test carried out at pH 4.5, while in oxalate buffer at pH 3.0, passivation was not reached at the analysed potentials.

These relations clearly demonstrate that for a given pH value, the E_p grows with the complexing strength of the solution. Thus, the chemistry of the solutions plays a crucial role at constant pH by determining the onset of passivation.

Figure 39 Relation among the complexation constants of all buffer systems [0.1] and the passive potentials E_p for a complexation stoichiometry of 1 a) and 2 b).

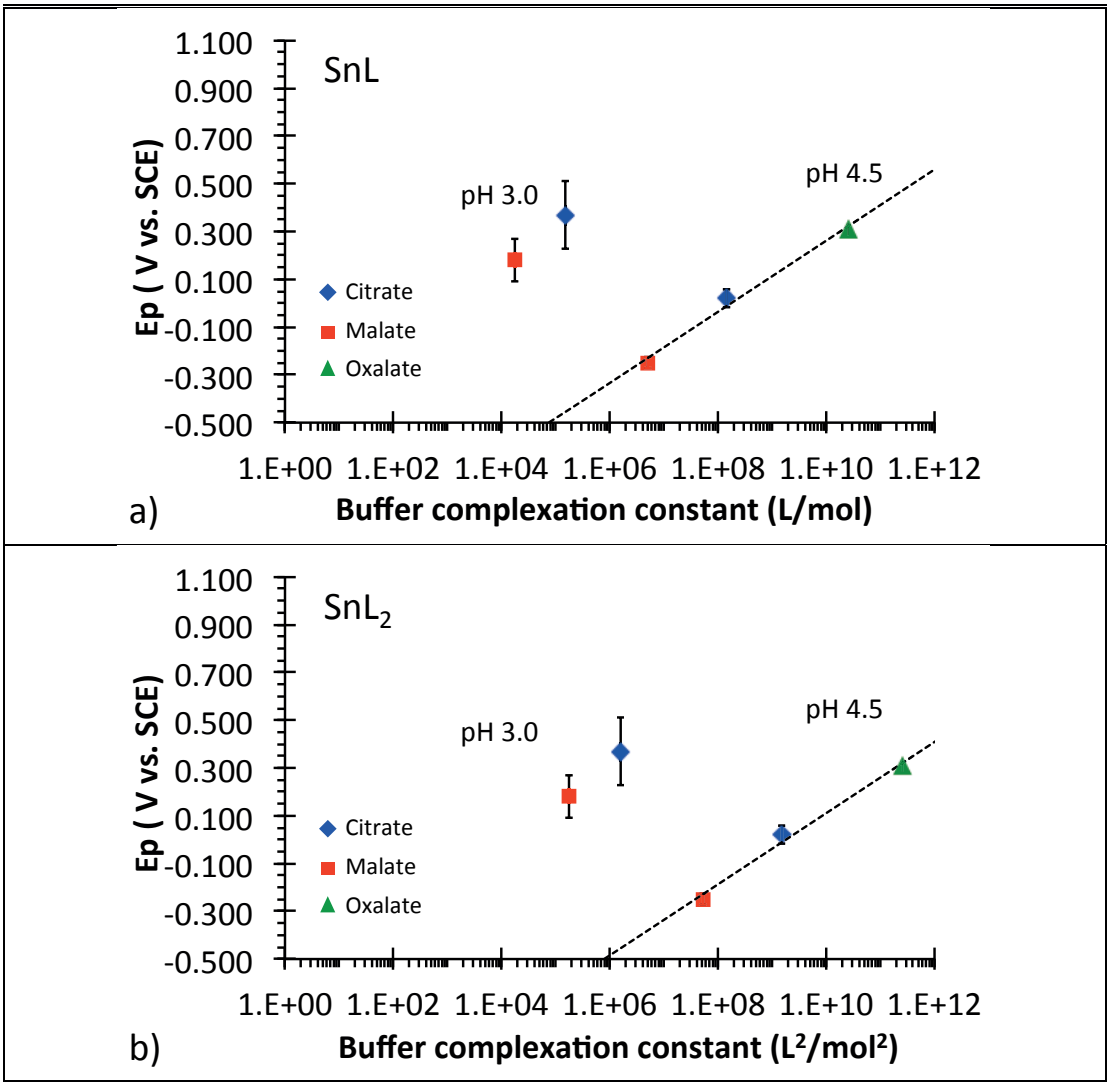

The double dependence of E_p on pH and complexation strength confirms that the passivation mechanism of tin follows that proposed in **Eq. 7** rather than the one proposed in **Eq. 9.**

The analysis of the shift in E_p as a function of pH gives a further confirmation of the mechanism proposed in **Eq. 7**. Considering the same buffer, the experimental E_p values shift lower by nearly 200 mV for an increase in pH of 1.5 points, from pH 3.0 to pH 4.5. If the passivation mechanism were that proposed by **Eq. 9**, according to

Eq. 10, the cathodic shift would have been close to 100 mV. Considering **Eq. 8**, the cathodic shift due to a variation in pH of 1.5 is 180 mV plus the contribution of the tin ion concentration. This last shift value is coherent with the cathodic shift of E_p observed experimentally.

Eq. 8 also explains the reason why at constant pH, E_p increases with the increase in the complexing strength of the solution. By increasing the complexing strength of the buffer, the tin ion concentration decreases and thus the last term of **Eq. 8** increases, while the others terms remain constant at constant pH.

$$Sn^{2+} + 2H_2O \leftrightarrows SnO_2 + 4H^+ + 2e^- \text{ [49]} \quad (7)$$

$$E_{rev,Sn^{2+}/SnO_2} = -0.77 - 0.1182pH - 0.0295\log(Sn^{2+}) \text{ [49]} \quad (8)$$

$$Sn + 2H_2O \leftrightarrows SnO_2 + 4H^+ + 4e^- \text{ [49]} \quad (9)$$

$$E_{rev,Sn/SnO_2} = -0.104 - 0.0591pH \text{ [49]} \quad (10)$$

In **Eq. 8**, the second term related to pH (-0.1182pH) exerts more influence than the third term related to tin ion concentration (-0.0295log(Sn^{2+})). Thus, it is clear why when the pH changes, the role of the complexing strength of the solution becomes negligible. In all cases, keeping the type of buffer constant at pH 4.5, E_p is lower than that measured at pH 3.0, despite the complexation strength being higher.

3.3.3 Oxygen reduction reaction kinetics

As highlighted in the results section, RDE tests demonstrated that the ORR is the cathodic process responsible for the cathodic plateau.

Figure 40 shows the Kouteki–Levich plot related to RDE tests. The plots also show the theoretical evolution of the limiting currents (j_l) for oxygen reduction according to a 4-electron process (**Eq. 2**) and a 2-electron process, which may take place at high rotation rates (**Eq. 11**) [76,77].

$$O_2 + H_2O + 2e^- \rightarrow H_2O_2 + 2OH^- \quad (11)$$

The theoretical j_l values were calculated according to the Levich equation (**Eq. 12**), in which *F* is the Faraday constant (96485 C/mol), *c* is the concentration of oxygen in the bulk (0.01 ppm), *D* is the coefficient of diffusion of oxygen in pure water at 25 °C (2.51×10^{-5} cm^2/s [41]), *v* is the kinematic viscosity of water at 25 °C (8.93×10^{-3} cm^2/s) and ω is the angular velocity in rad/s.

$$|j_l| = 0.62nFc_{O_2,b}{D_{O_2}}^{2/3}\nu^{-1/6}\omega^{1/2} \quad (12)$$

In citrate buffers, the j_l values for the ORR are independent of pH and total concentration (**Figure 40a)**. In contrast, in oxalate, the increase in pH results in a decrease of the j_l values for the ORR for low rotation rates (**Figure 40b**). This can be explained by considering that the oxalate anions could be more easily adsorbed at the tin-solution interface than the citrate anions. However, due to the previous evidence of the absence of absorption of anions on the tin surface, the effect can more plausibly be related to changes in the solution viscosity or the oxygen diffusion coefficient induced by the pH and buffer concentration. The comparison between theoretical trends of j_l for the ORR and the j_l for the ORR measured on tin in citrate and oxalate buffers suggests that for rotation rates > 1500 rpm, the ORR takes place with a 2-electron process. For lower rotation rates, the ORR approaches a 4-electron process because the high rotation rates lead to the elimination of H_2O_2 from the electrode surface before its further oxidation to HO^-. The transition between the two mechanisms is most likely a mixed process [77,78]. The contribution of the ORR to the overall cathodic reaction can be quantified from the slope of the linear regions of the Kouteki–Levich plots included from 1500 rpm and 100 rpm. The j_l values for the ORR ($j_{l\ O2/OH^-}$) on tin in citrate and oxalate buffers calculated at 100 rpm are listed in **Table 20.**

Figure 40 Kouteki–Levich plot for tin electrode citrate a) and oxalate b) buffers.

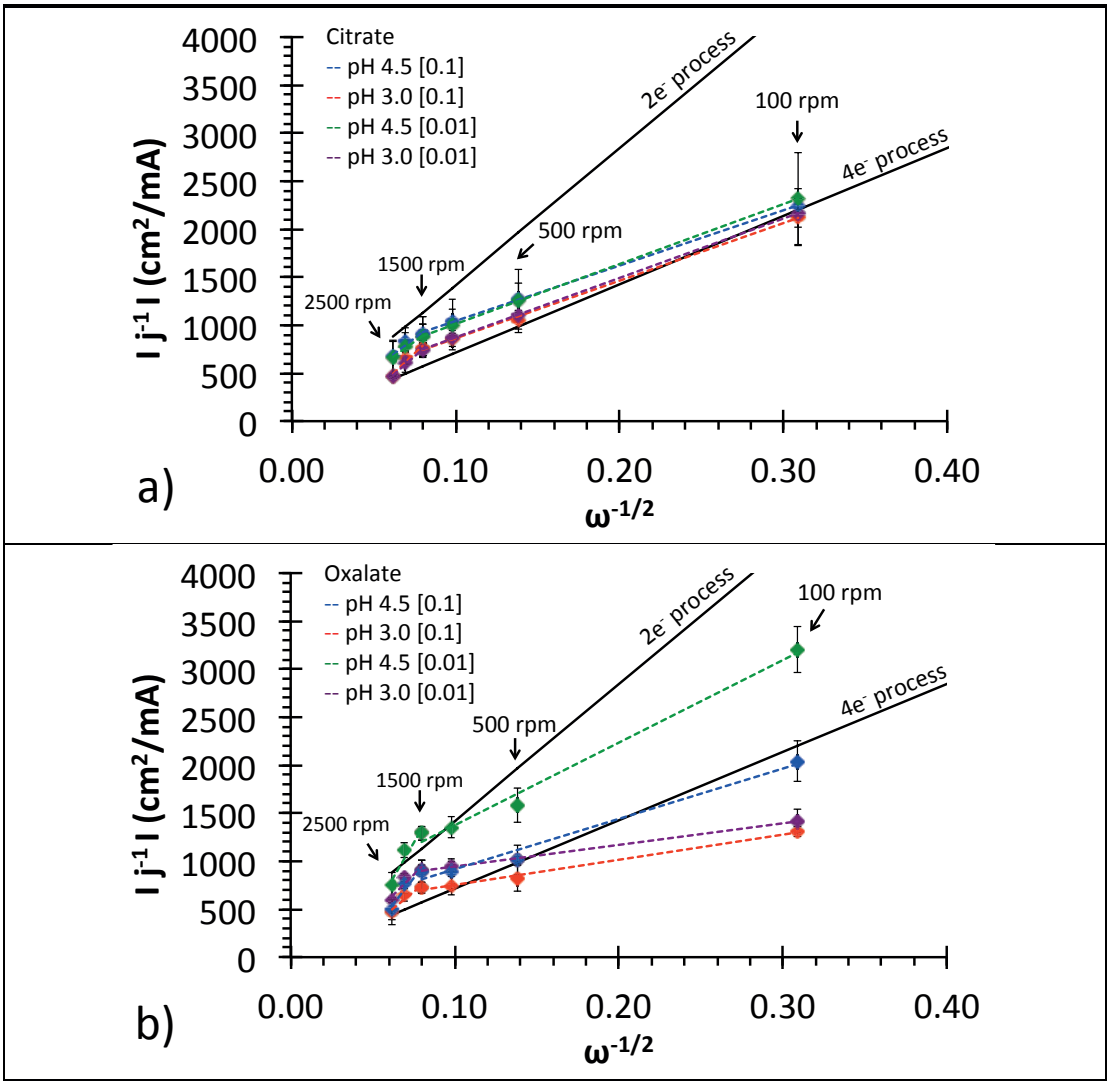

Table 20 Limiting current densities for the ORR for tin in citrate and oxalate buffers calculated at 100 rpm. *Not measured in malate buffers.

pH	[Total concentration]	Oxygen reduction reaction $j_{l\ O2/OH^-}$ (µA /cm^2)		
		Citrate	Malate*	Oxalate
3.0	**0.01**	0.52 ± 0.04	NA	1.46 ± 0.28
3.0	**0.1**	0.55 ± 0.09	NA	1.25 ± 0.11
4.5	**0.01**	0.53 ± 0.09	NA	0.38 ± 0.04
4.5	**0.1**	0.56 ± 0.02	NA	0.62 ± 0.05

$j_{l\ O2/OH^-}$ can be subtracted to the cathodic branch of the corresponding PP curve to obtain the cathodic polarization curve of tin due only to the HER. This will allow the study of the kinetics of the HER on tin.

3.3.4 Hydrogen evolution reaction kinetics

Figure 41 shows the correction procedure of the cathodic polarization curve of tin in [0.1] citrate buffer at pH 3.0. In all cases, the curves recorded with the RDE setup at 100 rpm approach those recorded with the static setup for both high cathodic applied potentials and anodic potentials.

Figure 41 Potentiodynamic polarization of tin in citrate buffer at pH 3.0 with a total concentration of [0.1] recorded with the static setup a) and RDE setup b). Curve c) is the cathodic branch of curve b) corrected by subtracting $j_{l\ O2/OH-}$.

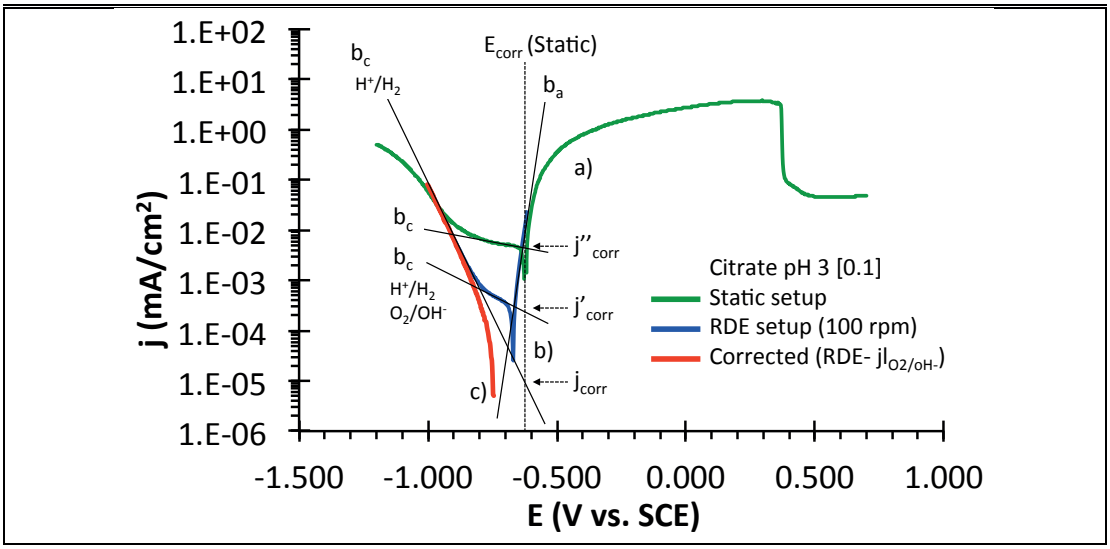

The intercept of the cathodic Tafel line at the corrosion potential E_{corr} makes it possible to determine the kinetics of the corrosion of tin. **Figure 41** clearly shows that extremely low oxygen concentrations, < 2 ppm (O_2 content declared for the Argon used for de-aeration), increase the corrosion rates of tin up to three orders of magnitude.

The kinetics of tin corrosion in the absence of oxygen, due only to the HER, are determined by the Tafel slope b_c extracted from the corrected curve c) reported in **Figure 41**.

Table 21 shows the b_c values for the HER determined in all citrate and oxalate buffers. The b_c values are close to 100 mV/dec independently of the type of buffer, pH and concentration. These b_c values are close to the theoretical value of 120 mV/dec reported by Landolt [41] for the HER according to the Volmer–Heyrovsky mechanism. The lower b_c value compared to the theoretical one could be due to the weak contribution of the Tafel reaction to the Volmer–Heyrovsky

mechanism as reported in the literature for the HER on tin [64]. The exchange current densities for the hydrogen ($j_{0\ H+/H2}$) on tin were extrapolated from the cathodic Tafel lines for the pure HER to the reversible potential of hydrogen. The $j_{0\ H+/H2}$ values, listed in **Table 22**, are close to the value of $\approx 10^{-4}$ µA/cm^2 reported by Landolt for tin [41]. The corrosion current densities (j_{corr}) for tin in the tested buffers (**Table 23**) were determined from the extrapolation at the E_{corr} of the cathodic Tafel line for the pure HER. Interestingly, the values of j_{corr} measured with this method are in good agreement with the j_{corr} reported by Sherlock et al. [34,45] (**Table 4**) for the same systems in the complete absence of oxygen. The other works presented in the literature [38,40,42,69] report j_{corr} values for tin of one to four orders of magnitude higher. These values are, however, compatible with the j_{corr} calculated for tin when considering the cathodic polarization curves measured in a not completely de-aerated medium, as for example in the situation shown in **Figure 41** by the curves a) and b).

Table 21 Cathodic Tafel slopes b_c for the HER determined on the corrected cathodic polarization of tin (100 rpm) in citrate and oxalate buffers. *Not measured in malate buffers.

pH	[Total concentration]	b_c (mV/dec)		
		Citrate	Malate*	Oxalate
3.0	**0.01**	94.77 ± 0.22	NA	104.18 ± 2.65
3.0	**0.1**	97.18 ± 1.95	NA	96.74 ± 2.15
4.5	**0.01**	98.27 ± 7.98	NA	98.65 ± 3.77
4.5	**0.1**	98.62 ± 8.96	NA	99.98 ± 1.84

Table 22 Exchange current density j_0 for the hydrogen electrode (H^+/H_2) on tin in citrate and oxalate buffers calculated at 100 rpm. *Not measured in malate buffers.

pH	[Total concentration]	j_0 H^+/H_2 (µA/cm^2)		
		Citrate	Malate*	Oxalate
3.0	**0.01**	7×10^{-5}	NA	1×10^{-4}
3.0	**0.1**	8×10^{-5}	NA	3×10^{-5}
4.5	**0.01**	9×10^{-5}	NA	7×10^{-6}
4.5	**0.1**	7×10^{-5}	NA	9×10^{-6}

Table 23 Corrosion current density (j_{corr}) obtained from the extrapolation to the E_{corr} of the cathodic Tafel lines for the pure HER. *Not measured in malate buffers.

pH	[Total concentration]	j_{corr} (μA/cm^2)		
		Citrate	Malate*	Oxalate
3.0	**0.01**	4 x 10^{-3}	NA	2 x 10^{-2}
3.0	**0.1**	1 x 10^{-2}	NA	5 x 10^{-2}
4.5	**0.01**	5 x 10^{-3}	NA	9 x 10^{-3}
4.5	**0.1**	5 x 10^{-3}	NA	3 x 10^{-2}

Based on the previous consideration, in the absence of oxygen, the j_{corr} of tin corresponds to the cathodic current density of the HER on the tin. Thus, the j_{corr} of tin can be theoretically calculated using the Volmer–Butler equation as given in **Eq. 13.**

$$j_{corr,Sn} = j_{c,HER}Sn = j_{0,H^+/H_2}\ exp\left(-\frac{E_{corr,Sn}-E_{rev,HER}}{\beta_{c,HER}}\right) \quad (13)$$

Table 24 shows the j_{corr} of tin calculated according to **Eq. 13** considering the following parameters: average value of b_c determined in this work in complexing acid buffer (100 mV/dec) (b_c=2.303 β_c [41]), the literature value of j_0 H^+/H_2 (10^{-4} μA/cm^2) [41], the measured $E_{corr,Sn}$ and calculated $E_{rev,HER}$ according to the pH by means of Nernst's equation.

Interestingly, the j_{corr} values theoretically calculated (**Table 24**) are extremely close to the j_{corr} experimentally determined in the three buffers (**Table 23**). Thus, it is possible to state that the pH and the E_{corr} of tin are the two parameters needed to determine the kinetics of corrosion of tin in de-aerated media due only to the HER. Thus, for a given pH, the differences in the corrosion rates of tin in malate, citrate and oxalate buffers are due to the corrosion potential that tin assumes in the different buffers.

Figure 33 shows the cathodic shift of the corrosion potential of tin with the increase in the complexing strength of the buffers. Thus, if the HER is the only cathodic process, the corrosion rate of tin will increase with the complexing strength of the buffer. This finding explains why Sherlock et al. [34] and Gouda et al. [38] found that the corrosion rate of tin increases with the complexing strength of the type of anion.

Table 24 Corrosion current density (j_{corr}) calculated using the Volmer–Butler equation for the HER on tin considering b_c equal to 100 mV/dec and $j_0 H^+/H_2$ equal to 10^{-4} μA/cm^2.

pH	[Total concentration]	j_{corr} (μA/cm^2)		
		Citrate	Malate*	Oxalate
3.0	**0.01**	5×10^{-3}	3×10^{-3}	3×10^{-2}
3.0	**0.1**	1×10^{-2}	6×10^{-3}	1×10^{-2}
4.5	**0.01**	5×10^{-3}	3×10^{-3}	5×10^{-2}
4.5	**0.1**	9×10^{-3}	2×10^{-3}	4×10^{-2}

3.4 Conclusions

This chapter has provided an overview of the electrochemical behaviour of tin in the typical corrosive environment derived from the literature review for canned acid products. Moreover, the use of the rotating disk electrode allowed identification of the mechanisms and the kinetics of tin dissolution.

- Tin is active in buffered acid media containing complexing anions and low residual oxygen concatenations.
- In the active dissolution of tin under cathodic control, the oxygen reduction reaction (ORR) and the hydrogen reduction reaction (HER) control the rate of tin dissolution.
- The ORR is under diffusion control and thus the rate of tin dissolution under natural convection can be determined by means of Fick's law, considering the initial oxygen concentration, the diffusion coefficient of the oxygen in the electrolyte and the kinematic viscosity of the electrolyte.
- The rate of tin dissolution due to acid corrosion can be calculated using the Volmer–Butler equation for the HER on tin. The Tafel constant and the hydrogen evolution exchange current densities are independent of the buffer and are respectively 100 mV/dec and 10^{-4} μA/cm^2. The reversible potential of hydrogen and the corrosion potential of tin are buffer dependent. The first is pH dependent according to the Nernst equation, while the second needs to be measured and is related to the complexing strength of the buffer with respect to tin ions.

4 Effect of galvanic coupling on the corrosion behaviour of tin and iron electrodes

Goal

The goal of this chapter is to study the influence of the galvanic coupling between tin and iron on their corrosion mechanism. This study was carried out in citrate and sulphate buffers. The two buffers were chosen to study the effect of a complexing and non-complexing electrolyte on the tin-iron galvanic coupling.

4.1 Material and methods

4.1.1 Electrodes and electrolytes

Pure Sn (99.99+%) and Armco iron supplied by GoodFellow Cambridge Ltd were used as materials for the galvanic coupling test. Sn electrodes were directly supplied in the form of 1 mm thick disks with a diameter of 15 mm, while the Armco iron electrodes, with the same diameter as for tin, were cut out from a 0.5 mm thick plate. The active area during the tests was 0.785 cm^2 for both materials.

Prior to each electrochemical test, the samples were mechanically polished up to 4000 grit with SiC paper and cleaned in pure ethanol by means of an ultrasonic bath according the procedure described in section 3.1.1.

The citrate and sulphate buffers were prepared according to the procedure described in section 3.1.1, with a total concentration of [0.1] and a pH of 3.0. **Table 25** reports the measured pH and conductivity values of the electrolytes employed.

Table 25 Experimental values of pH and conductivity of electrolytes employed in this work.

pH	[Total concentration]	Citrate		Sulphate	
		mS/cm	pH	mS/cm	pH
3.0	**0.1**	2.97	3.00	14.18	3.01
4.5	**0.1**	8.72	4.49	-	-

4.1.2 Electrochemical measurements

All the electrochemical tests were performed in the absence of light and at low residual oxygen concentration according the same de-aeration procedure as described in section 3.1.2. All the measurements were carried out by means of a potentiostat AUTOLAB PGSTAT30 equipped with a multiplex module MUX.MULTI4. A picoammeter Keithley 485 was used to measure the coupling currents flowing between tin and iron electrodes. For all measurements made with the picoammeter, tin was connected to the negative pole and iron to the positive pole.

The tests were performed in static conditions, after the two hours needed for the electrolyte de-aeration, in a 1.25 L electrochemical cell equipped with one tin working electrode (WE 1) and one iron working electrode (WE 2), sharing a common gold mesh as the counter electrode (CE) and a reference SCE placed between the tin and iron electrodes. OCP was alternatively measured every 30 s for 30 s over the two hours needed for the system stabilization. The resistance of the buffer solutions (Rint) was calculated according to **Eq. 14**, considering the resistance of the solution between the tin working electrode and the reference electrode measured by means of electrochemical impedance spectroscopy (EIS). The distance between the reference and working electrodes was 1.5 cm whereas the distance between the coupled tin and iron working electrodes was 3 cm. EIS was carried out at OCP by applying an amplitude of the signal of ± 10 mV and the solution resistance was measured as 10 KHz.

$$R_{int} = R_{EIS} \frac{d_{WE,Sn-RE}}{d_{WE,Sn-WE,Fe}} \quad (14)$$

Afterwards, before coupling, the polarization resistance of each electrode was assessed by means of PP from -10 mV vs. OCP to +10m V vs. OCP with a scan rate of 0.002 V/s. Cathodic and anodic branches of PP curves were recorded respectively from OCP to -0.1 V and from OCP to 0.1 V vs. SCE, at scan rate of 0.001 V/s.

Figure 42a shows the experimental setup for the electrochemical measurements carried out on uncoupled tin and iron electrodes. Afterwards, tin and iron electrodes were coupled through the picoammeter according to the experimental setup shown in **Figure 42b**. The current flowing between the two electrodes was measured with

the picoammeter and recorded every 5 s over 21 h. In parallel, the coupling potential was measured with the potentiostat. After the coupling, the electrodes were uncoupled and re-connected according the experimental set up shown in **Figure 42a.** At this point, the same electrochemical characterization carried out before coupling (OCP, EIS, polarization resistance and cathodic and anodic PP) was repeated to assess the electrochemical behaviour of tin and iron after the coupling.

The substitution in the measurement procedure of the coupling step with an immersion step in which the electrodes were kept uncoupled for 21 h allowed better understanding of the coupling effect. The schematization of the measure procedures is illustrated in **Figure 43.**

Figure 42 Experimental setups for electrochemical measurements carried out on tin and iron electrodes with an uncoupled a) and coupled b) configuration.

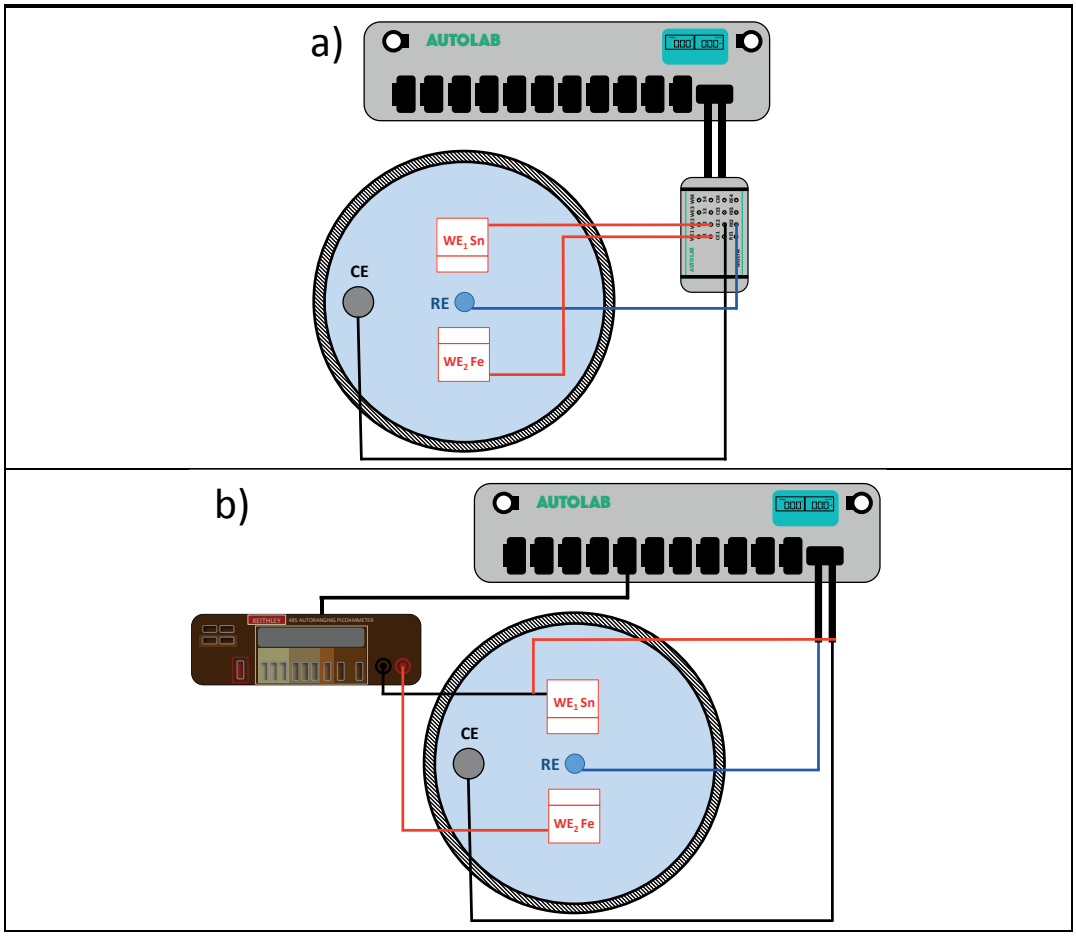

Figure 43 Measurement procedures used in the study.

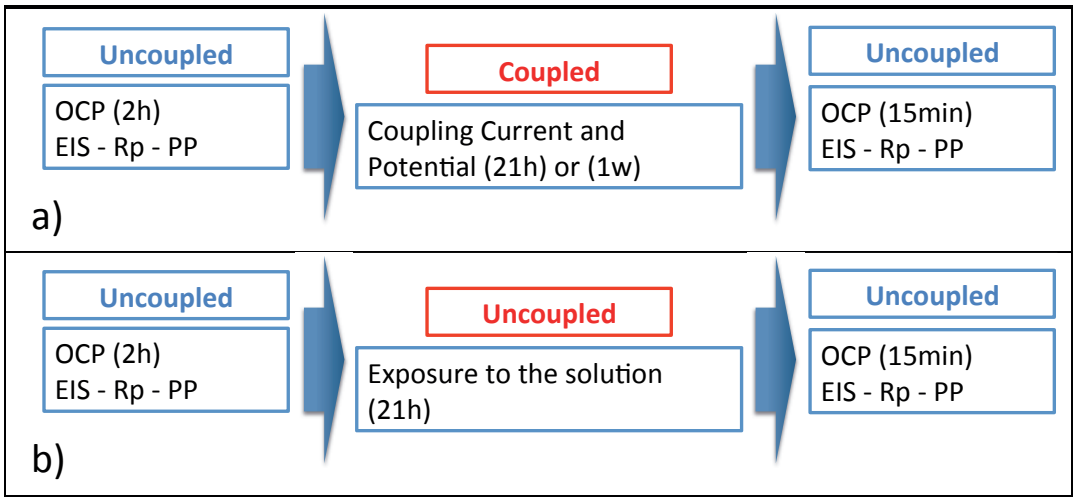

The surfaces of the iron electrodes were chemically analysed by means of X-ray photoemission spectroscopy (XPS). The electrodes were analysed after the complete electrochemical measurement procedure previously described. Before XPS analysis, the surface of the samples was rinsed with deionized water, cleaned with ethanol (p.a.) and dried with oil-free compressed air.

All the measurements were carried out at 23.5 W with a beam size of 100 µ. The analyses were performed on the original surface and on the same spot after 1 min of sputtering with Ar ions accelerated at 2 kV over an area of 2x2 mm. In these conditions, the sputter rate with respect to silicon was 12 nm/min.

4.1.3 Summary of the electrochemical tests performed

Table 26 contains a summary of the tests. Several aspects were taken into account for the evaluation of the study of the tin-iron galvanic coupling:

- The reproducibility of the measures was assessed by carrying out three replications of each measurement of the tin-iron coupling parameters in [0.1] citrate buffer at pH 3.0. The results referring to these tests are identified as T1.
- The effect of the coupling was assessed in the same buffer as T1, but keeping the two electrodes uncoupled for the overall duration of the test. The results referring to these tests are identified as T2.
- Sulphate buffer with the same pH and concentration as in T1 and T2 was used as the electrolyte to study the effect on the tin-iron galvanic coupling of non-complexing anions of tin. The results referring to these tests are identified as T3.

- [0.1] citrate buffer at pH 4.5 was used as the electrolyte to study the effect on the tin-iron galvanic coupling of the pH and the complexing strength of the buffer. The results referring to these tests are identified as T4.
- The assessment of the long-term galvanic coupling between tin and iron was carried out in the same citrate buffer as in T1, but in this case the coupling between tin and iron was maintained over 7 days. The results referring to these tests are identified as T5.

Table 26 Summary of the tests performed

Reference	Buffer	pH	Test conditions	Coupling duration	Properties assessed
T1	**Citrate**	**3.0**	Sn-Fe coupled	21 h	Reproducibility
T2	**Citrate**	**3.0**	Sn-Fe uncoupled	21 h	Co-presence of uncoupled electrodes
T3	**Sulphate**	**3.0**	Sn-Fe coupled	21 h	No complexing environment
T4	**Citrate**	**4.5**	Sn-Fe coupled	21 h	pH/buffer complexing strength
T5	**Citrate**	**3.0**	Sn-Fe coupled	1 week	Long-term coupling

4.2 Results

4.2.1 Electrochemical behaviour of tin and iron before coupling

Figures 44a and 44b show the cathodic and anodic PP curves recorded for tin and iron, respectively. The tests were carried out according to the experimental setup described in **Figure 42a**.

Figure 44 Potentiodynamic polarization curves of tin a) and iron b) recorded before coupling (initial).

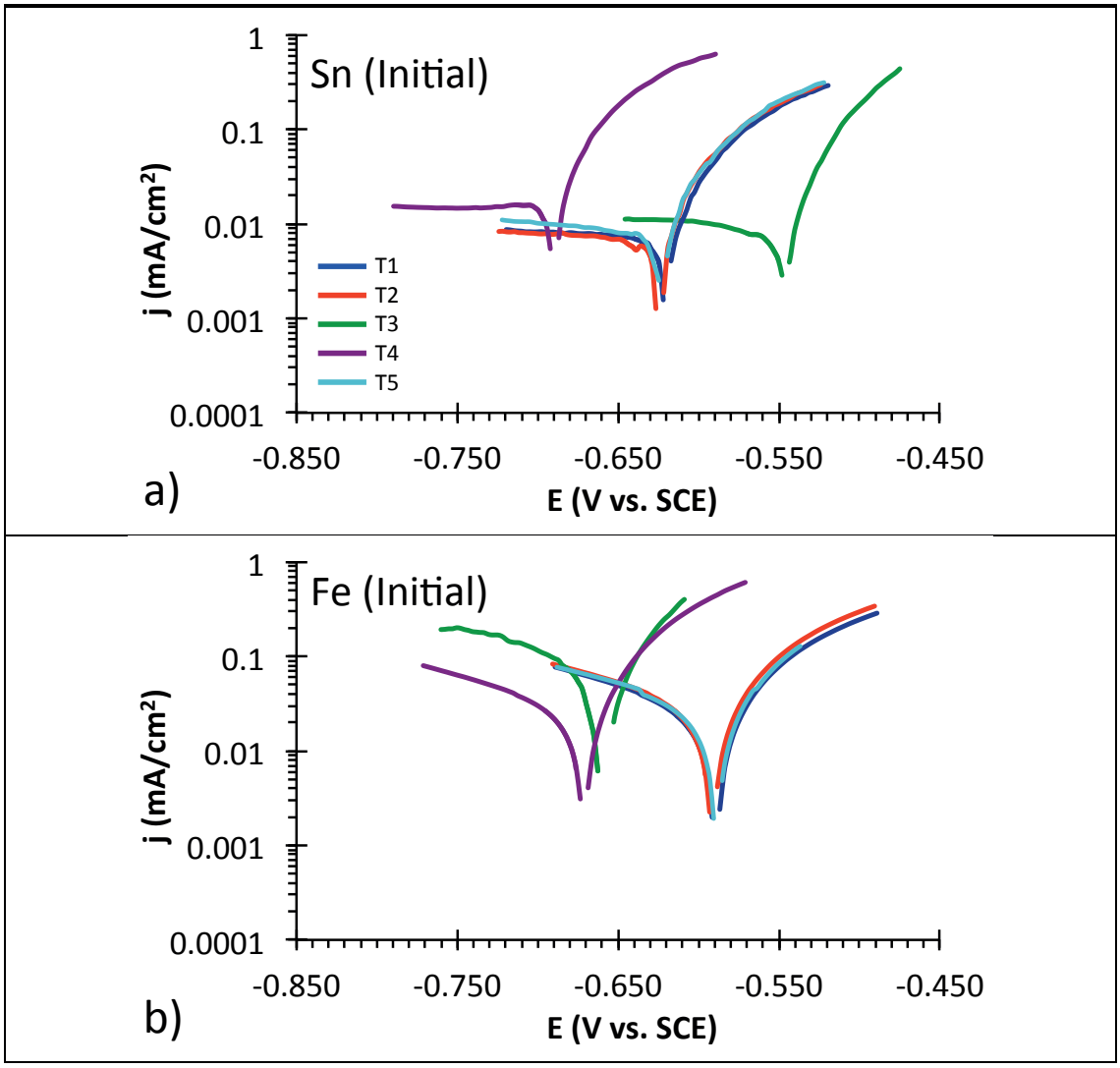

Table 27 lists the OCP values of tin and iron measured after 2 h of de-aeration and the E_{corr} of tin and iron obtained from the PP. As observed in the previous chapter, in this case also, the OCP values correspond with the E_{corr} for both tin and iron.

Table 27 Electrochemical parameters of the tin and iron electrodes measured on the two separate electrodes before coupling. E_{corr}, OCP, j_{corr} of iron (determined from the extrapolation at the E_{corr} of the cathodic Tafel lines) and solution resistance (R_{int}).

pH	Uncoupled (initial)				
	T1	T2	T3	T4	T5
Buffer	Citrate	Citrate	Sulphate	Citrate	Citrate
pH	3.0	3.0	3.0	4.5	3.0
E_{corr} Sn (V vs. SCE)	-0.622	-0.627	-0.548	-0.692	-0.625
E_{corr} Fe (V vs. SCE)	-0.592	-0.593	-0.669	-0.674	-0.591
OCP Sn (V vs. SCE)	-0.623 ± 0.005	-0.624	-0.545	-0.691	-0.622
OCP Fe (V vs. SCE)	-0.588 ± 0.003	-0.591	-0.673	-0.671	-0.588
ΔE_{corr} (V)	-0.030	-0.034	0.121	-0.018	-0.034
ΔE_{OCP} (V)	-0.035	-0.033	0.128	-0.020	-0.034
r_p Sn (Ω cm^2)	1137	1237	889	461	987
r_p Fe (Ω cm^2)	837	681	312	618	710
R_{int} Sn (Ω)	339	322	82	135	303
R_{int} Fe (Ω)	364	327	81	126	350
j_{corr} Fe (μA/cm^2)	25.2	28.8	105.8	26.7	28.8

As previously discussed in Chapter 3, E_{corr} Sn shifts towards negative potential in buffers with a high complexing strength, such as citrate at pH 4.5, while E_{corr} Sn is more anodic in sulphate buffer, in which the anions have less or no complexing strength compared to citrate buffer.

The decrease in E_{corr} Fe for the increase in the pH of citrate buffer is consistent with the cathodic shift of the reversible potential of hydrogen due to an increase in pH of 1.5 points ($E_{rev,H2/H+}$ = -0.0591pH).

The ΔE_{corr} values (E_{corr} Sn – E_{corr} Fe) demonstrate that only in presence of complexing agents for tin ions, such as citrate anions, is the reversal of the tin-iron couple achieved and thus tin becomes cathodic towards the iron.

The PP curves of tin have the typical trend already observed and analysed in Chapter 3. In all the solutions, the concentration of residual oxygen controls the current densities associated with the cathodic plateau of oxygen reduction and thus the corrosion rate of tin. As also demonstrated in Chapter 3, the cathodic currents are very sensitive even to small variations in the residual oxygen concentration. Thus, this leads to the difference in the cathodic plateau currents observed in **Figure 44a**.

Figure 44b shows the PP curves of iron. HER takes place at a higher rate on iron compared to tin. However, the HER still limits the reaction for iron corrosion. **Table**

27 lists the corrosion current densities (j_{corr}) of iron determined by the extrapolation at the E_{corr} Fe of the cathodic Tafel line. As expected, the corrosion current densities of iron are much higher (three orders of magnitude) than those measured for tin in Chapter 3. The reason is that the metal-hydrogen bond is stronger for iron than tin [41] and thus hydrogen atoms are easily adsorbed on the iron surface.

4.2.2 Galvanic coupling between tin and iron

Figure 45a shows the evolution of the coupling currents (j_{coup}) over 21 hours. In citrate buffers, the positive sign of the j_{coup} flowing from iron(+) to tin(-) demonstrates that a small difference in E_{corr} between the two metals (**Table 27**) is enough to generate a flux of electrons from tin to iron. Initially, the j_{coup} grows to a maximum value and later decreases asymptotically to a stable value. As reported in **Table 28,** after 21 h the j_{coup} values measured in citrate at pH 3.0 and 4.5 are 3 $\mu A/cm^2$ and 5 $\mu A/cm^2$, respectively. During this period, the E_{coup} moves from values between tin and iron towards values closer to tin.

Interestingly, the tin-iron couple in T5, in which the coupling was carried out over 7 days, shows similar behaviour to the results of T1 and T4. Furthermore, by comparing the results of T5 with T1 and T3, it is clear that the significant decrease in the coupling currents occurs 21 h after the onset of the galvanic coupling. Afterwards, the coupling currents become stable or undergo a negligible decrease.

In sulphate buffer, the reversal of the corrosion potentials of the tin-iron couple results in the opposite situation. Once coupled, a negative j_{coup} flowing from iron(+) to tin(-) demonstrates the existence of a flux of electrons from iron to tin.

In these conditions, without oxygen but in the absence of complexing agents, the tin coating does not protect the iron; therefore, localized corrosion of iron can take place [15]. Also in this case, the high initial j_{coup} tends to stabilize after 21 h to lower values (-1.6 $\mu A/cm^2$).

It seems that after 21 h, all the systems evolve towards more stable conditions characterized by a lower coupling effect.

Table 28 E_{coup} (V vs. SCE) and j_{coup} ($\mu A/cm^2$) of the tin-iron couple measured immediately after coupling and following the coupling period.

Reference	Buffer	pH	Sn-Fe Coupling			
			E_{coup} (initial)	E_{coup} (final)	j_{coup} (initial)	j_{coup} (final)
T1	**Citrate**	**3.0**	-0.601 ± 0.001	-0.619 ± 0.002	15.0 ± 0.7	3.1 ± 0.6
T2	**Citrate**	**3.0**	No coupling			
T3	**Sulphate**	**3.0**	-0.656	-0.642	-9.8	-1.6
T4	**Citrate**	**4.5**	-0.680	-0.697	12.8	5.4
T5	**Citrate**	**3.0**	-0.603	-0.651	18.8	2.2

Figure 45 Evolution over 21 h of the coupling current j_{coup} ($\mu A/cm^2$) a) and coupling potential E_{coup} (V vs. SCE) b).

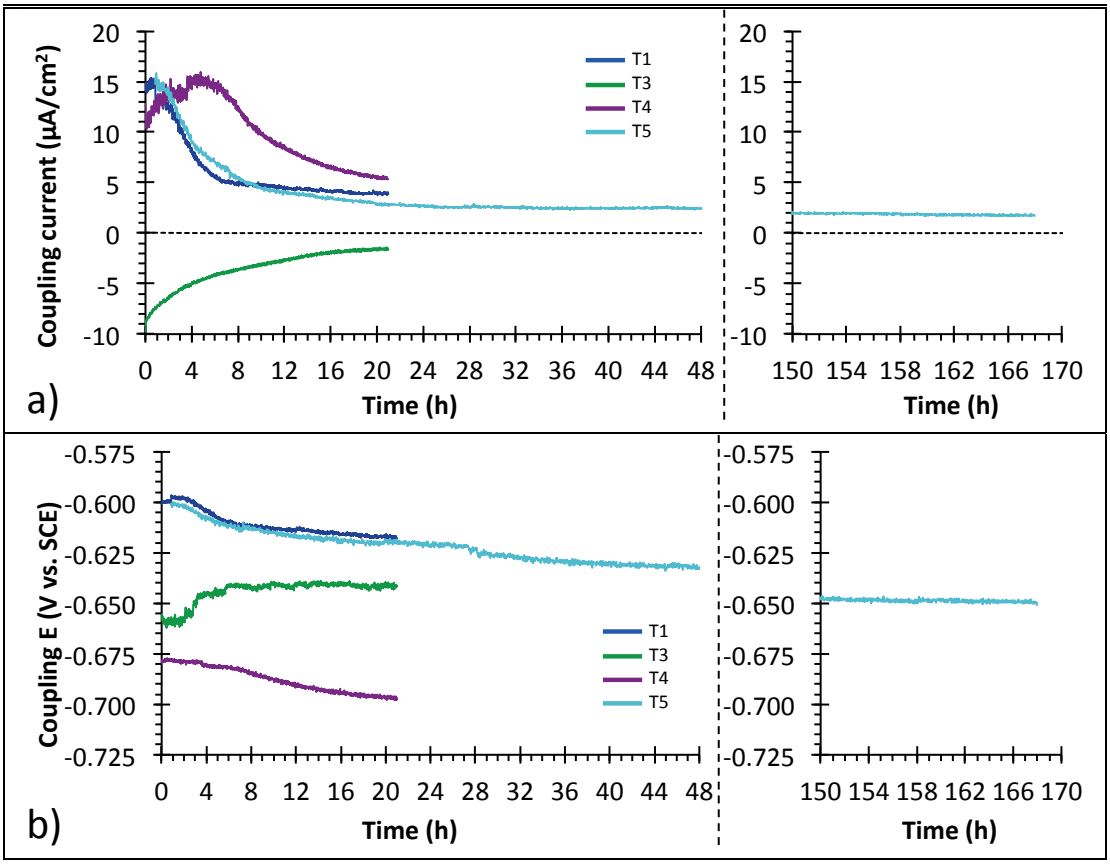

4.2.3 Electrochemical behaviour of tin and iron after coupling and immersion

Figure 46a shows the PP curves recorded for tin after coupling and immersion. The currents associated with the cathodic plateau are similar, regardless of whether the electrodes were coupled or not and independently of the buffer. Thus, this effect is most likely due to the reduction in the oxygen concentration. This is because the cell is continuously de-aerated during the test and thus the oxygen concentration

decreases up to a steady-state value. The coupling with iron seems not to influence the cathodic and anodic mechanisms of tin corrosion. In contrast, for the iron (**Figure 46b**), both cathodic and anodic reactions proceed with slower kinetics.

Figure 46 Potentiodynamic polarization curves of tin a) and iron b) recorded after coupling (final) in citrate and sulphate buffers at pH 3.0 and pH 4.5 and total concentration [0.1].

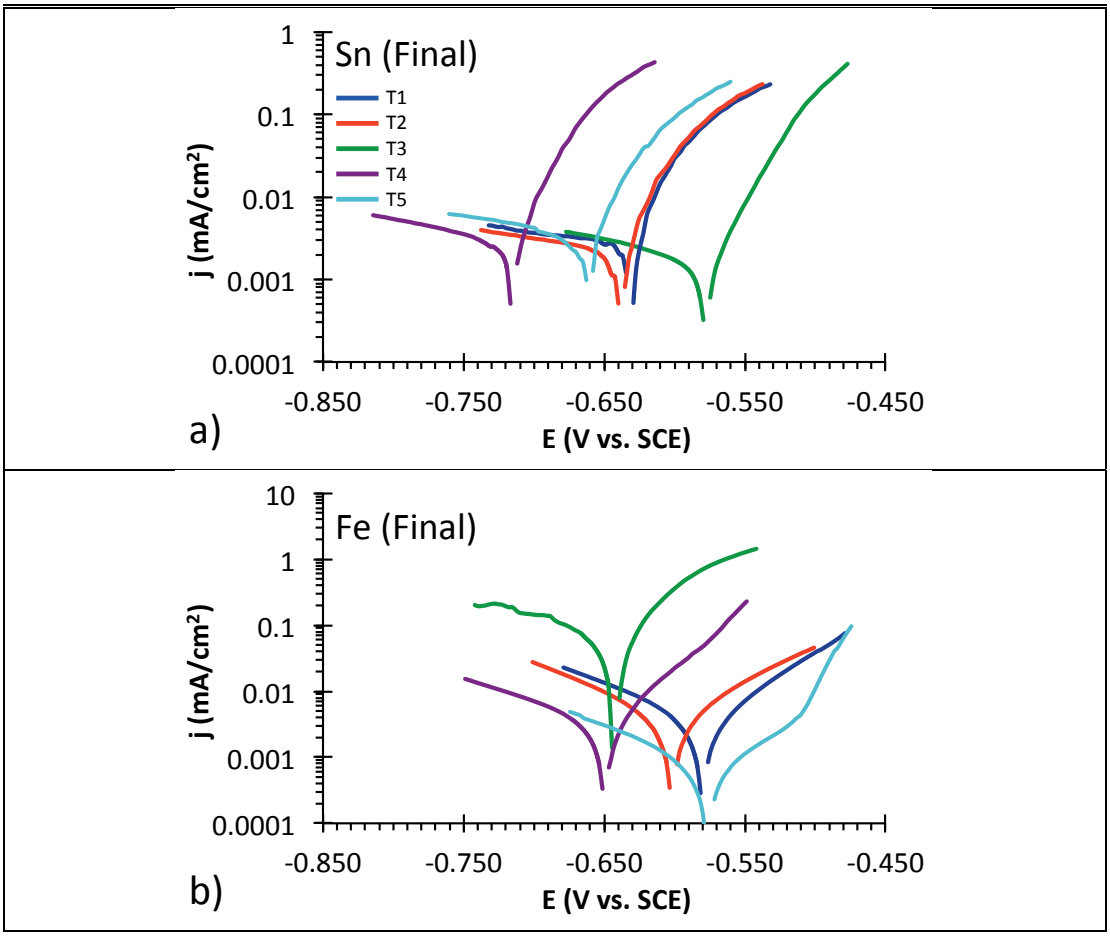

Table 29 shows that, after 21 h of coupling or immersion (T1, T2), the E_{corr} of tin is 20–30 mV more negative compared to the situation before coupling. The E_{corr} of iron decreases only in sulphate and citrate buffers at pH 4.5 (T3, T4). For longer coupling times (T5), the cathodic shift of the E_{corr} of tin is 60 mV, while the E_{corr} of iron undergoes a more limited anodic shift of 14 mV. The increase in ΔE_{corr} observed in all citrate buffers after the coupling is in apparent contrast to the reduction of the j_{coup} reported in **Table 28**. This indicates that the polarization resistance of the electrodes increases during the coupling time interval.

In citrate buffer, the j_{corr} of iron decreases by a factor of 6–10. In sulphate buffer, the j_{corr} of iron decreases only by a factor of 2 because the presence of sulphate

anions enhances iron corrosion by dissolving the protective iron oxide/hydroxide layer [79,80]. Comparing the situation before coupling (**Table 27**) with that after coupling (**Table 29**), it is clear that what changes during the coupling are the polarization resistance of tin and iron, while the internal resistance of the electrolyte remains constant. In citrate buffers, the polarization resistance of iron increases by a factor of 8 after 21 h of coupling (T1, T4) or immersion (T2) and by a factor of 33 after 7 days of coupling (T5). In contrast, in sulphate buffer the polarization resistance of iron remains constant to the initial value.

Table 28 Electrochemical parameters of the tin and iron electrodes measured on the two separate electrodes after coupling. E_{corr}, OCP, j_{corr} of iron (determined from the extrapolation at the E_{corr} of the cathodic Tafel lines) and solution resistance (R_{int}).

pH	Uncoupled (final)				
	T1	T2	T3	T4	T5
Buffer	**Citrate**	**Citrate**	**Sulphate**	**Citrate**	**Citrate**
pH	**3.0**	**3.0**	**3.0**	**4.5**	**3.0**
E_{corr} Sn (V vs. SCE)	-0.634	-0.640	-0.580	-0.717	-0.663
E_{corr} Fe (V vs. SCE)	-0.581	-0.598	-0.644	-0.651	-0.577
OCP Sn (V vs. SCE)	-0.637 ± 0.007	-0.631	-0.579	-0.716	-0.661
OCP Fe (V vs. SCE)	-0.589 ± 0.007	-0.581	-0.641	-0.648	-0.574
ΔE_{corr} (V)	-0.053	-0.042	0.064	-0.066	-0.086
ΔE_{OCP} (V)	-0.048	-0.050	+0.062	-0.068	-0.087
r_p Sn (Ω cm^2)	3016	3573	6243	2812	2643
r_p Fe (Ω cm^2)	4938	4747	275	4736	23517
R_{int} Sn (Ω)	332	321	83	133	294
R_{int} Fe (Ω)	347	338	83	125	313
j_{corr} Fe (μA/cm^2)	4.4	2.7	51.7	3.2	0.7

4.2.4 X-ray photoemission spectroscopy

Figure 47 shows the XPS peaks of carbon, oxygen, tin and iron recorded on the surface of the iron electrodes after the electrochemical measurements. The spectra were acquired after 1 min of Ar sputtering to remove ≈5 nm of superficial contamination. For iron, the peak for the 3p transition was considered because the peak of the main transition ($2p_{3/2}$) overlapped with the peak of the $3p_{3/2}$ transition of tin.

Tin was detected on the surface of all iron samples and also in the case of T2 when the iron electrode was kept immersed in the citrate solution without being coupled with tin.

The energy of the peak $3d_{5/2}$ (486.3 eV) is consistent with the presence of tin oxides, while the metallic peak is not detected. The oxygen peaks at 530 eV and 531.5 eV correspond to the presence of metal oxides and hydroxides, respectively. Carbon is present as a general contaminant and also as carbon bonded with oxygen, most likely as a carboxyl group (288 eV).

The presence of oxidized tin, hydroxide groups and carboxyl groups on the iron surface is evidenced by the precipitation of tin oxides and tin-citrate complexes. This last finding is in agreement with the results proposed by Lamberigts et al. [36].

Table 30 shows the atomic concentration of the elements present on the iron surface. Tin precipitates on the surface of the iron electrode, not only in the presence of galvanic coupling, but also when immersed in citrate solution together with the tin electrode without being coupled with it. Thus, as soon tin ions are available in the solution, precipitation of oxidized tin and tin complexes takes place.

The XPS analysis of the tin electrode surface do not reveal the presence either of hydroxides or carboxylic groups. Thus, this suggests that tin-citrate complexes precipitate only on the iron surface.

Figure 47 XPS spectra recorded on the iron electrodes after the electrochemical measurements.

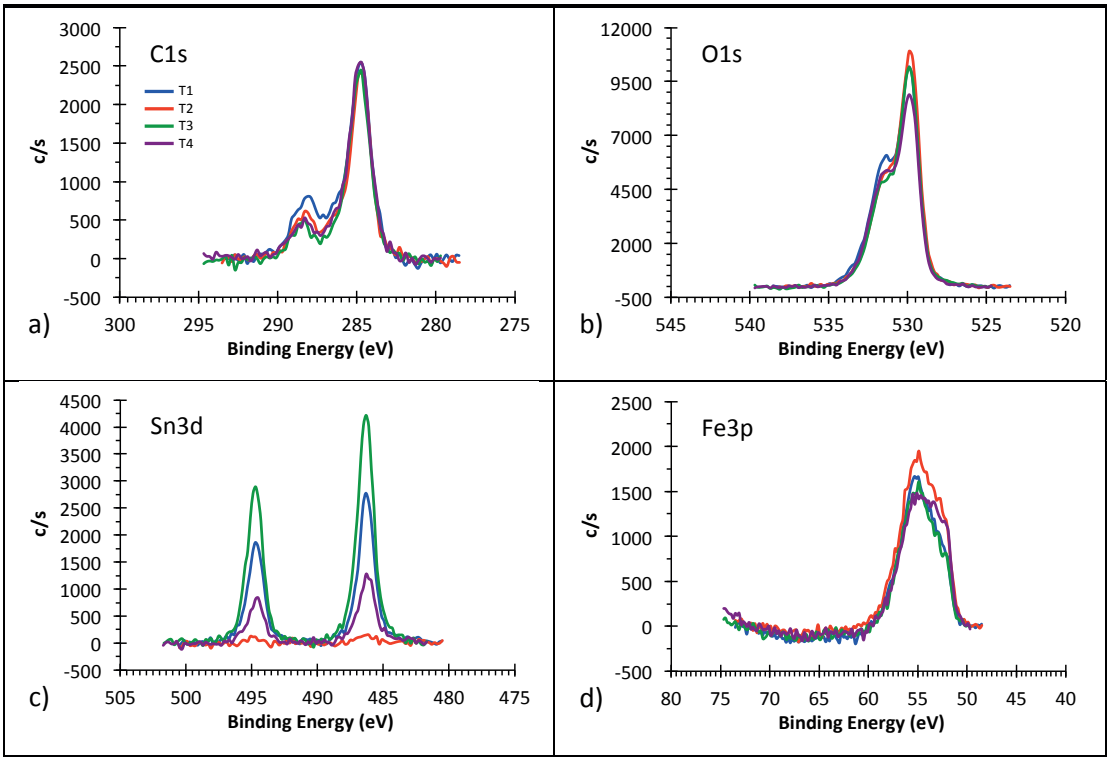

Table 30 Atomic percentage of carbon, oxygen, tin and iron measured by means of XPS on the iron surface after 1 min of sputtering with Ar ions (2 kV 2x2 mm).

Reference	Buffer	pH	Atomic %			
			C	O	Sn	Fe
T1	**Citrate**	**3.0**	27.98	44.44	1.56	26.02
T2	**Citrate**	**3.0**	23.31	45.50	0.05	31.14
T3	**Sulphate**	**3.0**	23.84	46.48	2.79	26.89
T4	**Citrate**	**4.5**	25.76	44.74	0.78	28.72
T5	**Citrate**	**3.0**	NA	NA	NA	NA

4.3 Discussion

4.3.1 Effect of coupling on polarization behaviour

Figure 48 shows the PP curves of tin and iron recorded before and after coupling in [0.1] citrate buffer at pH 3.0. The trend of the PP curves clearly shows that the galvanic coupling reduces the reactivity of iron, while the anodic reactivity of tin does not change. As previously discussed, the decrease in the cathodic plateau currents of tin is consistent with a reduction in oxygen concentration.

The presence of tin oxides and tin-citrate complexes on the iron surface, evidenced through XPS analysis, supports the fact that these precipitates are

responsible for the slowdown in the kinetics of the HER on iron. The same effect was observed by Lambertigts et al. [36], studying the effect of coupling on steel.

In contrast, the absence of precipitates on the tin surface after the galvanic coupling justifies why the anodic kinetics do not change.

Figure 48 Potentiodynamic polarization curves of tin and iron recorded before (initial) and after coupling (final), in citrate (T1) a) and sulphate (T3) b) buffers [0.1] at pH 3.0.

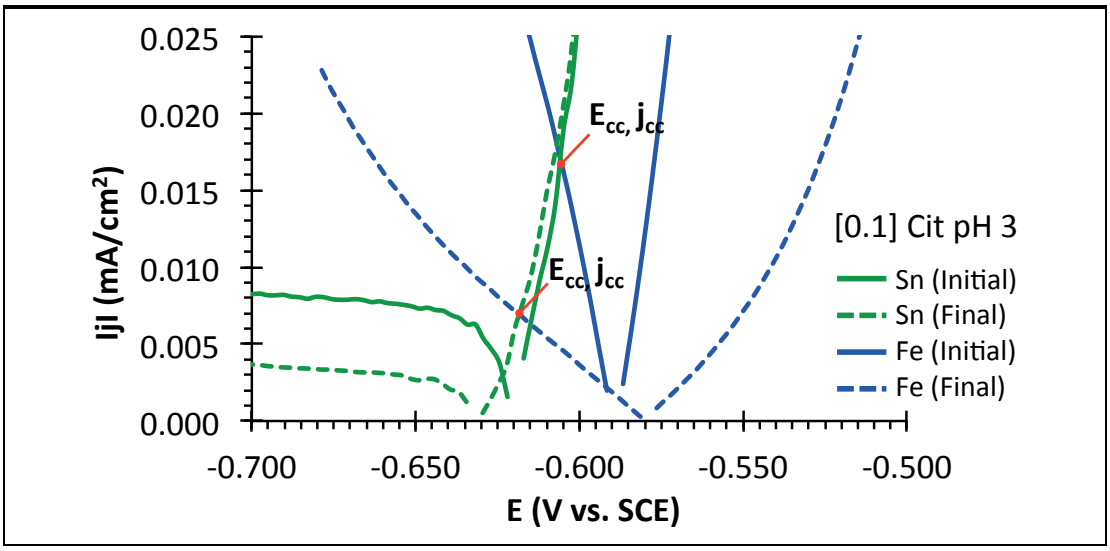

From **Table 31** it is evident that the short circuit potentials (E_{cc}) and the short circuit current densities (j_{cc}) extracted from the PP (**Figure 48**) correspond to the coupling potentials (E_{coup}) and coupling current densities (j_{coup}) measured. This suggests that the internal resistance of the electrolyte is negligible compared to the polarization resistance of the single electrodes. Therefore, the galvanic coupling current is linked only to the cathodic kinetics of iron and anodic kinetics of tin.

The values of the polarization resistance of tin and iron reported in **Table 33** indicate that these values are time dependent. The extremely high polarization resistance observed for iron after one week of coupling is consistent with the precipitation mechanism previously described. For tin also, the polarization resistance changes with time, but it seems to reach a stationary value after one day of exposure to the electrolyte.

Table 31 Comparison between polarization resistances of tin and iron before and after coupling and comparison of the short circuit potential (E_{cc}) and short circuit current densities (j_{cc}) extracted from the PP curves reported in **Figure 48** .The measured coupling potential (E_{coup}) and coupling current densities (j_{coup}) are also included.

Parameter	Measurement point	T1	T4	T5
		Citrate	Citrate	Citrate
		pH 3.0	pH 4.5	pH 3.0
r_p Sn Ω cm^2	Initial	1137	461	987
	Final	3016	2812	2643
r_p Fe Ω cm^2	Initial	837	618	710
	Final	3016	4736	23517
E_{coup} (V vs. SCE)	Initial	-0.601 ± 0.001	-0.680	-0.603
	Final	-0.619 ± 0.002	-0.697	-0.651
E_{cc} (V vs. SCE)	Initial	-0.606	-0.684	-0.608
	Final	-0.618	-0.701	-0.651
j_{coup} (µA/cm^2)	Initial	15.0 ± 0.7	12.8	18.8
	Final	3.1 ± 0.6	5.4	2.2
j_{cc} (µA/cm^2)	Initial	16.0	16	20.5
	Final	6	7	3.4

4.3.2 Modelling of coupling currents

Figure 49 shows the equivalent circuits of tin-iron corrosion cells generated by galvanic coupling. The representation is done according to the convention described by Landolt [41], in which R_{ext} is the external resistance due to the electronic conductors (Ω), R_{int} is the ohmic resistance of the electrolyte between the two electrodes (Ω) and R_p Sn and R_p Fe are the polarization resistances of the two coupled metals (Ω). R_{ext} is constant and negligible during the coupling test, while the other parameters R_{int} and R_p may evolve during the coupling.

Figure 49 shows that in the presence of a complexing environment in which E_{corr} Sn is lower than E_{corr} Fe, electrons flow from tin to iron. Thus, the corrosion rate of tin increases as soon tin is in contact with iron. The overall corrosion current responsible for tin dissolution is given by the sum of the corrosion current of tin in the electrolyte (j_{corr}), as determined in Chapter 3, and the coupling current resulting from the galvanic coupling with iron (j_{coup}).

Figure 49 Electrical equivalent circuits of corrosion cell in [0.1] Citrate buffer pH 3.0 R_{int} internal resistance of the electrolyte between tin and iron electrodes, R_{ext} resistance of the electronic conductors of the circuit, R_p polarization resistance of the two electrodes.

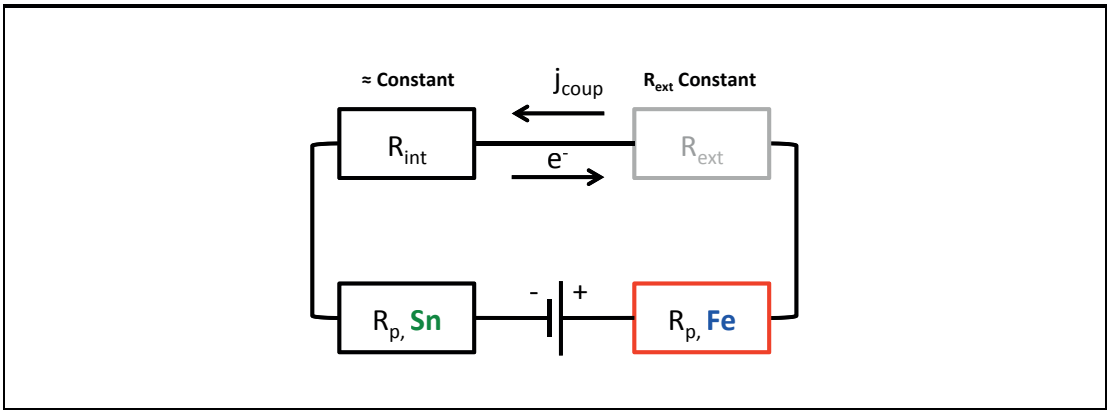

According to the literature [41], the coupling current J_{coup} (A) of the previously described corrosion cell is given by **Eq. 15**:

$$J_{coup} = \frac{\Delta E_{corr}}{R_p\,Sn + R_p Fe + R_{int} + R_{ext}} \qquad (15)$$

Considering **Eq. 15**, disregarding R_{ext} and introducing the areas of the two coupled electrodes, the coupling current density determining the increase of tin dissolution can be calculated using **Eq. 16**:

$$j_{coup} = \frac{\Delta E_{corr}}{\frac{r_p\,Sn\,(t)}{A_{Sn}} + \frac{r_p Fe\,(t)}{A_{Fe}} + R_{int}} \frac{1}{A_{Sn}} \qquad (16)$$

where r_p (t) are the time-dependent polarization resistance of Sn and Fe, expressed in Ω cm^2, R_{int} is the resistance of the electrolyte (Ω) and A_{Sn} and A_{Fe} are the areas of Sn and Fe expressed in cm^2.

The fact that the coupling current (j_{coup}) and the short circuit currents (j_{cc}) are extremely close to each other (**Table 31**) suggests that the R_{int} term of **Eq. 16** can be disregarded with respect to the polarization resistance of tin and iron.

Moreover, considering that the resistance of electrolyte can also be calculated by the solution resistivity (ρ_e) according to **Eq. 17**, it is clear that when the distance between tin and iron electrodes is very small ($d_{Sn\text{-}Fe}$), the R_{int} terms can also be disregarded.

$$R_{int} = \rho_e \frac{d_{Sn-Fe}}{\frac{(A_{Sn}+A_{Fe})}{2}} \quad (17)$$

Table 32 shows the comparison between the directly measured coupling current densities for tin and the values calculated according to **Equation 16** and the experimental parameters reported in **Tables 27 and 29.** The good correlation between the measured values and the calculated values suggest that by means of **Eq. 16** it is possible determine the kinetics of tin dissolution from tinplate once the tin-iron galvanic coupling takes place.

Kamm et al. [24] demonstrated that the rate of tin dissolution is similar, independently of the $FeSn_2$ coverage, for tinplated samples coated with homogeneous and low porous tin layers. This condition was valid before visible areas of $FeSn_2$ were exposed to the electrolyte. The degree of coverage of the $FeSn_2$ alloy plays a key role once this phase is exposed. If the coverage is close to 100%, the rate of Sn release is faster than that of pure Sn, but slower than when Sn is coupled with Fe [48]. A low coverage of the $FeSn_2$ alloy leads to a marked increase in tin dissolution [24,48].

Table 32 Comparison between the coupling current density measured and the values calculated by means of **Eq. 16**.

Reference	Buffer	Coupling time	j_{coup} (μA/cm^2)	
			Measured	Calculated (Eq. 2)
T1	**Citrate pH 3.0 [0.1]**	**Initial**	15.0 ± 0.7	15.6
		Final	3.1 ± 0.6	5.8
T4	**Citrate pH 4.5 [0.1]**	**Initial**	12.8	16.9
		Final	5.4	8.9
T5	**Citrate pH 3.0 [0.1]**	**Initial**	18.8	17.6
		Final	2.2	3.3

4.3.3 Effect of porosity on tinplate corrosion lifetime

We can now apply **Eq. 16** to the case of tinplate with different porosities of the Sn layer. The galvanic coupling occurs between the top and the bottom of the tin coating due to porosity or when the tin layer is not homogeneously dissolved. The calculations were done for the [0.1] citrate buffer systems at pH 3.0 and 4.5 using

Eq. 16 considering the equivalent circuit representing the typical tin-iron couple polarity (**Figure 49**).

The values of the polarization resistance of tin and iron were taken from **Table 31**, while the solution resistance R_{int} was disregarded since the tin-iron distance is at maximum 1 µm. Thus, according to **Eq. 17**, the R_{int} term becomes negligible compared to the polarization resistances of the two metals. The resistance of the solution in the porosities can also be disregarded because the common aspect ratio of the porosities is 1:1. All the other parameters used for the calculation are listed in **Table 33**.

Table 33 Input parameters for the calculation of j_{coup} according to **Eq. 16**

Parameter	Value	Units
Can volume	0.4	dm^3
Internal surface	≈320	cm^2
Thickness of pure tin layer	1	µm
Internal surface in contact with the electrolyte	320	cm^2
Citrate buffer concentration	0.1	mol/L
Citrate buffer pH	3.0, 4.5	-
Porosity of the tin layer	0.1, 0.2, 0.3, 0.4, 0.5, 1	%

Figure 50 shows the influence of the percentage of exposed iron on the corrosion rate of tin due to galvanic coupling. From **Figure 50a** it is clear that already exposed areas of iron below 1% are critical for tin dissolution. Interestingly, after this percentage, the coupling current densities responsible for tin dissolution become two orders of magnitude higher than the corrosion current densities measured in Chapter 3 for tin in the same electrolytes. Thus, clearly the homogeneity of the pure tin layer is fundamental for the lifetime of tinplate.

Figure 50b shows that moving from 0.1% to 1% of iron exposure, the expected lifetime of the Sn layer decreases by a factor of 10. These results are in agreement with Britton et al. [13], who reported that tin dissolution due to galvanic coupling with iron increases dramatically when the exposed area of iron exceeds 1% of the total area.

Thus, **Eq. 10** seems to be a reliable tool for estimating the relevance of porosity and tin-iron galvanic coupling on the lifetime of tinplate in food cans.

Figure 50 Relation between the % of exposed iron in the tin-iron galvanic coupling and the corrosion rate of tin a) and the lifetime of a pure tin layer 1 µm thick covering the entire internal surface of a can b).

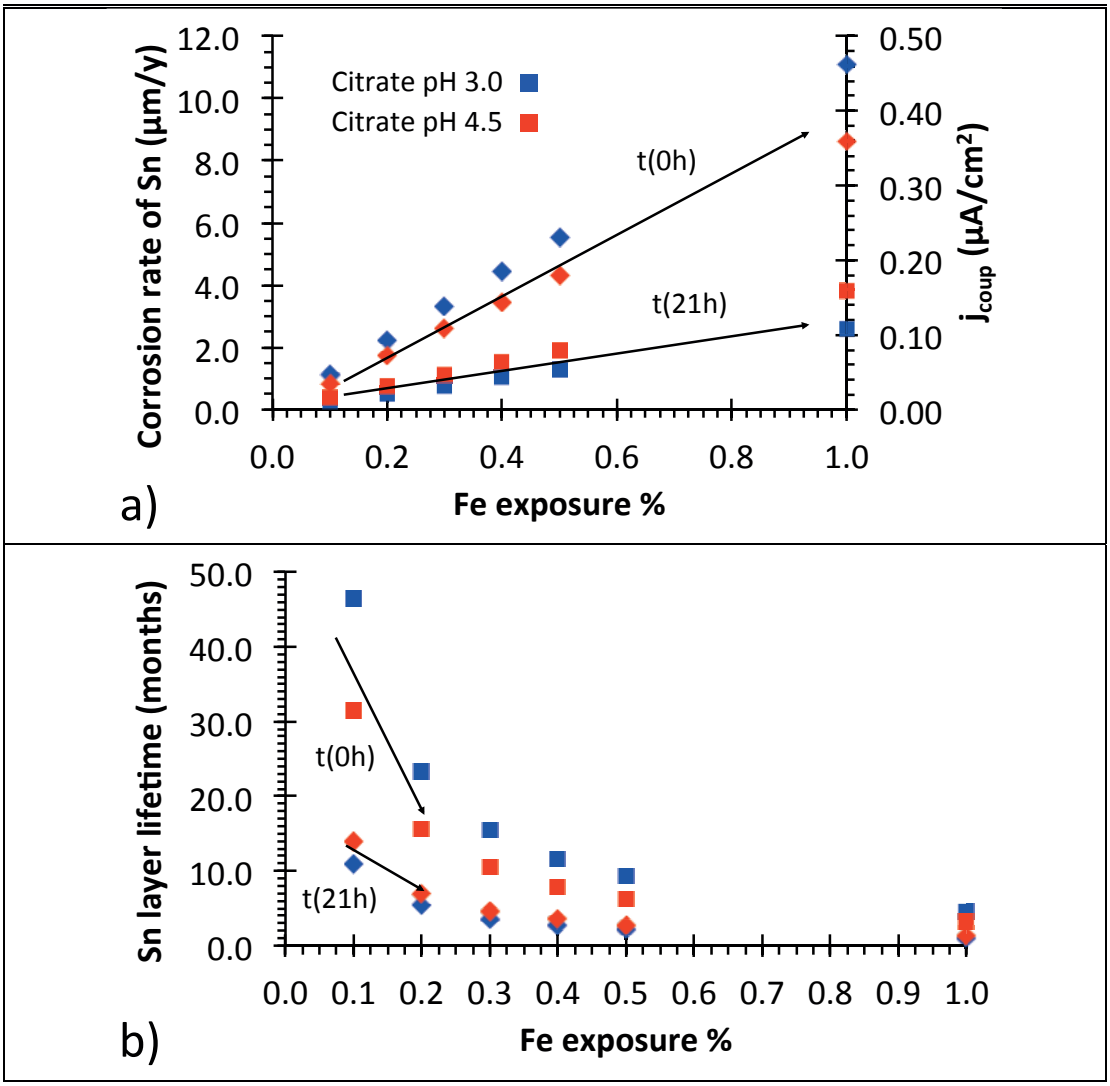

4.4 Conclusions

This study highlighted that the galvanic coupling between tin and iron does not influence the anodic and cathodic kinetics of tin corrosion, while those of iron are inhibited by the presence of tin ions in solution. The presence of the complexing agents of tin ions determines the polarity of the tin-iron couple and the mechanism governing the galvanic coupling. Thus:

- In complexing media, the corrosion potential of tin is lower compared to that of iron. A galvanic coupling current flowing from tin to iron determines the enhancement of tin dissolution compared to simple acid corrosion.
- The kinetics of tin-iron galvanic coupling is determined by the kinetics of the anodic dissolution of tin and by the cathodic kinetics of the HER on iron.
- Precipitation of Sn complexes/oxides on the iron surface inhibits the cathodic kinetic of the HER on iron. This self-healing behaviour of tinplate allows the reduction of the coupling current flowing from iron to tin.
- The galvanic coupling current responsible for the increase in tin dissolution due to the galvanic coupling between tin and iron can be calculated by knowing the tin-iron area ratios, the corrosion potentials and the polarization resistances of tin and iron.

5 Modelling of tinplate corrosion

In Chapter 1, **Figure 7** showed the trend in tin release as a function of storage time, which is commonly used to describe tinplate corrosion in acidic foods [4,5,32,34]. This trend is based on empirical studies and was explained by Mannheim et al. [30] considering three stages, as follows:

1st stage: rapid tin dissolution due to the reduction in residual oxygen and the oxidant species present in food and described in Chapter 3.

2nd stage: the longest stage, characterized by slow tin dissolution at an almost constant rate.

3rd stage: tin dissolution increases exponentially due to the exposure of large areas of base steel available for the HER.

The proposed explanation is purely phenomenological and has some shortcomings. For example, the claim that during the 2nd stage the release of tin is almost constant while the area of exposed base steel increases does not match the findings of previous works [8-12]. In particular, Britton et al. [10] reported that the corrosion rate of tin increases when the exposed area of base steel exceeds 1% of the total tinplate surface. Furthermore, roughness aspects are not considered.

In the next paragraphs a mechanistic description of tinplate corrosion based on the outcomes of this work is proposed.

5.1 Tinplate corrosion model

5.1.1 Phenomenology

Figure 51 shows the realistic representation of the structure of tinplate as assessed in Chapter 2. The two regions relevant for the corrosion behaviour of tinplate are the tin layer and the interface.

Figure 51 Realistic representation of the tinplate structure.

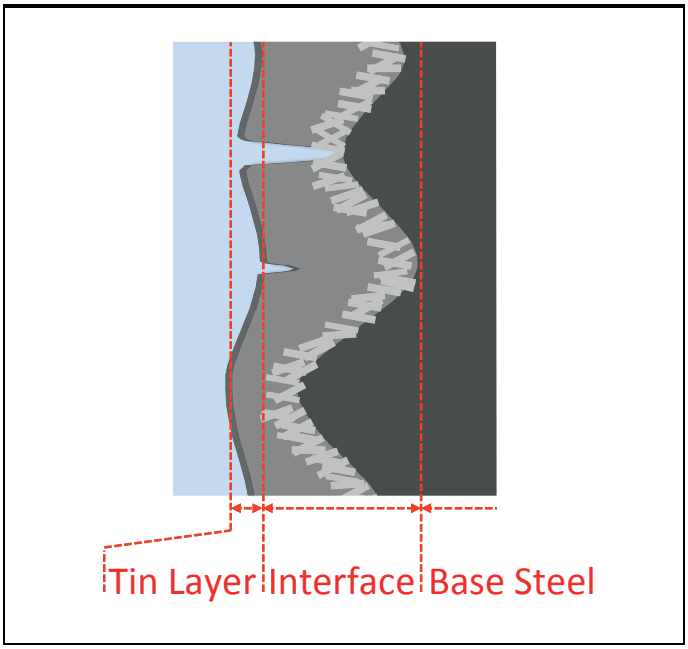

The tin guarantees the corrosion resistance of tinplate and thus the overall lifetime of tinplate is dependent on the corrosion rate of tin. Based on the outcomes of Chapters 3 and 4, the overall corrosion current responsible for tin dissolution can be calculated according to **Eq. 18** considering the contribution of the currents of the ORR and the HER taking place on tin and the galvanic coupling current flowing from the base steel to tin.

$$j_{corr}\ Sn = j_{l,ORR}\ Sn + j_{c,HER}\ Sn + j_{coup}\ Sn/Base\ Steel \qquad (18)$$

To model the corrosion behaviour of tinplate and predict its durability, **Eq. 18** needs to be combined with the material structure information determined in Chapter 2. The modelling was carried out taking into account the following assumptions:

- The effect of porosity is negligible during the corrosion of the tin layer.
- The currents of galvanic coupling between tin and base steel are calculated considering the coupling between tin and iron as studied in Chapter 4.
- The cathodic kinetics of iron are time dependent; they reduces with time due to the deposition of tin oxides/complexes on the iron surface. Thus, for the modelling it is necessary to specify the times to which the polarization resistance of iron refers.

- The tin-iron alloy is considered inert to corrosion. Thus, it affects corrosion by partially masking the iron surface.
- Oxygen content reduces to zero within a certain time due to its reactivity with tin.

5.1.2 The tin corrosion phase

In the absence of porosity, the corrosion current density responsible for the dissolution of the tin layer depends only on the ORR and the HER, while the contribution of galvanic coupling can be disregarded. Based on the outcomes of Chapter 3, the currents of the ORR and the HER can be calculated by means of **Eq. 19** and **Eq. 20**, respectively.

$$j_{c,ORR}Sn = j_{l,ORR} = nFD_{O_2}\frac{c_{O_2,b}}{\delta} \quad (19)$$

$$j_{c,HER}Sn = j_{0,HER}\ exp\left(-\frac{E_{corr,Sn}-E_{rev,HER}}{\beta_{c,HER}}\right) \quad (20)$$

The modelling of this phase is now carried out considering a can made of tinplate material type D 2.8/11.2, previously characterized in Chapter 2 (Tinplate E). For this specific material, the AES analysis highlighted a minimum tin layer thickness of 432 nm and a width of interface of 963 nm. For the modelling, the internal surface of a can (≈320 cm^2) was considered to be entirely in contact with 0.4 dm^3 of [0.1] citrate buffer at pH 3.0. **Table 34** lists the parameters used for the calculation of the limiting current for the ORR ($j_{l,ORR}$) according to **Eq. 19**. The initial concentration of oxygen was chosen based on the oxygen saturation values of pure water at different temperatures. The thickness of diffusion layer δ for the ORR under static conditions was determined using **Eq. 19** by measuring the j_l for the ORR on tin in citrate buffer solution saturated in oxygen at 25 °C. In these conditions, the measured $j_{l,ORR}$ is -18 ± 5 µA/cm^2, while the diffusion coefficient (D_{O2}) and the solubility of oxygen in fresh water are 2.51x10^{-5} cm^2/s and 8.3 mg/L, respectively [41]. Thus, the resulting thickness of the diffusion layer δ is 0.14 cm.

Table 34 Input parameters for the calculation of $j_{l,ORR}$ according to **Eq. 19**

Parameter	Value	Units
D_{O2}	2.51×10^{-5}	cm^2/s
v	8.93×10^{-3}	cm^2/s
n	4	-
F	96485	C/mol
δ	0.14	cm
c_{O2}	Input parameter	mol/cm^3

The corrosion current due to the cathodic reaction of the HER was determined by means of the Volmer–Butler equation (**Eq. 20**). The parameters used for the calculation of the cathodic current of the HER are listed in **Table 35**. For the modelling, the $j_{0,HER}$ calculated in Chapter 3 for the HER on tin in [0.1] citrate buffer at pH 3 was used. A b_c of 100 mV/dec can be used for the calculation independently of the buffer system. $E_{rev,\ HER}$ and $E_{corr,\ Sn}$ are the input parameters for the calculation of $j_{c,\ HER}$. The $E_{rev,\ HER}$ for a given pH is calculated by means of Nernst's equation, while $E_{corr,\ Sn}$ is a measured value after 2 h of stabilization.

Table 35 Input parameters for the calculation of $j_{c,HER}$ according to **Eq. 20**

Parameter	Value	Units
$j_{0,HER}$	8×10^{-8}	mA/cm^2
$E_{rev,\ HER}$	-0.421	V vs. SCE
$E_{corr,\ Sn}$	-0.625	V vs. SCE
$b_{c,\ HER}$	100	mV/dec

Considering the previous assumptions, it is now possible to model the first stage of the corrosion of tinplate. In this stage, the dissolution of the tin layer occurs as a result of the ORR and the HER. The ORR takes place as long as oxygen is present; afterwards the dissolution of tin is only due to the HER.

Figure 52 shows the evolution over the first 30 h of the modelled $j_{l,ORR}$, $j_{c,HER}$ and $j_{corr,Sn}$ for an initial oxygen concentration of 3.4 ppm (water oxygen saturation at the typical filling temperature of 80 °C). Clearly, the ORR makes an important contribution to the overall $j_{corr,Sn}$ only during the first hour or day after the filling of the can. Afterwards, once the oxygen concentration drops to zero, the rate of tin corrosion is determined by the rate of the HER.

Although this first stage lasts only a short period, **Table 36** shows that the rapid corrosion of tin due to the ORR can markedly affect the lifetime of a can. The citrate

buffer saturated in oxygen at 0 °C consumes 43% of the thickness of the Sn layer. If the oxygen content is lowered to 1 ppm, the initial consumption of the Sn layer drops to 3%. The second stage, characterized by the dissolution of the residual tin due to the HER, is the longest and determines the lifetime of a can. **Table 36** also shows the times needed to dissolve the residual tin layer and reach the interface after the consumption of the initial oxygen concentration.

Figure 52 Contribution of the HER and the ORR to the overall corrosion current responsible for the dissolution of tin from the interface of Tinplate E in citrate buffer at pH 3.0 and a total concentration of [0.1] containing initially 3.4 ppm of oxygen.

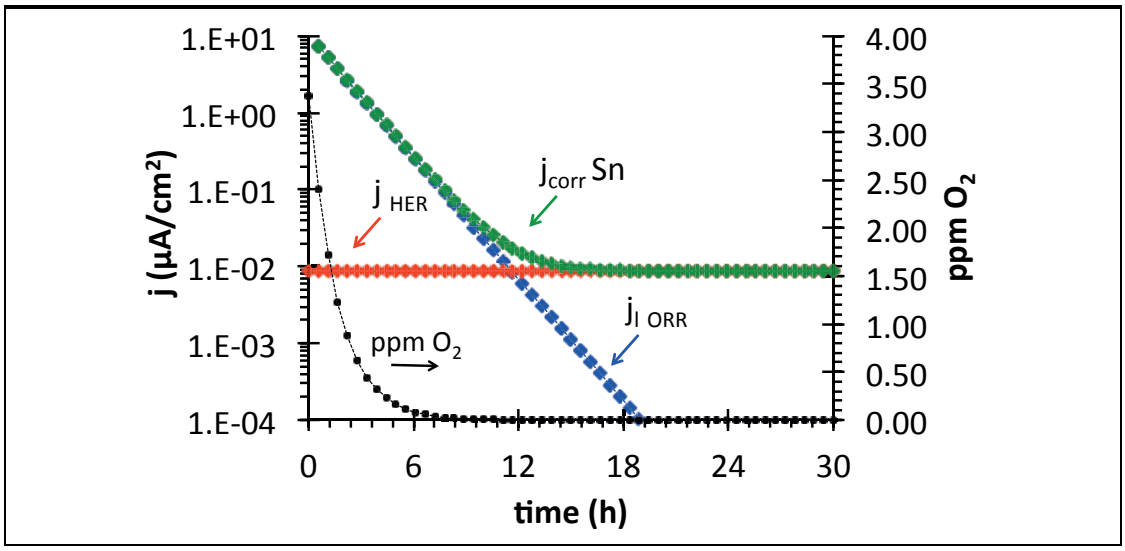

Table 36 Influence of the initial concentration of oxygen on the lifetime of tinplate cans type (D 2.8/11.2)

Initial O_2 concentration (ppm)	Thinning of Sn layer due to O_2 (nm)	Residual Sn layer thickness (nm)	Time needed to dissolve the residual Sn layer (d)
14.6	186	246	388
9.1	116	316	499
6.4	82	350	553
4.7	60	372	587
3.4	43	389	614
1	13	419	662
0	0	432	682

5.1.3 The interface corrosion phase

The dissolution of tin induced by the galvanic coupling between tin and base steel (j_{coup}Sn/Base steel) needs to be considered as soon as the interface is approached. Based on the outcomes of Chapter 4, the contribution of galvanic coupling to the overall corrosion current density can be calculated by means of **Eq. 21**:

$$j_{coup}\ Sn/Base\ Steel\ = \frac{\Delta E_{corr}}{\frac{r_p\ Sn}{A_{Sn}} + \frac{r_p Base\ steel}{A_{Base\ Steel}\ \theta_{FeSn_2}} + R_{int}} \frac{1}{A_{Sn}} \quad (21)$$

In addition to the kinetic parameters of tin-iron galvanic coupling, **Eq. 21** also requires the material parameters describing the evolution of the tin/iron atomic ratio as a function of depth and the degree of coverage of the FeSn2 alloy.

The modelling of j_{coup}Sn/base steel was undertaken considering the tin/iron ratio as a function of depth as measured by AES depth profile analysis (**Figure 21**, area 1). For the modelling, different possible coverage degrees reported in the literature were considered. Gabe et al. [11,15] found a coverage degree comprising between 50% and 99% for electroplated tinplate and between 85% and 100% for tinplate produced by hot dipping.

Table 32 reports the parameters used in **Eq. 21** to calculate the tin-iron galvanic coupling current. The values of the difference in corrosion potential (ΔE_{corr}) and the polarization resistance (r_p) are those measured in Chapter 4 after 7 days of coupling. As previously discussed in Chapter 4, the effect of the solution resistance (R_{int}) can be disregarded.

Table 32 Input parameters for the calculation of j_{coup} according to **Equation 21.**
*From AES depth profiles; At% changes with the considered depth

Parameter	Value	Units
ΔE_{corr}	0.087	V
$r_p Sn$	2643	Ω cm^2
$r_p Fe$	23517	Ω cm^2
A_{Sn}	Sn At%* x total surface	cm^2
A_{Fe}	Fe At%* x total surface x θ_{FeSn2}	cm^2
θ_{FeSn2}	Input parameter	%

Figure 53a shows the evolution of the modelled $j_{c,HER}$, $j_{coup,Sn\text{-}Fe}$ and $j_{corr,Sn}$ once the interface is reached and the $FeSn_2$ alloy has 95% coverage. This high alloy coverage

slows down the dissolution of tin due to galvanic coupling. **Figure 53b** shows the importance of the $FeSn_2$ alloy coverage for the lifetime of the cans once the interface is reached.

Figure 53 Contribution of the HER and Sn-Fe galvanic coupling to the overall corrosion current responsible for the dissolution of tin from the interface of Tinplate E in citrate buffer at pH 3.0 and a total concentration of [0.1]. Time 0 is the corrosion time at which the interface is reached.

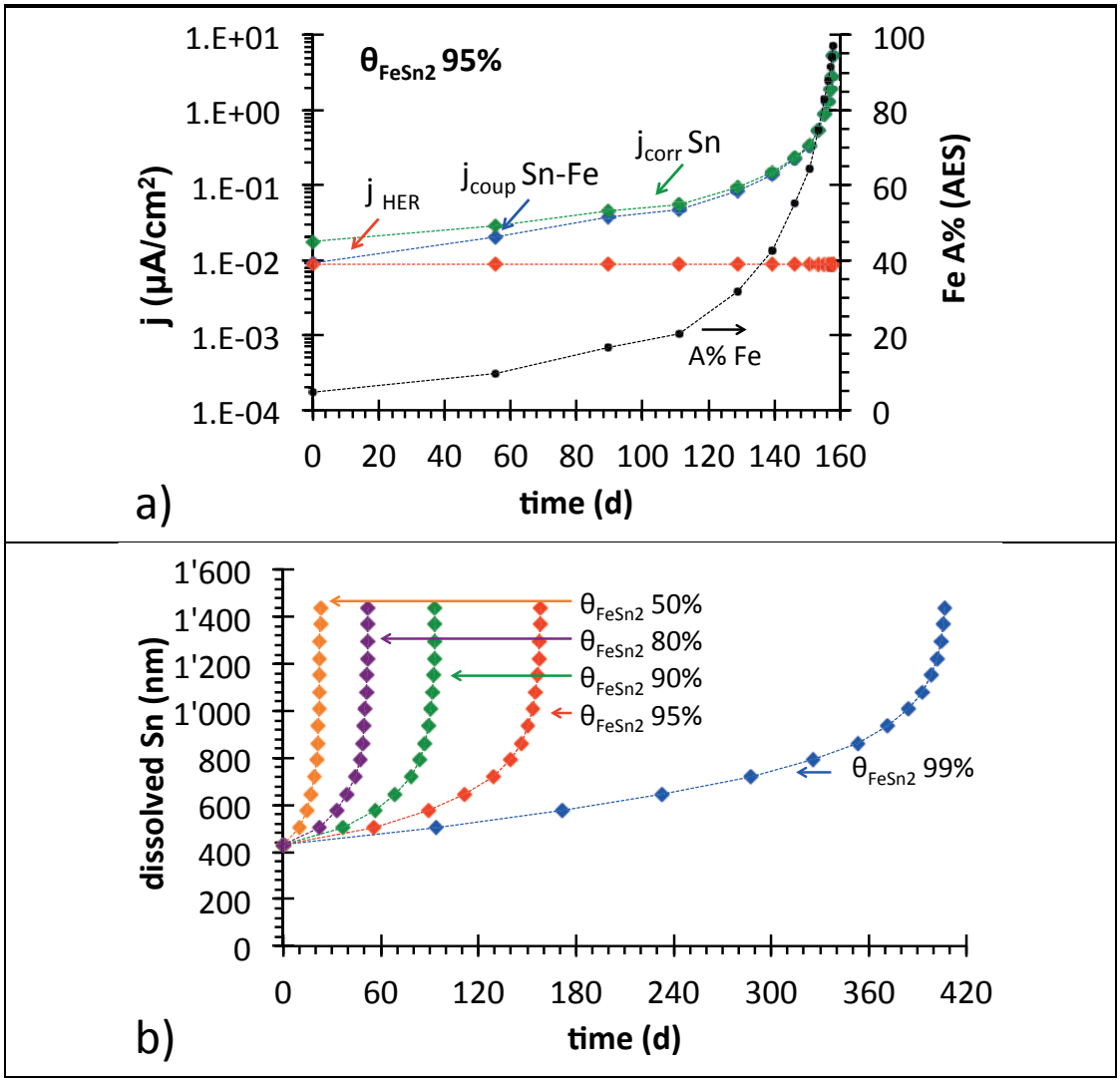

5.2 Application to cans

5.2.1 Modelling of the lifetime of cans containing model solutions

Figure 54 shows the combination of the three different stages of tinplate corrosion previously modelled. The modelled curve shows the dissolution of tin from a plain tinplate can type D 2.8/11.2 completely filled at 80 °C (3.4 ppm O_2), with 0.4 dm^3 of [0.1] citrate buffer at pH 3.0. The alloy coverage was assumed to be equal to 95%.

The modelled curve of tin dissolution follows the same trend as the empirical curve of tin dissolution reported in the literature [4,34] and schematized in **Figure 7** in Chapter 1. The good correlation between the trend of the modelled and empirical curves supports the validity of the model. Furthermore, the modelled lifetime is consistent with that observed by Kamm et al. [31] during the pack test of cans made of the same type of tinplate (E 11.2/11.2) filled with citrate buffer at pH 3.0.

The curve reported in **Figure 54b** indicates that once the interface is reached, a relevant HER takes place. This leads to rapid swelling of the can and later to bursting. Thus, swelling of a can should be interpreted as a signal that most of the tin layer has been dissolved and the interface is exposed. In these conditions the remaining lifetime is limited.

Figure 54 Modelled curves representing the dissolution of tin from tinplate as a function of time a) and the amount of hydrogen released due to Sn corrosion b). Input parameters for modelling: complete filling with [0.1] citrate buffer at pH 3.0, initial oxygen concentration 3.4 ppm, $FeSn_2$ coverage 95% and tinplate structure represented by the AES depth profile of Tinplate E on area 1.

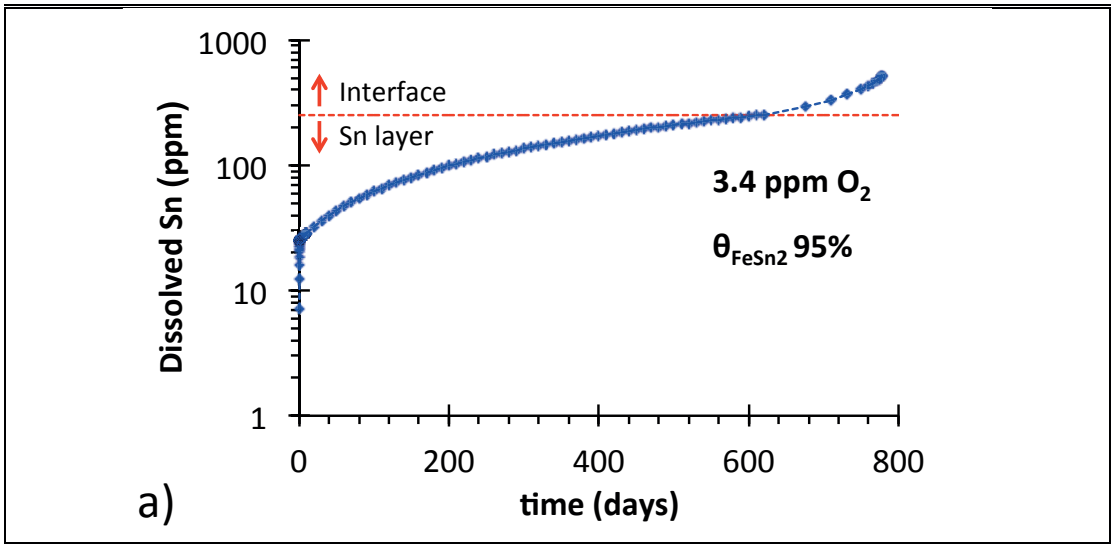

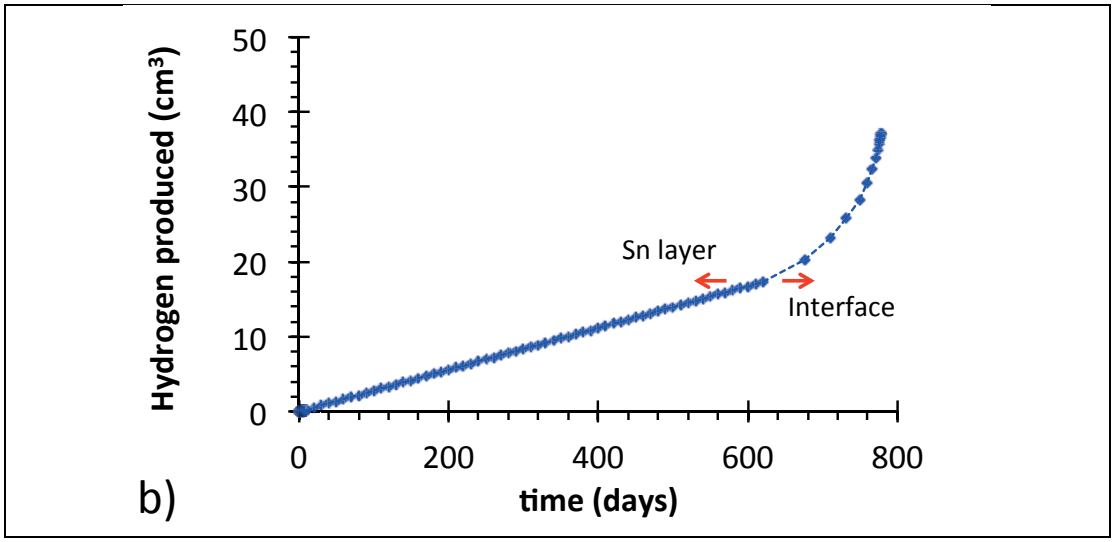

The model can predict the time needed for the dissolution of the tin constituting the Sn layer and the interface. The overall lifetime of tinplate primarily depends on the thickness of the tin layer, while the contribution of the interface is extremely dependent on the coverage degree of the $FeSn_2$ alloy. As shown in **Figure 53b**, an alloy characterized by 50% of coverage provides only a few days of protection after the consumption of the tin layer. In contrast, an alloy with 99% coverage extends the lifetime of the can up to more than one year after the consumption of the tin layer.

Based on the last observations, the lifetime of tinplate can be increased without increasing the nominal tin mass by reducing the roughness of the base steel and by enhancing the quality of the flow-melting treatment. The reduction in roughness will result in an increase of the thickness of the tin layer, while the improvement of the flow-melting treatment will enhance the coverage of the $FeSn_2$ alloy.

5.2.2 Comparison of model predictions with the lifetime of real cans

We prepared two model food cans (type E 2.8/2.8) filled with raspberry puree (pH 3.5) and tomato sauce for canned ravioli (pH 4.2). The compositions of the two foods are reported in **Tables 38** and **39.** More details concerning the production are reported in the Appendix.

Table 38 Composition of the raspberry puree as provided by Bischofszell Food Ltd.

Component	Weight percentage (wt/wt %)
Raspberries	59.0%
Sugar	27.4%
Water	8.7%
Concentrated lemon juice	2.2%
Modified starch	2.0%
Aromas	0.5%
Vanilla extract	0.2%

Table 39 Composition of the tomato sauce for canned ravioli as provided by Bischofszell Food Ltd.

Component	Weight percentage (wt/wt %)
Water	81.10%
Tomato concentrate	14.50%
Sugar	1.60%
Cooking salt	1.20%
Rapeseed oil	1.00%
Glucose syrup	0.40%
Extract of spices	0.10%

The prediction of the lifetime of the cans filled with raspberry puree was done considering the parameters previously determined in Chapters 3 and 4 for the [0.1] citrate buffer at pH 3.0. For the prediction of the cans filled with tomato sauce for canned ravioli, the parameters considered were those determined for the same citrate buffer but at pH 4.5. As an assumption, it was considered that the products were oxygen free.

The structure of the tinplate material (E 2.8/2.8) characterized by means of AES spectroscopy was in agreement with that of the reference commercial sample previously analysed in Chapter 2. The tin layer and the interface thickness were ≥ 20 nm and 850 nm, respectively. All the parameters used for modelling the durability of the cans are summarized in **Table 40**.

Table 40 Input parameters used for the modelling. [1] From Chapter 3, [2] from Chapter 4 and [3] from AES depth profile analysis.

Parameter	pH 3.0	pH 4.5	Units
c_{O2}	0		mol/cm^3
[1] $j_{0,HER}$	8x10^{-5}	7x10^{-5}	mA/cm^2
[1] $E_{rev,\ HER}$	-0.422	-0.507	V vs. SCE
[1] $E_{corr,\ Sn}$	-0.625	-0.703	V vs. SCE
[1] $b_{c,\ HER}$	100	100	mV/dec
[2] ΔE_{corr}	-0.048	-0.068	V
[2] r_p *Sn*	3016	2812	Ω cm^2
[2] r_p *Fe*	4938	4736	Ω cm^2
[3] *Sn layer thickness*	20		nm
[3] *Interface thickness*	850		nm
Can internal surface	320		cm^2
A_{Sn}	Sn At%* x total surface		cm^2
A_{Fe}	Fe At%* x total surface x θ_{FeSn2}		cm^2
θ_{FeSn2}	90%		%

Table 41 shows the comparison between the lifetimes predicted according to the model and the observed lifetimes. The observed lifetime consists of the time taken to reach an evident swelling of the cans. This because these conditions correspond to the situation in which tin is completely dissolved and large areas of base steel undergo acid corrosion producing molecular hydrogen which determines an increase in the internal pressure of the can.

Table 41 Comparison between the lifetime predicted by the model and the observed lifetime.

	Lifetime (days)	
	Raspberry puree	Tomato sauce for canned ravioli
Predicted	50	56
Observed (swelling)	40	180

Interestingly, the predicted lifetime for the raspberry puree cans is very close to the observed lifetime. The good correspondence between the two values results from the fact that the citrate buffer used to determine the input parameter of the model is representative of the raspberry puree composition. In particular, the citric acid contained in the raspberry puree (**Table 38**) seems to be the main parameter characterizing food corrosivity. The overestimation of the lifetime of these cans is most probably due to the fact that for the modelling we did not consider the corrosion accelerator effect of the anthocyanins present in the fruit pigment.

For cans of tomato sauce for canned ravioli, the model underestimates the lifetime of the cans by a factor of 3. This is consistent with the fact that the chemical composition of this food (**Table 39**) is more complex than that of the citrate model solution used to determine the input parameters of the model. In particular, the oil contained in this food is most probably responsible for the slowdown in the kinetics of the corrosion process. Although it is clear that for this type food, the model input parameters need to be determined more clearly, the predicted lifetime is consistent with the observed lifetime and the model estimates the lifetime for the worst corrosivity scenario.

5.3 Applicability of the model for historical collections

To extend the applicability of the model to museum collections of cans, the input parameters need to be obtained by means of non-destructive techniques, or at least minimally invasive methods. Two types of parameters need to be assessed:

- Material parameters of the tinplate
- Chemical parameters of the food

5.3.1 Determining the material parameters of the tinplate

As demonstrated in Chapter 2, the average thickness of the tin layer can be determined in a non-destructive way by means of XRF spectroscopy, although it is not possible to distinguish between pure and alloyed tin. The original thickness of the tin layer originally covering the internal surface of the cans and in contact with the food can be determined by carrying out XRF analysis of the external surface of the cans. However, this is possible only for historical cans produced through the hot-dipping process or for modern cans electrolytically plated with equal tin masses on both surfaces. Unfortunately, the same method cannot be extended to cans coated with differential tin masses. Thus, in this case it is necessary to refer to the nominal tin mass that was theoretically applied on the internal side of the can based on the available information about the production of each specific can.

The width of the interface can be approximated by means of 3D WLI or laser microscopy by determining, for example, the Rz (max peak to valley height) of the

base material. As was shown in Chapter 2, the surface roughness of tinplate coated with a tin mass ≤ 2.8 g/m^2 approaches that of the base steel. Thus, in these cases the roughness analysis carried out on the external side allows an estimation of the interface width. For all the other cases, in which the external tin layer is thick, the roughness needs to be assessed after local removal of the tin layer. For a minimally invasive intervention, the external tin layer should be removed using the methods reported in Chapter 1, from an area as small as possible.

5.3.2 Determining the chemical parameters of the food

As previously demonstrated, the initial concentration of oxygen present in the can after filling, the pH and the types of complexing agents are the three fundamental food parameters for modelling the lifetime of a can. Other components may also play a role, as seen in the previous section. They can retard corrosion and thus disregarding them will lead to the prediction of the worst corrosion scenario. The initial amount of oxygen needs to be estimated based on process data related to the canning, i.e. temperature of hot filling, exhausting, steam flow, presence of head space, etc. [4].

The pH and the type of the principal complexing agent are parameters accessible from canned food databases. These two parameters determine the E_{rev} of hydrogen and the E_{corr} of tin needed for the modelling of the corrosion rate of tin according to **Eq. 20**. The E_{rev} for the HER can directly be calculated by means of Nernst's equation, while the E_{corr} of tin, in the absence of data, needs to be measured or theoretically calculated. Despite the possibility of carrying out the measurement in a minimally invasive way through microelectrodes, the direct measure of the E_{corr} of tin requires access to the inside of the can. Alternatively, based on the dependence of the E_{corr} on the complexing strength of the electrolyte demonstrated in Chapter 3, the E_{corr} can be estimated provided that the complexing strength of the food media towards the tin ions is known.

5.3.3 Estimation of the lifetime of can collections

In the absence of detailed information about the system, the lifetime of cans can be estimated considering the average thickness of the tin layer and the main food

component. By feeding information into the model concerning the material and chemical parameters of a can from a museum collection, conservators can estimate the state of the lifetime of the can and thus define an intervention time line. **Figure 55** shows the application of the model for the buffer systems investigated in this work. The expected lifetime of cans is reported as a function of the content and the thickness of the tin layer characterizing the type of tinplate. The calculation was done without considering a specific stratigraphy. Thus, the thicknesses of the tin layer corresponding to each type of tinplate are average values, i.e. those that can be obtained by means of XRF analysis. Moreover, for the modelling, the interface was disregarded since it has been demonstrated that over the total lifetime of a can, the lifetime of the interface is limited. For all cases, the calculations were made considering the complete filling of the cans at 80 °C (initial oxygen concentration of 3.4 ppm).

Figure 55 Relation between the lifetime of the can, the thickness of the Sn layer and the type of buffer system. Calculations were done considering the 0.4 dm^3 cans to be completely filled at 80 °C with oxalate, citrate and malate buffers.

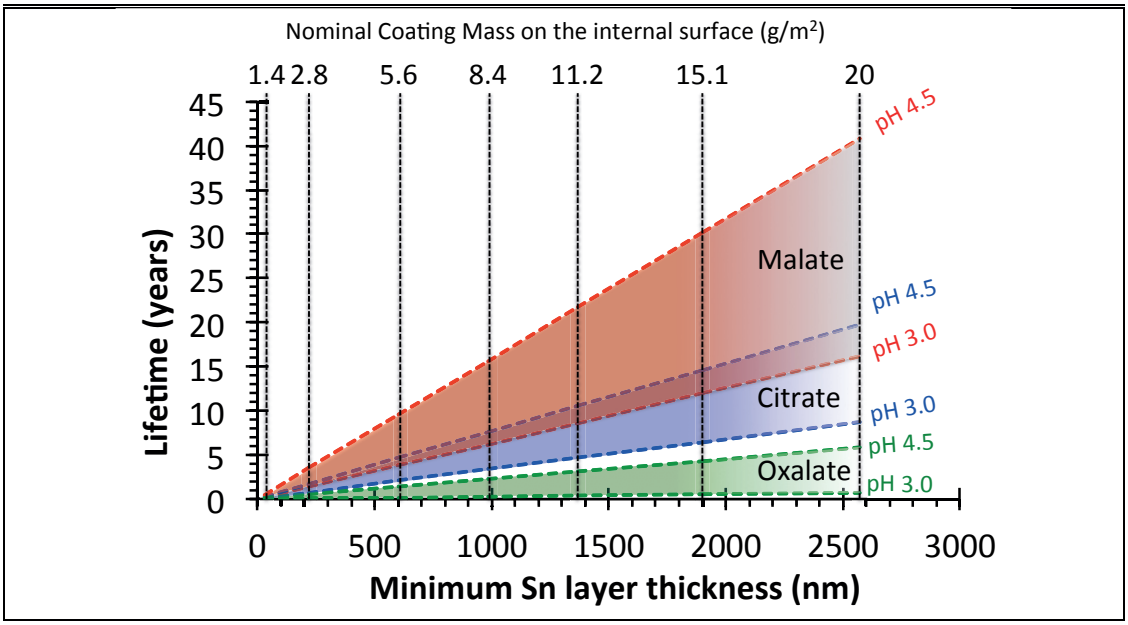

6 Conclusions

This study on the corrosion of tinplates used for food packaging has improved knowledge of the degradation phenomena occurring in the long term and determined the mechanisms and the kinetics of the corrosion reactions involved.

A multi-technique approach based on cutting-edge analysis has proved to be the best method for an exhaustive and precise characterization of tinplate structure and for providing the input material parameters needed for the model. In particular, Auger electron spectroscopy (AES) allows local description of the stratigraphy of tinplate by determining the thickness of the tin layer, the interface and the tin-iron atomic ratio along the interface. X-ray fluorescence (XRF) has been demonstrated to be a valuable alternative for the characterization of tinplate structure. Although this method provides average values over larger analysis areas compared to the AES, the rapidity and the possibility of working in a non-destructive way makes this technique extremely useful for characterizing the material of historical collections.

By means of an electrochemical approach, it has been possible to describe the mechanisms and to quantify the kinetics of the oxygen reduction reaction (ORR), the hydrogen evolution reaction (HER) and the effect of the type of complexing agents on the global reaction of tin dissolution. Electrochemical methods have enabled description of the galvanic coupling mechanism between tin and iron in citrate buffer solutions and furthermore to clarify its effect on the overall corrosion rate of tinplate. The identification of the effect of the single food chemical components on the corrosion rate of tinplate may allow conservators to make predictions concerning the corrosion rates of tinplates with regard to a specific food.

A corrosion model for the prediction of the lifetime of plain tinplated cans combining the material structure with the mechanisms and the kinetics of the corrosion of tin and tin-iron galvanic coupling has been proposed. The model is a promising and powerful tool for helping museum conservators to define an intervention timeline for historical cans. However, at the moment it cannot be indiscriminately applied to every can.

Further work should be done to extend the applicability of the model to a wider range of canned food. This will be possible by carrying out studies on the kinetics of tin corrosion and tin-iron galvanic coupling for a greater number of food molecular components to create a larger database available to conservators. On the material side, the electrochemical behaviour of the $FeSn_2$ alloy needs to be investigated to a greater extent to determine the mechanisms and kinetics of corrosion and the galvanic coupling effect between the tin and the base steel.

References

[1] M. Warner. House history: some assembly required. 2009.

[2] G.L. Robertson. Food packaging principles and practice. Third Edition. New York: CRC Press Taylor & Francis Group. 2013. 703pp.

[3] G. Barone, L. Bolzoni, G. Caruso, A. Montanari, S. Parisi, I. Sfeinka. Food packaging hygiene. London: Springer. 2015. 132pp.

[4] L. Selwyn. Metals and corrosion: a handbook for the conservation professional. Ottawa: Canadian Conservation Institute. 2004.

[5] L. Brambilla, A. Michel, R. Bertholon. Condition of cans in collections: a challenge in conservation. Proceedings of the Interim Meeting of the ICOM-CC Metals Working Group. 26–30 September 2016, New Delhi, India, pp. 266-274.

[6] L. Brambilla, F. Cova Caiazzo, A. Michel, S. Mischler, R. Bertholon. Degradation of heritage cans: monitoring of museums' collections. Measurements. 2018; 127(10): pp. 256-263.

[7] ITRI Ltd. Guide to tinplate. Second edition. United Kingdom: ITRI Ltd (Tinplate Panel). 2000. 123pp.

[8] E. Morgan. Tinplate and modern canmaking technology. Oxford: Pergamon Press. 1985. 268pp.

[9] ASTM A623-16. Standard specification for tin mill products, general requirements. 2016.

[10] R.A. Covert, H.H. Uhlig. Chemical and electrochemical properties of $FeSn_2$. Journal of Electrochemical Society. 1957; 104(9): pp. 537-542.

[11] D.R. Gabe. Structure and constitution of the tinplate alloy layer. Iron Steel. 1960; 40(4): pp. 118-122.

[12] H.E. Biber, W.T. Harter. The growth of $FeSn_2$ layers on specifically oriented iron single crystal. Journal of Electrochemical Society. 1957; 113(8): pp. 828-834.

[13] R.P. Frankenthal, A.W. Loginow. Kinetics of the formation of the iron-tin alloy $FeSn_2$. Journal of Electrochemical Society. 1960; 107(11): pp. 920-922.

[14] D.R. Gabe. Structure and constitution of the tinplate alloy layer. Iron Steel. 1960; 40(5): pp. 162-165.

[15] D.R. Gabe, M. Met. Principles of metal surface treatment and protection. Second edition. Oxford: Pergamon Press. 1978. 211pp.

[16] D.R. Gabe, R.J. Mort. Electron metallography of tinplate alloy layers. Journal of the Iron and Steel Institute. 1965; 1: pp. 64-70.

[17] N. Sarafianos. Determining reaction time at iron/tin interface of electrolytic tinplate during first stage of $FeSn_2$ growth. Materials Science and Technology. 1987; 3(1): pp. 66-71.

[18] UNI EN 10202:2004, Prodotti per imballaggio laminate a freddo – Banda stagnata elettrolitica e banda cromata elettrolitica.

[19] ASTM A630-03. Standard test methods for determination of tin coating weights for electrolytic tin plate. 2014.

[20] C.T. Kunze, A.R. Willey. Electrolytic determination of tin and tin-iron alloy coating weights on tin plate. Journal of the Electrochemical Society. 1952; 99(9): pp. 334-359.

[21] M. Tsurumaru, A. Nunokawa, Y. Suzuki. Evaluation of iron exposure on tinplate and in tinplate cans. Proceeding of the 2nd International Tinplate Conference, London. 1980; 31: pp. 348-359.

[22] G. Milanese, A. Montanari, R. Massini, A. Cassarà. Sperimentazione e applicazioni di un metodo per valutare il ferro esposto sulle bande stagnate. Industria Conserve, Parma. 1984; 59(5): pp. 120-124.

[23] I.M. Notter, D.R. Gabe. Polarization resistance methods for measurement of the porosity of thin metal coatings. Corrosion Science. 1993; 34(5): pp. 851-870.

[24] G.G. Kamm, A.R. Willey, R.E. Beese, J.L. Krickl. The alloy-tin couple test – a new research tool. Corrosion. 1961; 17(2): pp. 84-92.

[25] S. Ramamurthy, T.L. Walzak, S.F. Lu, T.C. Lipson N.S. McIntyre. Study of tinplate structure using imaging secondary ion mass spectrometry. Surface and Interface Analysis. 1991; 17: pp. 834-841.

[26] S.F. Lu, G.R. Mount, N.S. McIntyre, A. Fenster. Use of image depth profiling SIMS for the study of tinplate corrosion. Surface and Interface Analysis. 1994; 21: pp. 177-183.

[27] N. Sarafianos. Auger depth profiling and diffusion measurements in electrolytic tinplate. Zeitschrift fur Metallkunde. 1995; 86(11): pp. 794-799.

[28] R. Coles, D. McDowell, M.J. Kirwan. Food packaging technology. Oxford: CRC Press LLC. 2003. 346pp.

[29] FAO Food and nutrition paper 36. Guidelines for can manufacturers and food canners. 1986. Rome: Food and Agriculture Organization of the United Nations.

[30] C.H. Mannheim, N. Passy. Internal corrosion and shelf-life of food cans and methods of evaluation. 1982; 17(4): pp. 371-407.

[31] I. Saguy, C.H. Mannheim, N Passy. The role of sulphur dioxide and nitrate on detinning of canned grape juice. Journal of Food Technology. 1973; 8: pp. 147-155.

[32] A. Albu-Yaron, A. Semel. Nitrate-induced corrosion of tinplate as affected by organic acid food components. Journal of Agricultural and Food Chemistry. 1976; 24(2): pp. 344-348.

[33] F.W. Salt, J.G.N. Thomas. The anaerobic corrosion of tin in anthocyanin solutions and fruit syrups. Journal of Applied Chemistry. 1957; 7(5): pp. 231-238.

[34] J.C. Sherlock, S.C. Britton. Complex formation and corrosion rate for tin in fruit acids. British Corrosion Journal. 1972; 7(1): pp. 180-183.

[35] A.R. Willey. Effect of tin ion complexing substances on the relative potentials of tin, steel and tin-iron alloy in pure acid and food media. British Corrosion Journal. 1972; 7(2): pp. 29-35.

[36] M. Lamberigts, J.F. Willem. Effect de l'adsorption d'etain stanneux sur le comportement électrochimique du fer dans les milieu légèrement acides désaérés Application à la corrosion du fer-blanc. Science Recherche Développement, Commission Européenne. 1998; EUR 18424 : pp. 1-86.

[37] J. Jarosz, C. Sinicki. Determination des constantes de dissociation des complexes formé entre l'étain stanneux e les espèces citriques en milieu acid. Comptes Rendus de l'Académie des Sciences. 1981; 292: pp. 793-795.

[38] V.K. Gouda, E.N. Rizkalla, S. Abd-El-Wahab, E.M. Ibrahim. Corrosion behaviour in organic acid solutions – I Tin electrode. Corrosion Science. 1981; 21(11): pp. 1-15.

[39] V.K. Gouda, S.M. Abd-El-Wahab, E.M. Ibrahim. Corrosion behaviour in organic acid solutions – II a Steel electrode. Corrosion Science. 1980; 20(1): pp. 1091-1099.

[40] G. Bombara, N. Azzeri, G. Baudo. Electrochemical evaluation of the corrosion behaviour of tinplate. Corrosion Science. 1970; 10(1): pp. 847-856.

[41] D. Landolt. Corrosion and surface chemistry of metals. Lausanne EPFL Press. 2007.

[42] R.M. El-Sherif, W.A. Badawy. Mechanism of corrosion and corrosion inhibition of tin in aqueous solutions containing tartaric acid. International Journal of Electrochemical Science. 2011; 6: pp. 6469-6482.

[43] A. Ninčević Grassino, Z. Grabarić, A. Pezzani, G, Squittieri, K. Berković. Corrosion inhibition with different protective layers in tinplate cans for food preservation. Journal of the Science of Food and Agriculture. 2010; 90(7): pp. 2419-2426.

[44] A. Ninčević Grassino, Z. Grabarić, A. Pezzani, G. Fasanaro, A. Lo Voi. Influence of essential onion oil on tin and chromium dissolution from tinplate. Journal of Food and Chemical Toxicology. 2009; 47: pp. 1556-1561.

[45] J.C. Sherlock, J.H. Hancox, S.C. Britton. Rate of dissolution of tin from tinplate in oxygen-free citrate solutions: I. Assessment by polarisation measurements. British Corrosion Journal. 1972; 7(9): pp. 222-226.

[46] E.L. Koehler, C.M. Canonico. Corrosion mechanisms in the plain can. Corrosion. 1957; 13(6): pp. 19-29.

[47] G.G. Kamm, A.R. Willey. Corrosion resistance of electrolytic tin plate. Corrosion. 1961; 17(2): pp. 99-106.

[48] S.C. Britton, K. Bright. Influence of area of the steel component on behaviour of a tin-steel couple. Corrosion. 1960; 17(4): pp. 120-124.

[49] M. Pourbaix. Atlas of electrochemical equilibria in aqueous solutions. Second edition. Houston: NACE. 1974. 643 pp.

[50] M. Šeruga, M. Metikoš-Huković. Passivation of tin in citrate buffer solutions. Journal of Electroanalytical Chemistry. 1992; 334(12): pp. 223-240.

[51] C.A. Gervasi, M.V. Bimbi, P.E. Alvarez. Characterization of anodic tin passive films formed in citrate buffer solutions. Journal of Electroanalytical Chemistry. 2009; 625: pp. 60-68.

[52] A.s Tselesh. Anodic behaviour of tin in citrate solutions: The IR and XPS study on the composition of passive layer. Thin solid films. 2008; 516(12): pp. 6253-6260.

[53] C.A. Gervasi, P.A. Palacios, M.V. Fiori Bimbi, P.E. Alvarez. Electrochemical studies on the anodic behaviour of tin in citrate buffer solutions. Journal of Electroanalytical Chemistry. 2010; 639: pp. 141-146.

[54] M. Šeruga, M. Metikoš-Huković, T. Valla, M. Milun, H. Hoffshultz, K. Wandelt. Electrochemical and X-ray photoelectron spectroscopy studies of passive film on tin in citrate buffer solution. Journal of Electroanalytical Chemistry. 1992, 334(3): pp. 223-240.

[55] C.A. Gervasi, P.E. Alvarez, M.V. Bimbi, M.E. Folquer. Comparative cyclic voltammetry and SEM analysis of tin electrodes in citrate buffer solutions. Journal of Electroanalytical Chemistry. 2007; 601(12): pp. 194-204.

[56] C.A. Gervasi, P.A. Palacios, P.E. Alvarez, M.V. Fiori-Bimbi, S.A. Brandan. Electronic structure of tin passive films and its influence on the corrosion of the base metal. Industrial & Engineering Chemistry Research. 2013; 52: pp. 9115-9120.

[57] H. Do Duc, P. Tissot. Anodic behaviour of tin in neutral phosphate solutions. Corrosion Science. 1979; 19: pp. 179-180.

[58] H. Do Duc, P. Tissot. Rotating disc and ring disc electrode studies of tin in neutral phosphate solution. Corrosion Science. 1979; 19: pp. 191-197.

[59] B.N. Strirrup, N.A. Hampson. Anodic passivation of tin in sodium hydroxide solutions. Journal of Electroanalytical Chemistry. 1976; 67(5): pp. 45-56.

[60] P. Keller, H.H. Strehblow. XPS-studies on the formation of passive layers on Sn and CuSn alloys in 0.1M KOH. Journal of Physical Chemistry. 2005; 219(7): pp. 1481-1488.

[61] A. Palacios-Padrós, F. Caballero-Briones, I. Díez-Pérez, F. Sanz. Tin passivation in alkaline media: formation of SnO microcrystals as hydroxyl etching product. Electrochimica Acta. 2013; 111(7): pp. 837-845.

[62] H.H. Hassan, K. Fahmy. Pitting corrosion of tin by acetate anion in acidic media. International Journal of Electrochemical Science. 2008; 3: pp. 29-43.

[63] M.A. Deyab. Hydrogen generation by tin corrosion in lactic acid solution promoted by sodium perchlorate. Journal of Power Sources. 2014; 268(6): pp. 765-770.

[64] O. Azizi, M. Jafarian, F. Gobal, H. Heli, M.G. Mahjiani. The investigation of the kinetics and mechanisms of hydrogen evolution reaction on tin. Journal of Hydrogen Energy. 2007; 32(10): pp. 1755-1761.

[65] M. Jafarian, F. Gobal, I. Danaee, T. Biabani, M.G. Mahjani. Electrochemical studies of the pitting corrosion of tin in citric acid solution containing Cl^-. Electrochimica Acta. 2008; 53: pp. 4528-4536.

[66] S.S. Abdel Rehim, S.M. Sayyah, M.M. El Deeb. Corrosion of tin in citric acid solution and effect of some inorganic anions. Materials Chemistry and Physics. 2003; 80: pp. 696-703.

[67] S.S. Abd El Rehim, A.M. Zaky, N.F. Mohmed. Electrochemical behaviour of a tin electrode in tartaric acid solutions. Journal of Alloys and Compounds. 2006; 424(12): pp. 88-92.

[68] A. Collazo, R. Figueroa, X.R. Nóvoa, C. Pérez. Corrosion of electrodeposited Sn in 0.01M NaCl solution. A EQCM and EIS study. Electrochimica Acta. 2016; 202(12): pp. 288-298.

[69] M. Drogowska, L. Brossard, H. Ménard. Dissolution of tin in the presence of Cl^- ions at pH 4. Journal of Applied Electrochemistry. 1989; 19(8): pp. 231-238.

[70] T.P. Hoar. The electrochemical behaviour of the tin-iron couple in dilute acid media. Trans. Faraday Soc. 1934; 30: pp. 472-482.

[71] E.L. Koehler. The tin-steel couple in air-free citric acid solution. Journal of Electrochemical Society. 1956; 103(9): pp. 486-491.

[72] C. Luner, M.V. Murray. Isolation and examination of alloy layers from electrolytic tinplate. Journal of the Electrochemical Society. 1963; 110(2): pp. 176-178.

[73] M. Stern. The effect of alloying elements in iron on hydrogen overvoltage and corrosion rate in acid environments. Journal of the Electrochemical Society. 1955; 102(12): pp. 663-668.

[74] K.D. Childs, B.A. Carlson, L.A. LaVanier, J.F. Moulder, D.F. Paul, W.F. Stickle, D.G. Watson. Handbook of Auger electron spectroscopy. Physical Third Edition. Eden Prairie (Minnesota): Electronics Inc. 1995. 249pp.

[75] D. Briggs, M.P. Seah. Practical surface analysis by Auger and X-ray photoelectron spectroscopy. Chichester: John Wiley & Sons Ltd. 1983. 533pp.

[76] H. Kaesche. Corrosion of metals: physicochemical principles and current problems. Corrosion Science. Berlin: Springer. 2003; 603pp.

[77] A.L. Colley, J.V. Macpherson, P.R. Unwin. Effect of high rates of mass transport on oxygen reduction at copper electrodes: implications for aluminium corrosion. Electrochemistry Communications. 2008; 10: pp. 1334-1336

[78] A.C. Vieira, A.M. Pinto, L.A. Rocha, S. Mischler. Effect of Al_2Cu precipitates size and mass transport on the polarization behaviour of age-hardened Al-Si-Cu-Mg alloys in 0.05M NaCl. Electrochimica Acta. 2011; 56: pp. 3821-3828.

[79] K.J. Vetter, F. Gorn. Kinetics of layer formation and corrosion processes of passive iron in acid solutions. Electrochimica Acta. 1973; 18: pp. 321-326.

[80] S.E. Traubenberg, R.T. Foley. The influence of chlorides and sulphate ions on the corrosion of iron in sulphuric acid. J. Electrochemical Society. 1971; 118(7): pp. 1066-1070.

Appendix

Preliminary corrosion experiments on cans

Goal

Canned foods are not stable systems and thus their corrosivity may change as a function of time. The aim of this section is to study the effect of food aging on corrosivity with regard to tin and iron. The aging of the canned food was achieved by means of accelerated thermal aging and real-time aging. Moreover, the results regarding the electrochemical behaviour of tin and iron in food systems are used to validate the results of the previous chapters obtained for model electrolytes.

Material and methods

Materials and electrolytes

Commercial tomato sauce for canned ravioli was chosen as the food for accelerated thermal aging. The production and the canning were done by Bischofszell Food Ltd in Bischofszell (Switzerland). The tomato sauce (composition previously reported in **Table 39**) was canned in three-piece tinplated cans internally coated with polymer. The type of tinplate according UNI EN 10202:2004 is E 2.8/2.8, the internal surface is coated with white epoxy-phenolic lacquer and the lateral solder is protected by means of a polyester strip. This type of can, in which tinplate is protected with a lacquer, was chosen to achieve only the aging of the food independently of the corrosion of the container. The thermal aging of the cans was carried out over two years at three temperatures:

- 3 °C, carried out in a commercial refrigerator.
- 22 °C, carried out in underground storage without temperature control, but at a constant temperature.
- 40 °C, carried out in an incubator.

The effect of natural aging was assessed by using the food content in the two different cans belonging to the collection of the historical museum of Bern as electrolytes for the electrochemical tests. The analysed foods were, respectively, peeled tomatoes and pea and carrot salad. In the museum, cans underwent 20 years of natural aging at room temperature. Commercially available cans of the same brand, containing the same products and manufactured by the same producers were analysed to compare the corrosivity of the foods over a shorter aging period. The compositions of the naturally aged canned foods are reported in **Table 42**.

Table 42 Composition of the cans from the museum of Bern as reported on the label.

Type of food	Component	Weight percentage (wt/wt%)
Peeled tomatoes	Peeled tomatoes	70%
	Tomato juice	30%
Pea and carrot salad	Peas	31%
	Carrots	31%
	Water	38%
	Cooking salt	n.a.

The electrochemical measurements were carried out on pure tin (99.999+%) and on Armco iron supplied by GoodFellow Cambridge Ltd. The two materials supplied as rods were transformed in disk electrodes. The rods of the two metals were machined up to a final diameter of 0.5 cm and afterwards embedded in epoxy resin. The final electrode diameter was 1 cm, while the active surface was 0.196 cm^2. Prior to each electrochemical test, the samples were mechanically polished up to 4000 grit with SiC paper and cleaned in pure ethanol by means of an ultrasonic bath, according to the procedure described in section 3.1.1.

Measures of pH and conductivity:

After 60 h of stabilization at room temperature, the cans were opened and the pH and conductivity of canned foods were measured. A pH meter (Metrohm model 654) and conductivity meter (Meterlab model CDM 210) were used to measure the pH and the conductivity respectively. For each test, the measurements were carried out at the centre and half height of the can cylinder.

Electrochemical measurements of food corrosivity:

The electrochemical measurements of food corrosivity with respect to tin and iron were carried out in an airtight 400 ml electrochemical cell from Metrohm. The electrochemical experimental setup is shown in **Figure 56**. The tin and iron electrodes were dipped in 350 ml of aged food and the SCE was placed in the centre of the electrochemical cell at half distance from the two working electrodes. A high surface gold mesh was used as counter electrode. The electrodes were connected to the potentiostat through the multiplex system MULTI4 from Metrohm Autolab. Two independent channels of the system shared the same reference electrode and counter electrode, while two independent working electrode channels were connected to the tin and iron electrodes, respectively.

Over the two hours before starting the test and for its entire duration, Ar saturated in water was bubbled in the cell to minimize the oxygen content of the system. The OCP of tin and iron was alternately measured every 30 s for 30 s over the two hours needed for the system stabilization. Afterwards, the polarization resistance of the two electrodes was assessed by means of PP from -10 mV vs. OCP to +10m V vs. OCP with a scan rate of 2 mV/s.

Solution resistance was assessed using EIS measurements carried out using the open circuit potential (OCP) in a frequency range from 100 KHz to 1 Hz by applying ± 10 mV as the amplitude for the perturbation. The electrochemical behaviour of tin and iron over a wider range of potential was assessed by means of PP. The potential sweep was carried out first in the cathodic direction, starting from the OCP to -100 mV vs. OCP and after 180 s of relaxation in the anodic direction from OCP to +100 mV vs. OCP. The galvanic coupling between tin and iron was investigated using the same procedure and experimental setups as described in section 4.1.2 with the electrochemical cell setup shown in **Figure 56**.

Figure 56 Electrochemical cell setup.

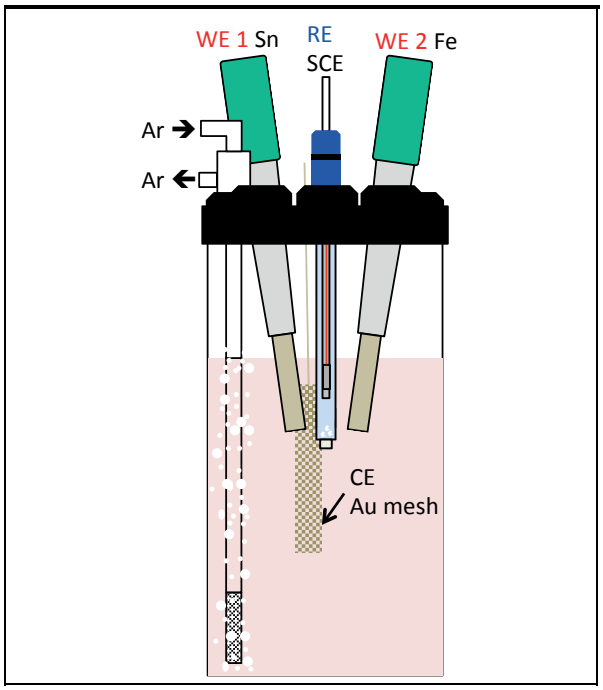

Results

Evolution of pH and conductivity:

The pH and conductivity values of the canned foods after thermal and natural aging are listed in **Table 43**. The variation in the two parameters is more significant for food aged by means of natural aging than thermal aging, which induces negligible results for both parameters. The pH decreases after thermal aging for tomato sauce for canned ravioli and after natural aging for pea and carrot salad. In contrast, for peeled tomatoes, natural aging determines the increase in pH.

After thermal aging, the samples aged at 3 °C and 22 °C show a large discrepancy in the results and on average very close values for conductivity. Conductivity increases after thermal aging at 40 °C. The conductivity decreases significantly after 20 years of natural aging for both foods.

Table 43 pH and conductivity values measured at room temperature in the canned foods after thermal and natural aging.

Type of food	Aging temperature (°C)	Aging time (years)	pH	mS/cm
Tomato sauce for canned ravioli	40°C	2	4.108	20.96
"	40°C	2	4.139	20.95
"	22°C	2	4.170	20.62
"	22°C	2	4.169	20.83
"	3°C	2	4.174	20.61
"	3°C	2	4.183	20.80
Peeled tomatoes	Not controlled	20	4.580	7.42
"	Not controlled	2	4.264	9.18
Pea & carrot salad	Not controlled	20	5.136	10.67
"	Not controlled	2	5.589	12.79

Electrochemical determination of food corrosivity:

Figure 57 shows the OCP potentials of tin and iron electrodes measured after 2 h of de-aeration in all the aged foods. As observed for the model electrolytes, in this case also the OCP corresponds to the E_{corr}. In tomato sauce for canned ravioli (**Figure 57a**) the E_{corr} values of tin and iron are close to -0.650 V vs. SCE and -0.600 V vs. SCE, respectively. Interestingly, the E_{corr} values do not change for thermally aged food: both tin and iron show constant E_{corr} values. The polarity of the tin-iron couple is constant and in each test, the E_{corr} of tin is 50 mV lower than the E_{corr} of iron. **Figures 57b** and **57c** show the evolution of the E_{corr} of tin and iron induced by the natural aging of peeled tomatoes and of pea and carrot salad. After two years of natural aging, the tin-iron couple maintains the same polarity and the ΔE_{corr} previously observed in tomato sauce for canned ravioli. Nevertheless, the ΔE_{corr} between tin and iron and the polarity of the tin-iron couple are not maintained in foods naturally aged for 20 years. The E_{corr} values of tin and iron are nearly the same for peeled tomatoes and pea and carrot salad (**Figures 57b** and **57c**). ΔE_{corr} drops below 10 mV.

Figure 57 Corrosion potentials of tin and iron measured after 2 h of stabilization and de-aeration in tomato sauce for canned ravioli a), peeled tomatoes b) and pea and carrot salad c).

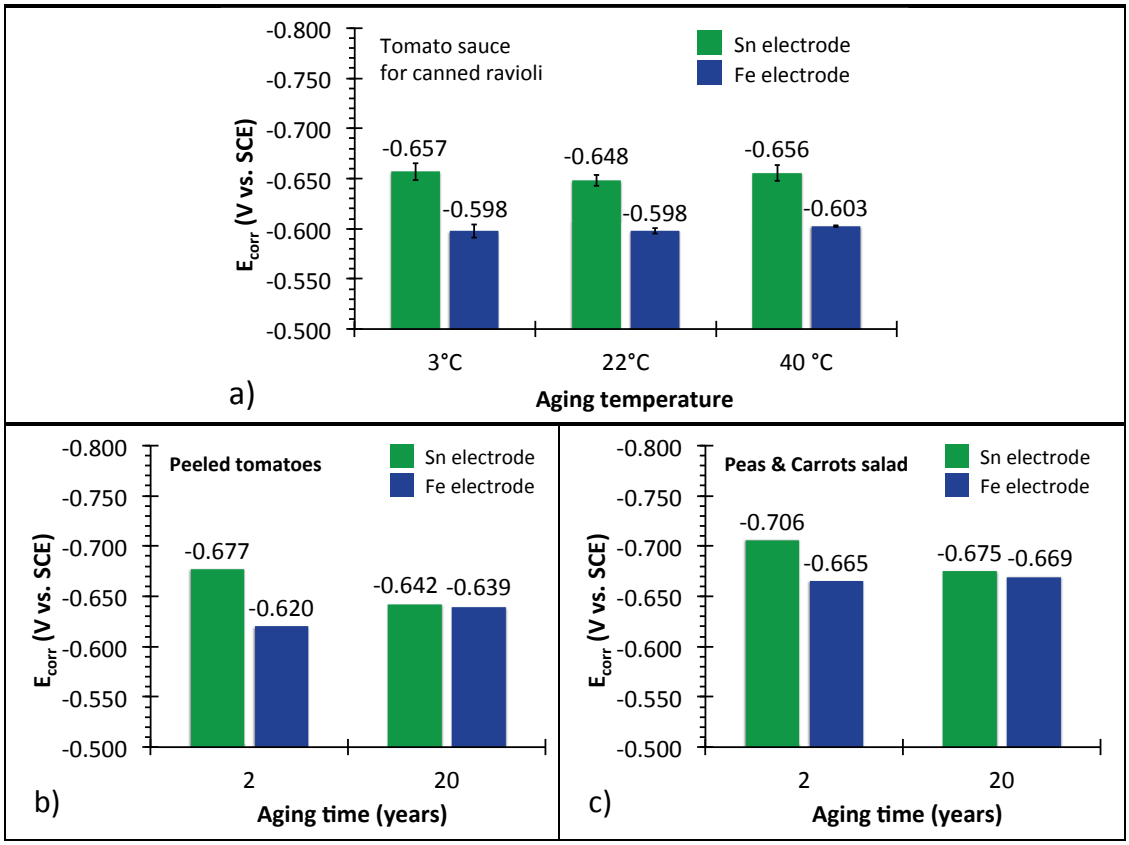

The evolution of food corrosivity as a function of the aging time and condition was assessed by means of the polarization resistance method. The reciprocal of the polarization resistance is directly proportional to the corrosion rate. Thus, this parameter has been used in **Figures 58** and **59** to show the evolution of food corrosivity with regard to tin and iron.

Figures 58a and **59a** show that the corrosivity of tomato sauce for canned ravioli increases as a result of thermal aging. The linear increase in the corrosion rate of tin with thermal aging is extremely weak compared to the exponential increase in the corrosion rate of iron. It should be emphasized that all the measurements were done after temperature stabilization at room temperature. Thus, the evolution of food corrosivity has to be attributed only to the chemical and physical modifications of the food induced by thermal aging.

The corrosion rates of tin and iron measured in naturally aged foods are shown in **Figures 58b** and **59b,** respectively. Also in this case, aging induces an increase in the corrosivity of foods for both tin and iron.

Figure 58 Evolution of the reciprocal of polarization resistance of tin as a function of accelerated thermal aging a) and natural aging b).

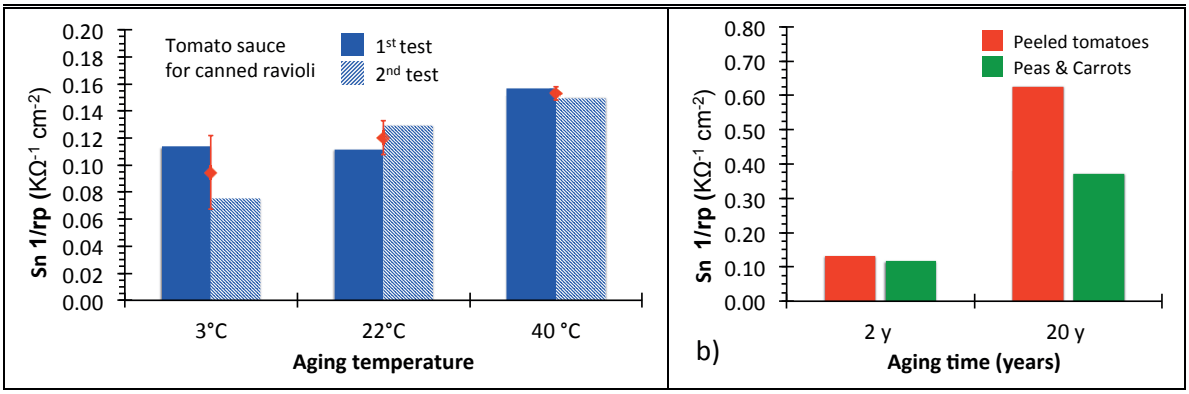

Figure 59 Evolution of the reciprocal of polarization resistance of iron as a function of accelerated thermal aging a) and natural aging b).

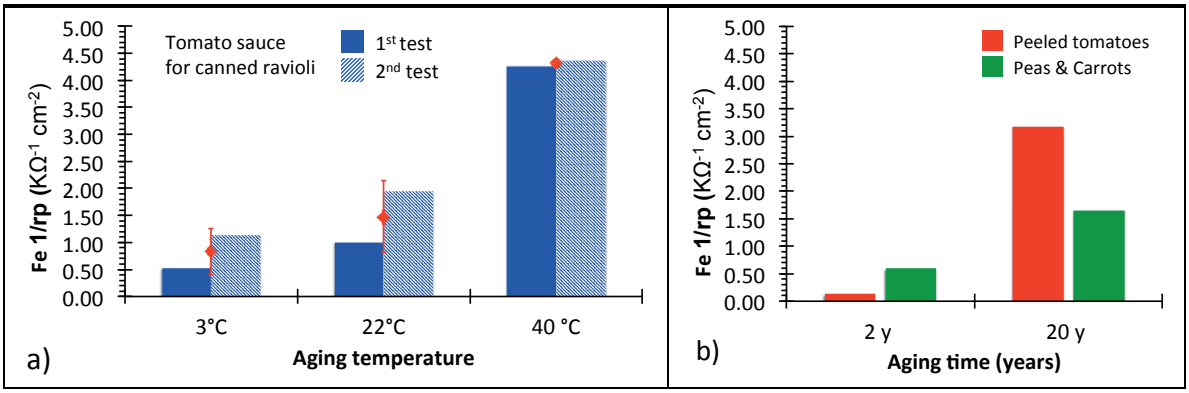

Tin-iron galvanic coupling in foods:

Figure 60 shows the E_{corr} of Sn and Fe and the E_{coup} and j_{coup} measured for all the food systems studied in this appendix. They were determined based on the same procedure as described in Chapter 4. The results confirm that in foods aged for two years at different temperatures, the E_{corr} of Sn is lower than that of iron and thus the tin-iron couple is well represented by the equivalent circuit shown in **Figure 49a**.

Although after 20 years of natural aging, the ΔE_{corr} between tin and iron becomes smaller, the E_{corr} of tin is lower than that of iron. Thus, even after 20 years the circuit shown in **Figure 49** can describe the polarity of the tin-iron couple in food cans. In all cases, electrons flow from tin to iron; the only exception is observed in peeled tomatoes from retail, for which at the beginning of the coupling a negative j_{coup} is recorded.

However, after 21 h of coupling, all systems show a positive j_{coup} flowing from iron to the tin electrode. Depending on the food, j_{coup} values shift from 1 up to

12 µA/cm^2. Interestingly, the tomato soup for canned ravioli thermally aged at 40 °C shows the highest j_{coup} compared to the same food aged at lower temperatures and also the other types of food naturally aged. Thus, the coupling between equal areas of tin and iron enhance the tin dissolution in all the foods tested.

Table 44 Reference legend for the galvanic coupling tests.

Reference	Type of food	Aging temperature (°C)	Aging Time (years)
a	**Tomato sauce for canned ravioli**	40°C	2
b	"	40°C	2
c	"	22°C	2
d	"	22°C	2
e	"	3°C	2
f	"	3°C	2
g	**Peeled tomatoes**	Not controlled	20
h	"	Not controlled	2
i	**Pea & Carrot salad**	Not controlled	20
l	"	Not controlled	2

Figure 60 E_{corr} Fe, E_{corr} Sn and E_{coup}, j_{coup} measured in the food systems. Measurements were undertaken immediately after coupling (initial) and after 21 h of coupling (final).

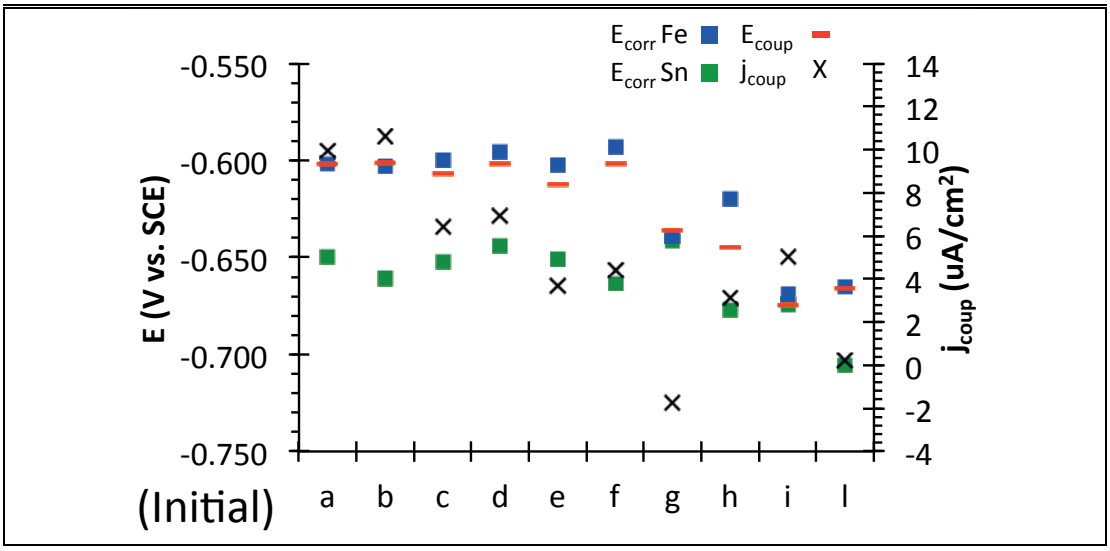

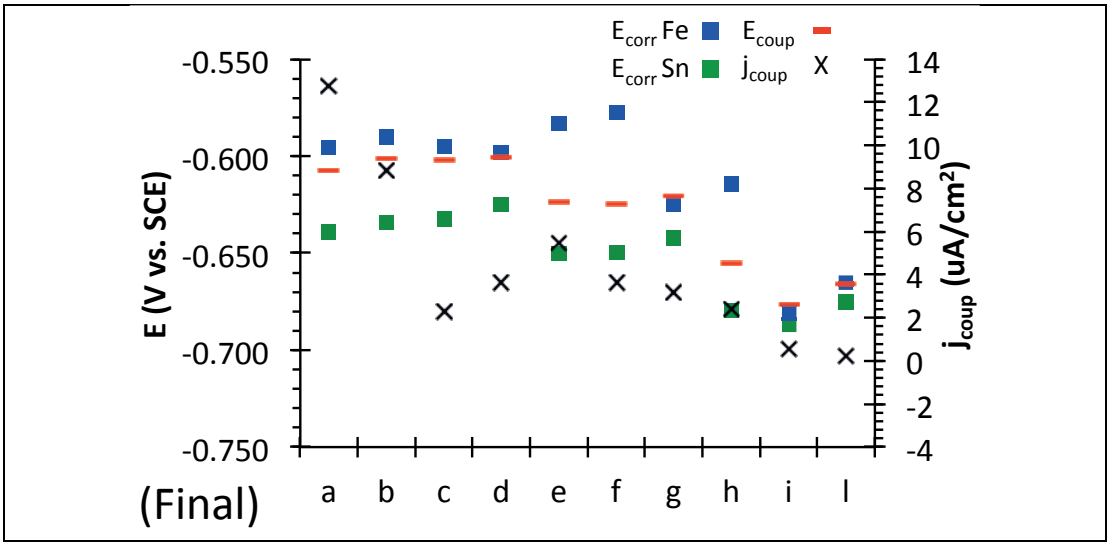

Discussion

Effects of aging on pH and conductivity

The variations in the pH and conductivity of tomato sauce for canned ravioli induced by thermal aging are extremely weak. The variability among the different cans, rather than the modifications induced by aging, could be the origin of the small differences in pH and conductivity. The data concerning natural aging are limited due to the fact that the analysed foods were from unique items in museum collections. Thus, it was not possible to assess the reproducibility of the measurements. Despite these issues, it is possible to formulate consistent hypotheses regarding the reason why the pea and carrot salad underwent to acidification with natural aging while the opposite effect occurred for peeled tomatoes. The acidification of pea and carrot salad was most likely due to the degradation reactions of the food, such as fermentation, which accumulates in canned food. In contrast, the increase in the pH observed in peeled tomatoes was most probably due to the acid corrosion of the tinplate underneath the protective coating. This hypothesis was confirmed by the fact that when the can was opened, large areas of the protective lacquer were missing.

Effects of aging on the corrosivity of food: E_{corr} / $1/r_p$

According to the literature [2,3,28,30], the release of tin over time due to corrosion follows the empirical trend reported in **Figure 60**. Canned foods are dynamic systems

supposed to change their chemical and physical properties over time. However, the evolution of the corrosivity of food with respect to aging has not previously been assessed.

Interestingly, despite the corrosion potentials of tin and iron, **Figures 58** and **59** show the increase in the corrosion rates of both tin and iron as a function of food aging independently of the type of food. The corrosion rate of tin is similar in all the three types of food aged for two years at room temperature. In contrast, 20 years of natural aging leads to an increase of food corrosivity much higher than that observed after thermal aging (**Figure 53b**). Interestingly, the increase in the corrosion rate of iron for naturally aged foods is consistent with that observed after accelerated thermal aging. This suggests that the food modifications responsible for the increase in iron corrosion can be achieved through accelerated thermal aging. For tin, these phenomena are mainly time dependent and the aging temperature has a limited effect. Tin and iron have similar E_{corr} values in natural aged food over two years. For both aging conditions, tin is 50 mV vs. SCE cathodic to iron. However, after 20 years of natural aging, ΔE_{corr} is reduced to < 10 mV. Complexing agents, such as organic acids contained in canned fruits and vegetables [35], reduce the concentration of free tin ions and maintain tin cathodic to iron. However, during aging the amount of dissolved tin increases, while the concentration of complexing agents is constant. Thus, at a certain point, the concentration of complexing agents is no longer sufficient to lower concentrations of free tin ions and thus the E_{corr} of tin approaches that of iron [38,39]. For longer aging, it is plausible that the E_{corr} of tin may shift towards higher potentials than those of iron. In this situation, iron is no longer protected by tin and localized corrosion phenomena can occur at iron sites [2,3,8,15,28-30].

Tin-iron galvanic coupling in foods:

Table 45 shows the comparison between the galvanic coupling currents of the tin-iron couple measured and calculated by means of **Eq. 21**, as shown in Chapter 4. Interestingly, in tomato sauce for canned ravioli, for all the conditions of thermal aging, the calculated j_{coup} values approach with good approximation the measured

j_{coup} values. In contrast, for peeled tomatoes and pea and carrot salad, the calculated j_{coup} differs with respect to the measured j_{coup}.

A hypothesis for these results could be that tomato sauce for canned ravioli is 100% liquid food, while both peeled tomatoes and pea and carrot salad contain large fractions of solids, which may affect the direct measures of j_{coup} and/or the determination of the input parameters of **Eq. 2** for the calculation of the j_{coup}.

Table 45 Comparison between the measured coupling current density values and those calculated by means of **Eq. 21**.

Ref.	Type of food	Aging conditions	Coupling time	j_{coup} (μA/cm^2)	
				Measured	Calculated (Eq. 10)
a	Tomato sauce for canned ravioli	2 y – 40 °C	Initial	9.9	7.2
			Final	12.7	6.2
b	"	2 y – 40 °C	Initial	10.6	8.8
			Final	8.9	7
c		2 y – 22 °C	Initial	6.4	5.3
			Final	2.3	2.2
d	"	2 y – 22 °C	Initial	6.9	5.9
			Final	3.6	1.7
e	"	2 y – 3 °C	Initial	3.7	4.6
			Final	5.4	6.9
f	"	2 y – 3 °C	Initial	4.4	4.9
			Final	3.6	4.8
g	Peeled tomatoes	20 y	Initial	-1.8	0.2
			Final	3.2	0.8
h	"	2 y	Initial	3.1	29.5
			Final	2.4	12.8
i	Pea & Carrot salad	20 y	Initial	5.0	0.6
			Final	0.5	0.6
l	"	2y	Initial	0.2	12.1
			Final	0.2	0.7

Conclusions

The study of the effect of aging on the corrosivity of canned food leads to the following conclusions:

- The corrosivity of canned foods increases over time with respect to both tin and iron freshly polished electrodes.
- For tin, the accelerated thermal aging is not able to mimic the same increase in corrosivity achieved by means of natural aging.

- Over time, the difference between the corrosion potential of tin and iron becomes very small. After 20 years of natural aging, corrosivity is below 10 mV. However, the corrosion potential of tin remains lower compared to iron. Thus, the remaining tin can still act as a sacrificial anode.
- The galvanic coupling currents between tin and iron measured in food are comparable with those measured in citrate buffers.
- The equivalent electrical circuit representing the tin-iron galvanic coupling in citrate buffers also applies to real foods. The tin-iron galvanic coupling currents can be calculated from **Eq. 21** by knowing the tin-iron area ratios, the corrosion potentials and the polarization resistances of tin and iron after 24 h of stabilization.

Curriculum Vitae

Education

October 2014 – September 2018

Doctoral student in Material Science and Engineering

Ecole Polytechnique Fédérale de Lausanne (EPFL), 1015 Lausanne, Switzerland.

February 2012 – December 2013

Master's degree in Industrial Chemistry and Management

Università degli Studi di Milano, 20122 Milan, Italy.

September 2008 - February 2012

Bachelor's degree in Industrial Chemistry

Università degli Studi di Milano, 20122 Milan, Italy.

September 2003 - July 2008

High school certificate. Technical Diploma in Chemistry and Biology

I.I.S " Giuseppe Torno ", 20022 Castano Primo (Milan), Italy.

Publications

- L. Brambilla, F. Cova Caiazzo, A. Michel, S. Michler, R. Bertholon. Degradation of heritage cans: Monitoring of museums' collections. Measurements. 2018; Vol. 127(10): pp. 256-263.
- F. Cova Caiazzo, L. Brambilla, A. Montanari, S. Mischler. Chemical and morphological characterization of commercial tinplate for food packaging. Surface and Interface Analysis.2017; Vol. 50(4): pp. 430-440.
- F. Cova Caiazzo, V. Sisti, S.P. Trasatti, S. Trasatti. Electrochemical characterization of multilayer Cr / CrN-based coatings. Coatings. 2014; Vol. 4(3): pp. 508-526.

- F. Cova Caiazzo, S. Trasatti, V. Sisti. Multilayer coating based on CrN/Cr for molds of plastics. La Metallurgia Italiana. 2014; Vol. 106(6): pp. 3-8.

Participation in conferences

- European Corrosion Congress. September 9th-13th, 2018. Krakow, Poland.
  Oral contribution: Corrosion mechanisms of tin in complexing acids.
- 2nd Conference & Expo of National Association of Corrosion Engineering (NACE). May 27th-29th, 2018. Genoa, Italy. Oral contribution: Tribocorrosion in material engineering. Poster presentation: Tinplate corrosion prediction.
- European Corrosion Congress. September 3th-7th, 2017. Prague, Czech Republic.
  Oral contribution: Tinplate corrosion prediction, the importance of the materials and structure characterization.
- Giornate Nazionali sulla Corrosione e Protezione. June 28th-30th, 2017. Milan, Italy.
  Oral contribution: Meccanismi di corrosion dello stagno in soluzioni acide in condizioni anossiche.
- 2nd International Conference on Valve and Flow Control Technologies. May 24th-25th, 2017. Bergamo, Italy.
  Oral contribution: Tribocorrosion in valves.
- Conservation of food cans in museums' collections workshop. February 27th-28th, 2017. Neuchâtel, Switzerland.
  Oral contribution: tinplate materials characterization.
- 2nd Swiss Corrosion Science day. January 25th, 2017. Dübendorf, Switzerland.
  Oral contribution: Corrosion mechanisms of tin.
- ICOM-CC Metal 2016 Conference. September 26th-30th, 2016. New Deli, India.
  Poster presentation: Preserving cans in collections: the importance of modelling corrosion of tin cans for cultural heritage.
- European Corrosion Congress. September 11th-15th, 2016. Montpellier, France.
  Oral contribution: Corrosion mechanisms of tin in deoxygenated acid solutions.
- 32nd Meeting of the Swiss Working Group of Surface and Interface Science. January 22nd, 2016. Fribourg, Switzerland.

Oral contribution: Characterization of tinplate by means of surface analysis and electrochemical methods.

- Corrosion. November 18th-21st, 2014. Gliwice, Poland.

  Oral contribution: Corrosion behaviour of CrN/Cr multi-layer coatings for molds of plastics.

- Giornate Nazionali sulla Corrosione e Protezione. July 10th-12th, 2013. Naples, Italy

  Oral contribution: Rivestimenti multistrato a base di CrN/Cr per stampi di materie plastiche.